UNIVERSITY OF CALIFORNIA,
IRVINE

A Functional Exploration of Threose Nucleic Acid

DISSERTATION

submitted in partial satisfaction of the requirements
for the degree of

DOCTOR OF PHILOSOPHY

in Pharmacological Sciences

by

Erica Mengyu Lee

Dissertation Committee:
Professor John C. Chaput, Chair
Professor Brian M. Paegel
Associate Professor Lauren V. Albrecht

2026

DEDICATION

To

my parents, from whom I've learned about perseverance

my partner, from whom I've learned about the simple joy of being

TABLE OF CONTENTS

LIST OF FIGURES

Page

ACKNOWLEDGMENTS

I would like to first and foremost express my sincerest gratitude to my research advisor, Professor John Chaput. Through you, I saw creativity, dedication, and hard work come together as you guide your lab towards new discoveries. Thank you for not only believing but also trusting in me over the years to be part of that journey with you. And thank you especially for offering me motivation in those moments when I felt the heaviest weight on my shoulders. I'm glad to have been part of your lab and have you as my mentor.

I would like to express my deepest appreciation for all past and current members of the Chaput Lab who have made it a wonderful environment to work in. Thank you to Victoria, Mohammad, Clark, Joy, and Alex for all the helpful discussions, heartfelt conversations, delightful exchanges, and goofy jokes that somehow appear at the right time without fail to solve a problem or lighten the mood. Thank you to Noah for your patience and enthusiasm to share your trove of knowledge. Your mentorship was instrumental in guiding my research direction and shaping my scientific approach. Thank you to Kim and Turnee for teaching me cellular work and working side-by-side on exciting projects with me. Thank you to Arlene for your positivity. Despite all, you keep the lab functional through keeping an eye on the well-being of lab members *and* lab equipment.

I would like to thank my committee members, Professor Brian Paegel and Professor Lauren Albrecht, for your guidance and perspective during my time at UCI. Your discussions and insights have helped me secure my footing early in the Ph.D. program. Thank you for your willingness to reach out to the naïve first-year and offer me mentorship that made an uncertain beginning feel less daunting and reminded me that I was on the right path.

I would like to thank my family, friends, and partner for encouraging me through my graduate career. I would not have made it this far without your continued support.

Thank you to all the sponsors for your financial support that brought this work to life. Financial support was provided by the University of California, Irvine, National Science Foundation Grant (CHM: 2001434, MCB:1946312), and Pharmaron Fellowship. Additional industrial sponsors include 1E Therapeutics and X, the Moonshot Factory.

Thank you to Oxford University Press and Springer Nature for granting permission to use the following publications in Chapter 1-3 of this dissertation:

Chapter 1 of this dissertation is an adaptation of the material as it appears in Lee, EM, Setterholm, NA, Hajjar, M, Barpuzary, B, and Chaput, JC. Stability and mechanism of threose nucleic acid toward acid-mediated degradation. *Nucleic Acids Res.* **51**, 9542-9551 (2023). doi:10.1093/nar/gkad716, used with permission from Oxford University Press (CC BY 4.0). The authors listed in this publication are Erica M. Lee, Noah A. Setterholm, Mohammad Hajjar, Bhawna Barpuzary, and Professor John C. Chaput.

Chapter 2 of this dissertation is an adaptation of the material as it appears in Lee, EM*, Nguyen, K*, Setterholm, NA, Malik, TN, Chaput, JC. Allele-specific knockdown by an engineered DNAzyme capable of RNase H1 evasion. *Nucleic Acids Res.* **54**, gkaf1476 (2026). doi:10.1093/nar/gkaf1476, used with permission from Oxford University Press (CC BY 4.0). The authors listed in this publication are Erica M. Lee, Kim Nguyen, Noah A. Setterholm, Turnee N. Malik, and Professor John C. Chaput.

Chapter 3 of this dissertation is an adaptation of the material as it appears in Lee EM and Chaput JC. Dynamism and Evolvability in Nucleic Acid Enzymes. *Nat. Commun.* (in press). The authors listed in this publication are Erica M. Lee and Professor John C. Chaput.

VITA

Erica Mengyu Lee

2026	Ph.D. in Pharmacological Sciences, University of California, Irvine
2024	M.S. in Pharmacological Sciences, University of California, Irvine
2020-21	Research Associate, OliX Pharmaceuticals, La Jolla
2019	B.S. in Pharmacological Chemistry, University of California, San Diego

FIELD OF STUDY
Nucleic Acid Chemistry; Synthetic Biology

PUBLICATIONS

(1) Lee, EM*, Nguyen, K*, Setterholm, NA, Malik, TN, Chaput, JC. Allele-specific knockdown by an engineered DNAzyme capable of RNase H1 evasion. *Nucleic Acids Res.* **54**, gkaf1476 (2026). doi:10.1093/nar/gkaf1476.

(2) Majumdar B, Sarma D, Lee EM, Setterholm NA, and Chaput JC. An improved synthesis of guanine TNA phosphoramidite for oligonucleotide synthesis. *Nucleosides, Nucleotides, and Nucleic Acids* **44**, 474-485 (2024). doi:10.1080/15257770.2024.2369688.

(3) Lee, EM, Setterholm, NA, Hajjar, M, Barpuzary, B, Chaput, JC. Stability and mechanism of threose nucleic acid toward acid-mediated degradation. *Nucleic Acids Res.* **51**, 9542-9551 (2023). doi:10.1093/nar/gkad716.

(4) Lee EM and Chaput JC. Dynamism and Evolvability in Nucleic Acid Enzymes. *Nat. Commun.* (manuscript in press).

(5) Lozoya-Colinas, A*, Lee JJ*, Kundu, N, Lee EM, and Chaput JC. Threomer Inhibition of S1-ACE2 Binding. *ACS Synth. Biol.* (manuscript in press).

(6) Mikami A, Datta D, Kundu J, Kumar V, Erande N, Medina E, Maola, VA, Lee EM, Matsuda S, Harp J, Egli M, Chaput JC, Manoharan M. Chiral-4'-methyl-α-(L)-threofuranosyl nucleic acids (MTNA): Synthesis, structure, binding affinity, nuclease stability, and polymerase recognition. *J. Am. Chem. Soc.* (manuscript in press).

(7) Lozoya-Colinas, A*, Lee JJ*, Kundu, N, Lee EM, and Chaput JC. A Scalable Route to Experimentally Validated Sequence-Function Datasets for AI-Driven XNA Aptamer Discovery (manuscript in preparation).

ABSTRACT OF THE DISSERTATION

A Functional Exploration of Threose Nucleic Acid
by
Erica Mengyu Lee
Doctor of Philosophy in Pharmacological Sciences
University of California, Irvine, 2026
Professor John C. Chaput, Chair

Xeno-nucleic acids (XNAs) are artificial genetic polymers with unnatural sugar and backbone structures that confer unique physicochemical properties, such as enhanced biostability and improved RNA binding thermodynamics, making them attractive for a wide range of applications. One such XNA is threose nucleic acid (TNA), which features a threose sugar ring with a 2′-3′ phosphodiester backbone linkage that confers high nuclease resistance while still supporting anti-parallel Watson-Crick base-pairing with DNA and RNA. Initially investigated as a plausible RNA progenitor, TNA research has since expanded towards its development as a molecular tool. This dissertation examines TNA across three studies that progress from the characterization of one of TNA's special properties to the application of TNA towards specific functions. First, to examine the mechanistic rationale behind the chemical resilience of TNA, the degradation kinetics of TNA under acidic, high-temperature conditions was assessed using RP-HPLC, mass spectrometry, and molecular dynamics simulations. TNA exhibited a half-life substantially longer than DNA and RNA, with strand cleavage occurring via β-elimination of the 2′-phosphodiester linkage, a mechanism distinct from natural nucleic acids and attributable to destabilization of the oxocarbenium intermediate responsible for depurination. Second, to demonstrate the utility of TNA in a therapeutic context, TNA was incorporated into the backbone architecture of an RNA-cleaving DNA enzyme (DNAzyme) through chemical evolution. The resulting TNA-modified lead

construct exhibited enhanced catalytic performance and achieved allele-specific mRNA and protein knockdown of the oncogenic KRAS G12V mutation by evading RNase H1 activity in cells. Third, to explore the link between dynamism and evolvability in nucleic acid enzymes, RNA-cleaving TNA enzymes (threozymes) were evolved by in vitro selection and compared to the well-characterized 10-23 DNAzyme. Unlike the DNAzyme, which was most active at physiological temperature, the threozymes required elevated temperature to become catalytically active, a finding consistent with TNA's more conformationally restricted backbone that limits access to productive folding states and raises the energetic barrier to catalysis. Together, these findings establish TNA as a chemical tool for engineering nucleic acid enzymes and a model system for probing how backbone architecture governs catalytic evolvability in nucleic acids, carrying significant implications in the development of XNA-based molecular medicine and biotechnologies.

INTRODUCTION

Nucleic Acids

Nucleic acids form the basis of life. Deceptively simple in appearance, these polymeric chains of sugar units exhibit two essential features that set them apart from other biopolymers: heredity and adaptability. Not only do nucleic acids possess the unique capability to store and propagate high densities of genetic information, but they also adapt over time and gain biologically useful functions through Darwinian evolution. Because of these features, nucleic acids can be used as powerful chemical tools in molecular medicine and biotechnology, where their sequence programmability and evolvability can be harnessed for therapeutic and diagnostic purposes. However, natural nucleic acids, DNA and RNA, are vulnerable to nucleases, severely limiting their utility in contexts outside of the passive maintenance of the genome.

Fortunately, the molecular properties of nucleic acids are largely determined by its chemical scaffold (i.e., sugar and backbone) rather than its sequence. Because these two elements are decoupled, the chemical scaffold can be modified to improve properties such as stability without disrupting the sequence-encoded information that governs recognition of target molecules. This modularity has motivated exploration of chemically modified nucleic acids with enhanced performance.[1,2]

Early generations of chemical modifications, including phosphorothioate (PS), 2′-O-methyl (2′-OMe), 2′-methoxyethyl (2′-MOE), and 2′-fluoro (2′-F), introduce subtle alterations to the structure in DNA and RNA, but confer meaningful improvements in nuclease re-

sistance and target binding affinity (Figure 1).[3,4] Despite being older chemistries, these modifications are still extensively used in oligonucleotide therapeutics and can be found in oligonucleotide drug candidates in ongoing clinical trials.[2]

Newer generations of modifications have pushed this paradigm further, encompassing artificial genetic polymers with distinct sugar moieties that fundamentally alter the chemical backbone, as well as novel base pairs that expand the genetic code. Termed xeno-nucleic acids (XNAs), these unnatural systems offer the opportunity to explore new regions of chemical space beyond those accessible by natural DNA and RNA.[5,6] With each successive generation of modifications, the field has gained deeper insight into the relationship between nucleic acid chemistry and function, progressively broadening the repertoire of achievable properties such as chemical stability, biological stability, enhanced binding affinity, cellular delivery, and lowered toxicity, greatly diversifying the functionalities and biotechnical applications of nucleic acids.

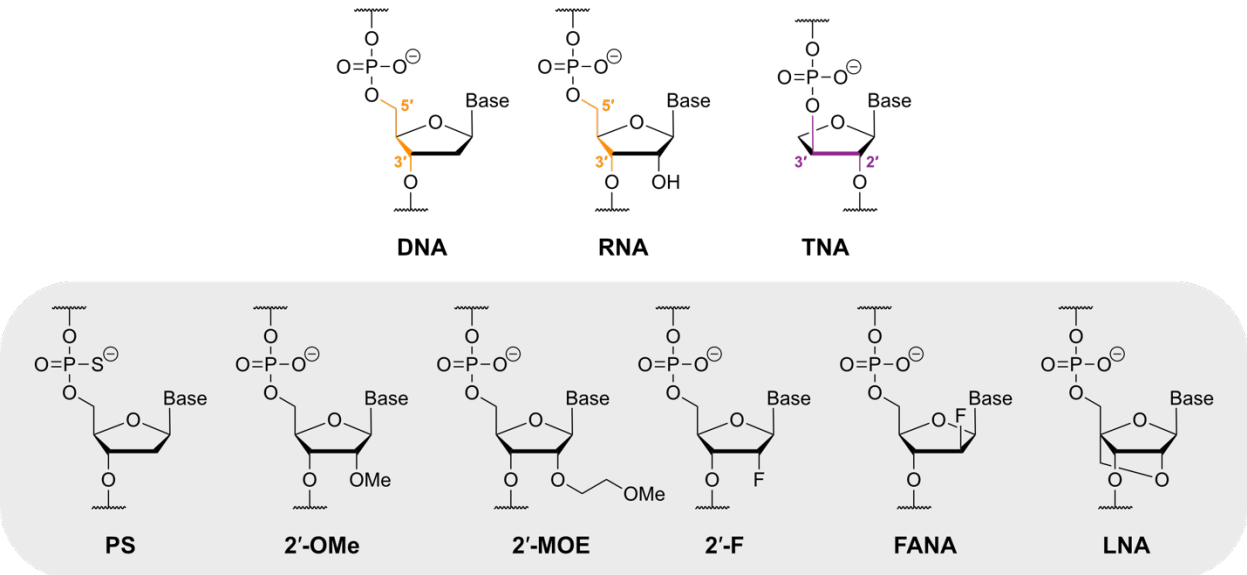

Figure 0.1. Time-dependent acid stability. *Chemical structures of DNA, RNA, TNA, and early generations of modifications used in nucleic acid-based therapeutics. a-L-threose nucleic acid (TNA) has one less atom in its backbone unit than DNA and RNA as highlighted.*

Of the various XNAs investigated over the years, 3',2'-α-L-threose nucleic acid (TNA) is one of the most prominently studied.[7–9] First proposed as an RNA progenitor by Albert Eschenmoser because of its chemical simplicity and base-pairing properties, TNA has since earned recognition well beyond its origins in origin-of-life research. Here, we review the structural and biophysical properties of TNA that underpin its utility, followed by a survey of its biomedical and biotechnological applications.

TNA Origins

TNA arrived in the spotlight during an investigation into the chemical etiology of nucleic acid structure by Eschenmoser et al., who sought to understand nature's motive for choosing ribose, a five-carbon sugar, as the molecular basis for RNA.[7,8] Their approach involved synthesis and characterization of alternative genetic polymers to evaluate their likelihoods of being either precursors or competitors to RNA. To be considered as a viable candidate, the nucleic acid analogue must meet two preliminary criteria: (1) its building blocks are derivable from natural prebiotic chemistry, and (2) it retains Watson-Crick base-pairing for genetic information transfer within itself and with existing nucleic acid systems. Through studies of sugars within the aldose family, it was gradually realized that TNA satisfied both criteria.

The relative chemical simplicity of threose met the first criterion. Threose is a four-carbon sugar that can be synthesized under prebiotic conditions through aldolization of glycolaldehyde phosphates,[10] supporting TNA's possible existence on early Earth based on building block availability. However, meeting the second criterion came as a surprise. At the time, it was widely assumed that Watson-Crick base-pairing required a backbone spacing of six bonds between repeating units, consistent with natural systems. TNA, on the other hand,

is composed of α-L-threose units linked through 3′-to-2′ phosphodiester linkages, yielding a repeat unit that is one carbon shorter than DNA or RNA, thus featuring only five bonds between repeating units. Yet, it was observed that TNA could efficiently engage in antiparallel Watson-Crick base-pairing with itself as well as complementary strands of DNA and RNA,[7,8] challenging the prior assumption.

Through structural studies, the conformational basis of TNA's unexpected base-pairing properties was elucidated. TNA accommodates the shorter backbone by orienting its 3′- and 2′-substituents in a quasi-trans-diaxial conformation, effectively bridging the geometric gap imposed by the missing carbon.[11] NMR studies have further revealed that TNA adopts a C4′-exo sugar pucker and takes on an A-like helical geometry in both homo- and heteroduplexes, closely resembling the duplex architecture of RNA rather than the B-form helix of DNA, and provides insight into the stronger hybridization observed in RNA:TNA than DNA:TNA duplexes in thermodynamic studies.[12–14]

The structural similarity to RNA is notable as it suggests that TNA and RNA are not merely informationally compatible, but geometrically convergent, a point that has fueled ongoing interest in TNA as an RNA progenitor. Experimental evidence further supports that cross-pairing between TNA and RNA is not a passive relationship, lending greater plausibility to the hypothesis of a TNA world before an RNA world. TNA oligonucleotides can serve as templates for non-enzymatic RNA oligomerization as well as ribozyme-catalyzed RNA polymerization,[15,16] consistent with a model in which RNA gradually supplants TNA as the dominant information carrier.

Taken together, these initial findings demonstrate that the informational capacity of nucleic acids was not as structurally constrained as previously believed, expanding the chemical landscape for research in origins-of-life and synthetic biology.

TNA Properties

Because of its unique backbone, TNA possesses distinct biophysical properties that extend its utility to various applications and make it an especially attractive chemical modification for oligonucleotide-based therapeutics and diagnostics. Its properties can address several pharmacological bottlenecks of an oligonucleotide—from resisting nuclease degradation, crossing the cell membrane, clearing safely from the body, and to surviving the acidic endosomal environment that follows cellular uptake. Together, these insights underscore the broad influence that backbone chemistry can have on pharmacokinetics.

One of TNA's most extensively characterized—and most favored—traits is its immunity against nucleases. TNA remains undigested after seven days of incubation at 37˚C in simulated physiological conditions involving human serum and human liver microsomes,[17] under which DNA and RNA are degraded within minutes. Moreover, TNA's resistance to nucleases can be extended beyond itself. TNA can shield adjacent DNA and RNA residues when incorporated into chimeric constructs as well as protect complementary RNA strands from enzymatic degradation.[17] Impressively, when compared to current commonly used modified nucleic acids in oligonucleotide drugs, TNA outcompetes 2′-OMe, 2′-MOE, and locked nucleic acid (LNA) as the most biological stable modification in assays against 5′- and 3′-exonucleases like phosphodiesterase II (PDII) and snake venom phosphodiesterase (SVPDE) (Figure 2).

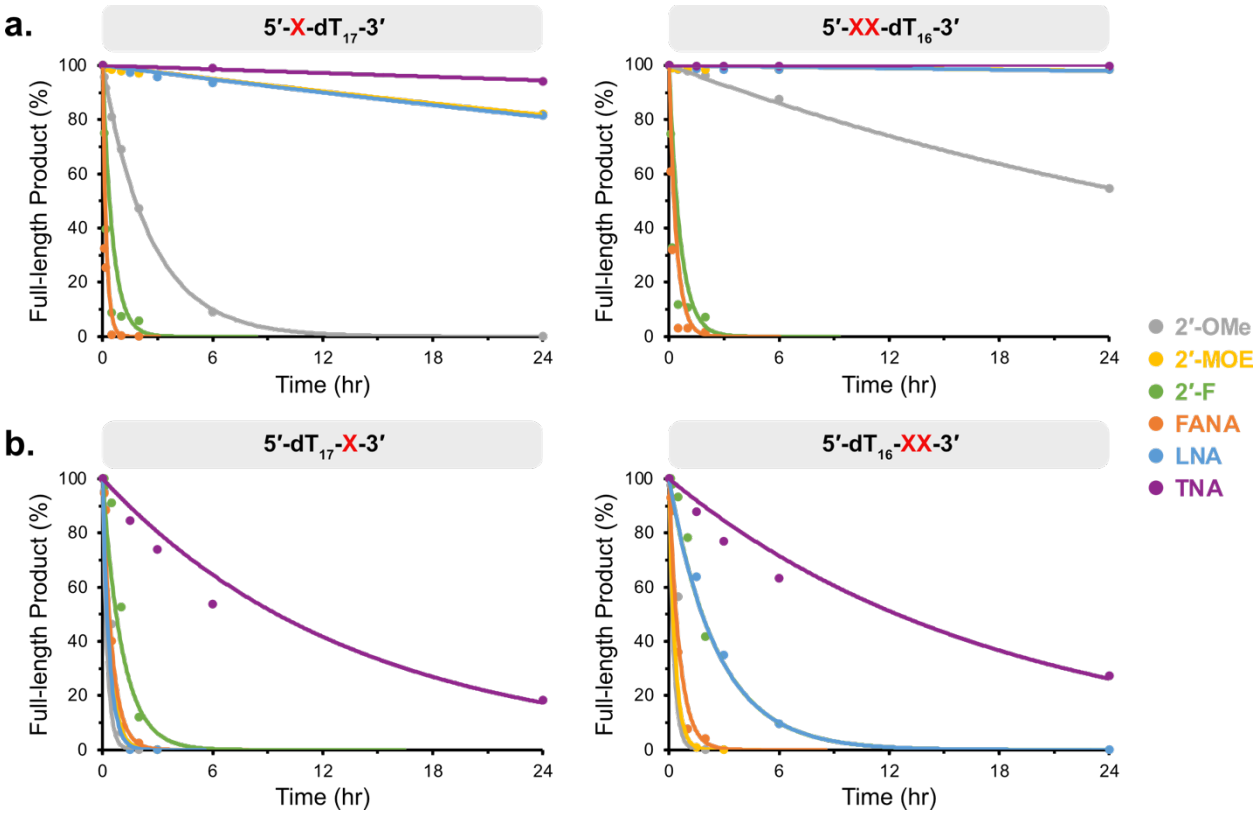

Figure 0.2. Exonuclease stability. a) *Degradation profiles of oligonucleotides (20 μM) modified at the 5′-end in the presence of PDII (500 mU/mL) and* ***b)*** *modified at the 3′-end in the presence of SVPDE (150 mU/mL). The red X represents the modified positions of the dT_{18} oligonucleotide. Degradation analysis was done by reversed-phase HPLC (RP-HPLC).*

Moreover, high biostability extends extracellular lifetime and may play a role in the gymnotic uptake of TNA, allowing it to be internalized by cells without the aid of a carrier or transfection reagent, an important trait that can overcome poor cellular uptake of therapeutic oligonucleotides, broadening their delivery to extrahepatic tissues. Using flow cytometry and confocal microscopy, concentration-dependent internalization of TNA has been observed across multiple cancer cell lines.[18] Furthermore, this uptake is not limited to monolayer cultures. TNA also penetrates 3D multicellular spheroids in a concentration- and time-dependent manner,[18] supporting its relevance to more physiologically representative tissue models.

Importantly, this efficient cellular uptake does not come at the cost of toxicity. TNA-treated cells remained >95% viable after 24 hours of incubation even at high TNA concentrations,[18] reflecting negligible cytotoxicity. This favorable cellular profile is mirrored at the organismal level. *In vivo* biodistribution studies show that TNA follows a pattern typical of other nucleic acid polymers, accumulating predominantly in the kidneys following intravenous injection and clearing through renal filtration.[18] Histopathological and blood chemistry analyses of TNA-treated mice revealed no abnormalities,[18] indicating a favorable biosafety profile and supporting TNA's continued development as a viable therapeutic scaffold.

Yet, once internalized, an oligonucleotide drug faces the challenge of surviving the acidic environment of the endosome to achieve cytosolic release. Here, TNA offers a further advantage, exhibiting notable stability under acidic conditions due to its slow rate of depurination relative to DNA and RNA (discussed further in Chapter 1). This property is particularly relevant to endosomal escape, a frequent bottleneck in oligonucleotide drug delivery as ≤1-2% of internalized oligonucleotides escape from endosomes.[19] More broadly, this finding illustrates a recurring theme in XNA research in which each newly characterized property of an XNA, like TNA, not only expands its own utility but also offers design principles that can guide the development of future XNA-based reagents.

TNA Applications

TNA is being investigated along several lines. One area of focus is its use as a chemical modification, where it can be incorporated into existing oligonucleotides to improve potency and specificity. Researchers are also exploring TNA as an evolvable polymer, capable of acquiring catalytic and binding functions. Beyond these applications, the utility of TNA is being

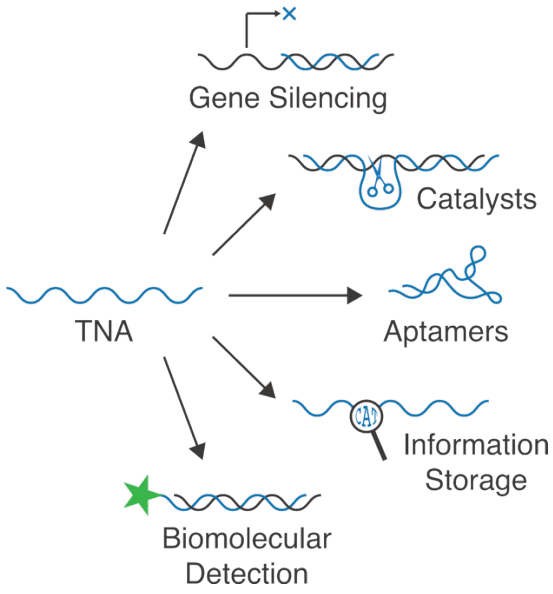

Figure 0.3. TNA applications. *The properties of TNA make it a versatile molecular tool in biomedical and biotechnological applications.*

recognized in more specialized areas of biotechnology as well. The following sections provide specific examples of these investigations.

Antisense oligonucleotides (ASOs). In 2019 and 2024, Lo et al. reported that TNA ASOs can suppress cancer-associated genes—BcL-2 and Akt—at the mRNA and protein levels via an RNase H-independent mechanism (steric inhibition of translation) with *in vivo* antitumor activity.[20,21] Across both targets, TNA ASOs achieved mRNA knockdown of ~40–70% and protein knockdown of ~40–50% relative to controls. Substantial antitumor effects of TNA ASOs were also observed in xenograft mouse models, demonstrating a 60–75% relative reduction in tumor growth compared to that of controls with no detectable systemic toxicity or organ damage caused by TNA. These studies build a consistent proof-of-concept that TNA ASOs can silence disease-relevant genes at both the mRNA and protein level and show prom-

ise in translating *in vitro* gene-silencing activity into meaningful *in vivo* therapeutic outcomes, positioning TNA as a viable RNase H-independent alternative to conventional ASO chemistries.

Small-interfering RNAs (siRNAs). In 2023, Manoharan et al. demonstrated that TNA incorporation can confer beneficial traits when placed at specific positions within an siRNA.[22] When placed at positions 6-7 of the antisense strand within the seed region, TNA nearly eliminated off-target effects without reducing on-target Ago2-mediated gene-silencing activity, owing to its identity of a thermodynamically destabilizing modification like glycol nucleic acid (GNA). This effect was further corroborated by crystallographic and molecular modeling data showing that TNA's C4′-exo pucker naturally matches the tight phosphate-phosphate spacing at the Ago2-induced kink between positions 6 and 7 in the antisense strand, conformationally pre-organizing the antisense strand upon binding to Ago2. Having a single TNA residue in the seed region also reduced hepatotoxicity in rats at supratherapeutic doses, which likely resulted from reduced off-target silencing observed *in vitro*. More recently, Zheng et al. similarly leveraged TNA's destabilizing character, showing that its incorporation at the 3′-terminus of the sense strand can achieve selective strand bias favoring antisense strand-loading into RISC.[23] These findings indicate that strategic incorporation of TNA can simultaneously improve the potency and safety of siRNA therapeutics.

DNA enzymes (DNAzymes). DNAzymes inherently recognize and cleave specific dinucleotide junctions in RNA, enabling discrimination at the single-nucleotide level for allele-specific therapies. However, this class of molecule faces challenges of poor catalytic activity and low biostability under physiological conditions, severely limiting its use as a gene-silencing agent. Among RNA-cleaving DNAzymes, 10-23 is the most studied, with research focused

on improving its performance through chemical modifications.[24–26] In 2021, Chaput et al. introduced TNA, alongside 2′-fluoro-arabinonucleic acid (FANA), as a capping agent for 10-23.[27,28] Having a single TNA residue at the 5′- and 3′-termini of the XNA-modified 10-23 significantly boosted biostability in simulated physiological conditions (i.e., human serum and human liver microsomes). More recently, Chaput et al. evaluated TNA substitutions at additional positions within a 10-23 scaffold, finding that a single TNA substitution in the catalytic core increased activity while TNA in the binding arm abrogated a competing cleavage mechanism by cellular RNase H1.[29] The resulting TNA-modified DNAzyme enabled allele-specific knockdown of an oncogenic KRAS mutation in mammalian cells and facilitated general knockdown of PCSK9 and GATA3 targets (discussed further in Chapter 2). These studies establish TNA as a powerful modification for engineering DNAzymes with enhanced intracellular activity and allele-specific precision.

Catalysts. Just as DNA and RNA can be evolved for catalytic function, so can TNA. In 2021 and 2025, Yu et al. reported TNA enzymes (TNAzymes) capable of RNA ligation, catalyzing the formation of a non-canonical 2′-5′ and canonical 3′-5′ phosphodiester linkage, respectively, between two RNA fragments.[30,31] These findings suggest a possible role of TNA in assembling RNA fragments into more complex structures during early evolution, underscoring its prebiotic relevance as an RNA progenitor. In 2022, Yu et al. extended TNAzyme function beyond ligation, describing an RNA-cleaving TNAzyme that recognized a single point mutation to selectively suppress mutant epidermal growth factor receptor (EGFR) expression in eukaryotic cells,[32] demonstrating TNA's potential as a molecular tool for precision medicine. More recently, Chaput et al. further uncovered a striking difference in temperature dependence between DNAzymes and TNAzymes, emphasizing the importance of backbone

architecture as a critical parameter governing evolvability in nucleic acids (further discussed in Chapter 3).

Aptamers. Aptamers are single-stranded oligonucleotides that bind to target molecules through specific structural interactions. In 2012, Chaput et al. evolved the first TNA aptamer which specifically bound human thrombin.[33] Since then, the field has expanded to show that TNA can be selected against increasingly diverse targets, ranging from small molecules, like ochratoxin A and ATP,[34,35] to therapeutically relevant proteins, like PD-L1 and c-Myc.[36,37] In 2020, Yu et al. evolved PD-L1 TNA aptamers with nanomolar affinities that effectively block PD-1/PD-L1 interactions and suppress tumor growth in xenograft mouse models,[36] demonstrating direct therapeutic relevance in cancer immunotherapy. In 2023, Yu and Guan et al. utilized a c-Myc TNA aptamer as a component in a proteolysis targeting chimera (PROTAC) for targeted proteasomal degradation of c-Myc,[37] showcasing the utility of TNA aptamers in other therapeutic avenues. More recently, efforts to push the performance of TNA aptamers closer to that of antibodies have led to the development of chemically modified "threomer" libraries bearing amino-acid-like side chains (e.g., phenylalanine, tryptophan).[38] These nucleobase modifications mimic the hydrophobic residues found at antibody paratopes and substantially increase the frequency of high-affinity, slow-off-rate binders recovered from selection.

Gene delivery. In 2020, Lu et al. developed a TNA loop-modified primer pair to construct terminal-closed linear genes.[39] This approach yielded a gene construct with markedly improved resistance to exonuclease digestion and serum degradation compared to the unmodified linear gene, resulting in more efficient and prolonged gene expression in eukaryotic cells. As a proof-of-concept study, this work demonstrates that TNA's biostability and

duplex-forming compatibility with DNA can be leveraged specifically for non-viral gene delivery, addressing a long-standing limitation of linear gene cassettes caused by poor stability. However, while the result signals promise for TNA in gene delivery which is of relevance to gene therapy, this is an application area still in its infancy compared to the more developed roles TNA has found in previously described therapeutic fields.

Biosensors. In 2021, Lo et al. constructed a TNA-based probe that enabled real-time detection of miRNA in cells, though its detection limit (2.5 nM) remained modest.[40] In a follow-up study, Lo et al. loaded TNA probes onto graphene oxide (GO)—known to reduce background noise—which significantly improved the limit of detection by a reported 88-fold compared to the TNA-only design, while preserving single-nucleotide mismatch discrimination.[41] The GO-TNA platform was tested for *in vitro* and *in vivo* imaging of oncogenic miRNAs, offering preliminary evidence of feasible detection. Together, these studies support TNA's potential as a biocompatible probe for real-time nucleic acid detection in biological environments.

Information storage. TNA's nuclease resistance has motivated its exploration as a biomaterial for long-term digital information storage, where DNA's susceptibility to enzymatic degradation is a persistent liability. In 2020, Chaput et al. demonstrated proof-of-concept by encoding text and image files (23 kB total) into DNA templates, enzymatically converting them into TNA, and recovering the information with high fidelity (>99%).[42] The TNA messages survived exposure to human serum, liver microsomes, and SVPDE that destroyed equivalent DNA messages, establishing TNA as a genuine safeguard against nuclease-driven information loss. In 2024, Kath-Schorr et al. extended TNA's information storage capacity by

expanding its genetic alphabet with the hydrophobic unnatural base pair TPT3:NaM.[43] Together, these studies suggest TNA is a chemically robust and increasingly versatile platform for archival data storage, though full realization of an expanded alphabet system will require engineered polymerases to encode and decode novel bases.

Thesis Overview: TNA's Scope

TNA research was born of a simple question rooted in fundamental chemistry, yet it quickly grew into an exploration of applications across therapeutics and biotechnologies. The backbone novelty that made TNA a plausible RNA progenitor also renders it refractory to nucleases, a trait that has made it a popular molecular tool. With continued investigation, TNA is well positioned to move further from a curiosity of prebiotic chemistry into a mainstay of nucleic acid-based applications. The chapters that follow take up this thread directly, examining TNA's broader implications in the design of next-generation XNA-based tools. Chapter 1 begins with an exploration of TNA's acid stability, illustrating special insights that can be gained from investigating the physicochemical properties of XNAs. Chapter 2 offers an example of TNA application through its performance as a DNAzyme modification. Chapter 3 closes by relating TNA's backbone rigidity to its catalytic accessibility, offering a framework for evolving other XNAs.

References

(1) Duffy, K.; Arangundy-Franklin, S.; Holliger, P. Modified Nucleic Acids: Replication, Evolution, and next-Generation Therapeutics. *BMC Biology* **2020**, *18* (1), 112.

(2) Egli, M.; Manoharan, M. Chemistry, Structure and Function of Approved Oligonucleotide Therapeutics. *Nucleic Acids Res* **2023**, *51* (6), 2529–2573.

(3) Manoharan, M. 2′-Carbohydrate Modifications in Antisense Oligonucleotide Therapy: Importance of Conformation, Configuration and Conjugation. *Biochimica et Biophysica Acta (BBA) - Gene Structure and Expression* **1999**, *1489* (1), 117–130.

(4) Sabahi, A.; Guidry, J.; Inamati, G. B.; Manoharan, M.; Wittung-Stafshede, P. Hybridization of 2′-Ribose Modified Mixed-Sequence Oligonucleotides: Thermodynamic and Kinetic Studies. *Nucleic Acids Research* **2001**, *29* (10), 2163–2170.

(5) Anosova, I.; Kowal, E. A.; Dunn, M. R.; Chaput, J. C.; Van Horn, W. D.; Egli, M. The Structural Diversity of Artificial Genetic Polymers. *Nucleic Acids Research* **2016**, *44* (3), 1007–1021.

(6) Chaput, J. C.; Egli, M.; Herdewijn, P. The XNA Alphabet. *Nucleic Acids Res* **2025**, *53* (13), gkaf635.

(7) Schöning, K.; Scholz, P.; Guntha, S.; Wu, X.; Krishnamurthy, R.; Eschenmoser, A. Chemical Etiology of Nucleic Acid Structure: The Alpha-Threofuranosyl-(3'-->2') Oligonucleotide System. *Science* **2000**, *290* (5495), 1347–1351.

(8) Schöning, K.-U.; Scholz, P.; Wu, X.; Guntha, S.; Delgado, G.; Krishnamurthy, R.; Eschenmoser, A. The α-L-Threofuranosyl-(3′→2′)-Oligonucleotide System ('TNA'): Synthesis and Pairing Properties. *Helvetica Chimica Acta* **2002**, *85* (12), 4111–4153.

(9) Wang, J.; Yu, H. Threose Nucleic Acid as a Primitive Genetic Polymer and a Contemporary Molecular Tool. *Bioorganic Chemistry* **2024**, *143*, 107049.

(10) Müller, D.; Pitsch, S.; Kittaka, A.; Wagner, E.; Wintner, C. E.; Eschenmoser, A.; Ohlofjgewidmet, G. Chemie von A-Aminonitrilen. Aldomerisierung von Glycolaldehyd-Phosphat Zu Racemischen Hexose-2,4,6-Triphosphaten Und (in Gegenwart von Formaldehyd) Racemischen Pentose-2,4-Diphosphaten: Rac-Allose-2,4,6-Triphosphat Und Rac-Ribose-2,4-Diphosphat Sind Die Reaktionshauptprodukte. *Helvetica Chimica Acta* **1990**, *73* (5), 1410–1468.

(11) Wilds, C. J.; Wawrzak, Z.; Krishnamurthy, R.; Eschenmoser, A.; Egli, M. Crystal Structure of a B-Form DNA Duplex Containing (l)-α-Threofuranosyl (3'→2') Nucleosides: A Four-Carbon Sugar Is Easily Accommodated into the Backbone of DNA. *J. Am. Chem. Soc.* **2002**, *124* (46), 13716–13721.

(12) Pallan, P. S.; Wilds, C. J.; Wawrzak, Z.; Krishnamurthy, R.; Eschenmoser, A.; Egli, M. Why Does TNA Cross-Pair More Strongly with RNA Than with DNA? An Answer From X-Ray Analysis. *Angewandte Chemie International Edition* **2003**, *42* (47), 5893–5895.

(13) Ebert, M.-O.; Mang, C.; Krishnamurthy, R.; Eschenmoser, A.; Jaun, B. The Structure of a TNA−TNA Complex in Solution: NMR Study of the Octamer Duplex Derived from α-(l)-Threofuranosyl-(3′-2′)-CGAATTCG. *J. Am. Chem. Soc.* **2008**, *130* (45), 15105–15115.

(14) Anosova, I.; Kowal, E. A.; Sisco, N. J.; Sau, S.; Liao, J.; Bala, S.; Rozners, E.; Egli, M.; Chaput, J. C.; Van Horn, W. D. Structural Insights into Conformation Differences between DNA/TNA and RNA/TNA Chimeric Duplexes. *ChemBioChem* **2016**, *17* (18), 1705–1708.

(15) Heuberger, B. D.; Switzer, C. Nonenzymatic Oligomerization of RNA by TNA Templates. *Org. Lett.* **2006**, *8* (25), 5809–5811.

(16) Horning, D. P.; Bala, S.; Chaput, J. C.; Joyce, G. F. RNA-Catalyzed Polymerization of Deoxyribose, Threose, and Arabinose Nucleic Acids. *ACS Synth. Biol.* **2019**, *8* (5), 955–961.

(17) Culbertson, M. C.; Temburnikar, K. W.; Sau, S. P.; Liao, J.-Y.; Bala, S.; Chaput, J. C. Evaluating TNA Stability under Simulated Physiological Conditions. *Bioorganic & Medicinal Chemistry Letters* **2016**, *26* (10), 2418–2421.

(18) Wang, F.; Liu, L. S.; Li, P.; Lau, C. H.; Leung, H. M.; Chin, Y. R.; Tin, C.; Lo, P. K. Cellular Uptake, Tissue Penetration, Biodistribution, and Biosafety of Threose Nucleic Acids: Assessing in Vitro and in Vivo Delivery. *Materials Today Bio* **2022**, *15*, 100299.

(19) Dowdy, S. F. Endosomal Escape of RNA Therapeutics: How Do We Solve This Rate-Limiting Problem? *RNA* **2023**, *29* (4), 396–401.

(20) Wang, F.; Liu, L. S.; Lau, C. H.; Han Chang, T. J.; Tam, D. Y.; Leung, H. M.; Tin, C.; Lo, P. K. Synthetic α-l-Threose Nucleic Acids Targeting BcL-2 Show Gene Silencing and in Vivo Antitumor Activity for Cancer Therapy. *ACS Appl. Mater. Interfaces* **2019**, *11* (42), 38510–38518.

(21) Li, P.; Zheng, S.; Leung, H. M.; Liu, L. S.; Chang, T. J. H.; Maryam, A.; Wang, F.; Chin, Y. R.; Lo, P. K. TNA-Mediated Antisense Strategy to Knockdown Akt Genes for Triple-Negative Breast Cancer Therapy. *Small Methods* **2024**, *8* (11), 2400291.

(22) Matsuda, S.; Bala, S.; Liao, J.-Y.; Datta, D.; Mikami, A.; Woods, L.; Harp, J. M.; Gilbert, J. A.; Bisbe, A.; Manoharan, R. M.; Kim, M.; Theile, C. S.; Guenther, D. C.; Jiang, Y.; Agarwal, S.; Maganti, R.; Schlegel, M. K.; Zlatev, I.; Charisse, K.; Rajeev, K. G.; Castoreno, A.; Maier, M.; Janas, M. M.; Egli, M.; Chaput, J. C.; Manoharan, M. Shorter Is Better: The α-(l)-Threofuranosyl Nucleic Acid Modification Improves Stability, Potency, Safety, and Ago2 Binding and Mitigates Off-Target Effects of Small Interfering RNAs. *J. Am. Chem. Soc.* **2023**, *145* (36), 19691–19706.

(23) Cheng, Z.; Cai, Y.; Zhang, E.; Cheng, Y.; Li, Y.; Zhang, X.; Liang, G.; Hou, M.; Wang, C.; Hu, T.; Tian, G.; Xie, Y.; Zheng, W.; Shen, J. Rational Design and Screening of Chemically Modified Anti-SARS-CoV-2 siRNA. *ACS Infect. Dis.* **2026**, *12* (5), 1727-1738.

(24) Larcher, L. M.; Pitout, I. L.; Keegan, N. P.; Veedu, R. N.; Fletcher, S. DNAzymes: Expanding the Potential of Nucleic Acid Therapeutics. *Nucleic Acid Ther* **2023**, *33* (3), 178–192.

(25) Santoro, S. W.; Joyce, G. F. A General Purpose RNA-Cleaving DNA Enzyme. *Proceedings of the National Academy of Sciences* **1997**, *94* (9), 4262–4266.

(26) Santoro, S. W.; Joyce, G. F. Mechanism and Utility of an RNA-Cleaving DNA Enzyme. *Biochemistry* **1998**, *37* (38), 13330–13342.

(27) Wang, Y.; Nguyen, K.; Spitale, R. C.; Chaput, J. C. A Biologically Stable DNAzyme That Efficiently Silences Gene Expression in Cells. *Nat. Chem.* **2021**, *13* (4), 319–326.

(28) Nguyen, K.; Wang, Y.; England, W. E.; Chaput, J. C.; Spitale, R. C. Allele-Specific RNA Knockdown with a Biologically Stable and Catalytically Efficient XNAzyme. *J. Am. Chem. Soc.* **2021**, *143* (12), 4519–4523.

(29) Lee, E. M.; Nguyen, K.; Setterholm, N. A.; Malik, T. N.; Chaput, J. C. Allele-Specific Knockdown by an Engineered DNAzyme Capable of RNase H1 Evasion. *Nucleic Acids Res* **2026**, *54* (1), gkaf1476.

(30) Wang, Y.; Wang, Y.; Song, D.; Sun, X.; Zhang, Z.; Li, X.; Li, Z.; Yu, H. A Threose Nucleic Acid Enzyme with RNA Ligase Activity. *J. Am. Chem. Soc.* **2021**, *143* (21), 8154–8163.

(31) Wang, J.; Han, F.; Zou, Y.; Wang, M.; Wang, Y.; Chen, J.-Y.; Yu, H. A Threose Nucleic Acid (TNA) Enzyme Catalyzing Native 3′-5′ Ligation of RNA. *J. Am. Chem. Soc.* **2025**, *147* (21), 18349–18358.

(32) Wang, Y.; Wang, Y.; Song, D.; Sun, X.; Li, Z.; Chen, J.-Y.; Yu, H. An RNA-Cleaving Threose Nucleic Acid Enzyme Capable of Single Point Mutation Discrimination. *Nat. Chem.* **2022**, *14* (3), 350–359.

(33) Yu, H.; Zhang, S.; Chaput, J. C. Darwinian Evolution of an Alternative Genetic System Provides Support for TNA as an RNA Progenitor. *Nature Chem* **2012**, *4* (3), 183–187.

(34) Rangel, A. E.; Chen, Z.; Ayele, T. M.; Heemstra, J. M. In Vitro Selection of an XNA Aptamer Capable of Small-Molecule Recognition. *Nucleic Acids Res* **2018**, *46* (16), 8057–8068.

(35) Zhang, L.; Chaput, J. C. In Vitro Selection of an ATP-Binding TNA Aptamer. *Molecules* **2020**, *25* (18), 4194.

(36) Li, X.; Li, Z.; Yu, H. Selection of Threose Nucleic Acid Aptamers to Block PD-1/PD-L1 Interaction for Cancer Immunotherapy. *Chem. Commun.* **2020**, *56* (93), 14653–14656.

(37) Li, X.; Zhang, Z.; Gao, F.; Ma, Y.; Wei, D.; Lu, Z.; Chen, S.; Wang, M.; Wang, Y.; Xu, K.; Wang, R.; Xu, F.; Chen, J.-Y.; Zhu, C.; Li, Z.; Yu, H.; Guan, X. C-Myc-Targeting PROTAC Based on a TNA-DNA Bivalent Binder for Combination Therapy of Triple-Negative Breast Cancer. *J. Am. Chem. Soc.* **2023**, *145* (16), 9334–9342.

(38) Lozoya-Colinas, A.; Yu, Y.; Chaput, J. C. Functionally Enhanced XNA Aptamers Discovered by Parallelized Library Screening. *J. Am. Chem. Soc.* **2023**, *145* (47), 25789–25796.

(39) Lu, X.; Wu, X.; Wu, T.; Han, L.; Liu, J.; Ding, B. Efficient Construction of a Stable Linear Gene Based on a TNA Loop Modified Primer Pair for Gene Delivery. *Chem. Commun.* **2020**, *56* (68), 9894–9897.

(40) Wang, F.; Liu, L. S.; Li, P.; Leung, H. M.; Tam, D. Y.; Lo, P. K. Biologically Stable Threose Nucleic Acid-Based Probes for Real-Time microRNA Detection and Imaging in Living Cells. *Molecular Therapy Nucleic Acids* **2022**, *27*, 787–796.

(41) Tam, D. Y.; Li, P.; Liu, L. S.; Wang, F.; Leung, H. M.; Lo, P. K. Versatility of Threose Nucleic Acids: Synthesis, Properties, and Applications in Chemical Biology and Biomedical Advancements. *Chem. Commun.* **2024**, *60* (83), 11864–11889.

(42) Yang, K.; McCloskey, C. M.; Chaput, J. C. Reading and Writing Digital Information in TNA. *ACS Synth. Biol.* **2020**, *9* (11), 2936–2942.

(43) Depmeier, H.; Kath-Schorr, S. Expanding the Horizon of the Xeno Nucleic Acid Space: Threose Nucleic Acids with Increased Information Storage. *J. Am. Chem. Soc.* **2024**, *146* (11), 7743–7751.

CHAPTER 1: Stability and mechanism of threose nucleic acid toward acid-mediated degradation

Erica M. Lee,[1] Noah A. Setterholm,[1] Mohammad Hajjar,[1] Bhawna Barpuzary,[1] and John C. Chaput[1-4]*

Affiliations

[1]Department of Pharmaceutical Sciences, University of California, Irvine, CA 92697-3958, United States

[2]Department of Chemistry, University of California, Irvine, CA 92697-3958, United States

[3]Department of Molecular Biology and Biochemistry, University of California, Irvine, CA 92697-3958, United States

[4]Department of Chemical and Biomolecular Engineering, University of California, Irvine, CA 92697-3958, United States

Chapter 1 is an adaptation of the material previously published in Nucleic Acids Research 2023, 51(18), 9542–9551 (https://doi.org/10.1093/nar/gkad716) used with permission from Oxford University Press (CC BY 4.0).

1.1 Abstract

Xeno-nucleic acids (XNAs) have gained significant interest as synthetic genetic polymers for practical applications in biomedicine, but very little is known about their biophysical properties. Here we compare the stability and mechanism of acid-mediated degradation of a-L-threose nucleic acid (TNA) to that of natural DNA and RNA. Under acidic conditions and elevated temperature (pH 3.3 at 90°C), TNA was found to be significantly more resistant to acid-mediated degradation than DNA and RNA. Mechanistic insights gained by reverse-phase HPLC and mass spectrometry indicate that the resilience of TNA toward low pH environments is due to a slower rate of depurination caused by induction of the 2'-phosphodiester linkage. Similar results observed for 2',5'-linked DNA and 2'-*O*-methoxy-RNA implicate the position of the phosphodiester group as a key factor in destabilizing the formation of the oxocarbenium intermediate responsible for depurination and strand cleavage of TNA. Biochemical analysis indicates that strand cleavage occurs by β-elimination of the 2'-phosphodiester linkage to produce an upstream cleavage product with a 2'-threose sugar and a downstream cleavage product with a 3' terminal phosphate. This work highlights the unique physicochemical properties available to evolvable non-natural genetic polymers currently in development for biomedical applications.

1.2 Introduction

Chemical modifications are critical to the development of oligonucleotide therapeutics, as natural DNA and RNA oligonucleotides rapidly degrade in biological environments (1,2). In the last 50 years, hundreds of changes have been made to the sugar, base, and phosphodiester backbone moieties of the molecule in an attempt to introduce molecular features that enhance the pharmacological properties of oligonucleotide therapeutics (3-6). This

large body of work has significantly improved our chemical understanding of how changes in oligonucleotide structure correlate with improvements in target recognition, RNA hybridization, and nuclease stability (7-9). Although most studies have focused on relatively subtle chemical changes made to DNA and RNA, including 2' substitutions (10), phosphodiester linkages (11), and alternative nucleobases (12,13), recent advances in nucleic acid chemistry have enabled the exploration of more diverse chemical architectures (14,15). Xeno-nucleic acids (XNA), artificial genetic polymers with backbone structures that are distinct from those found in nature (16), offer a promising new class of oligonucleotide therapeutics (17,18).

The unique physicochemical properties of XNA relative to natural DNA and RNA have attracted considerable attention as new materials for biomedicine (19,20). Favorable properties commonly attributed to XNAs include increased nuclease stability caused by their unnatural sugar-phosphate backbone structure and the potential for elevated thermodynamics of Watson-Crick base pairing. Locked nucleic acids (LNA), for example, are resistant to nuclease degradation and capable of increasing the melting temperature of DNA oligonucleotides by 4-8°C per residue when hybridized to complementary strands of RNA (21). XNAs are also thought to exhibit enhanced chemical stability, but detailed mechanistic studies evaluating their resilience under extreme conditions are lacking. One exception is 2'-fluoroarabino nucleic acid (FANA), which showed no signs of degradation after 2 days of incubation at 37°C in simulated gastric fluid (pH 1.2), under which conditions DNA and RNA degraded with half-lives ($t_{1/2}$) of 2 minutes and 3 hours, respectively (22). Since acid stability is known to be important for therapeutic delivery, especially endosomal escape (23), biochemical assays evaluating the mechanism and potential resistance to low pH environments are needed to guide the discovery of future XNA-based reagents.

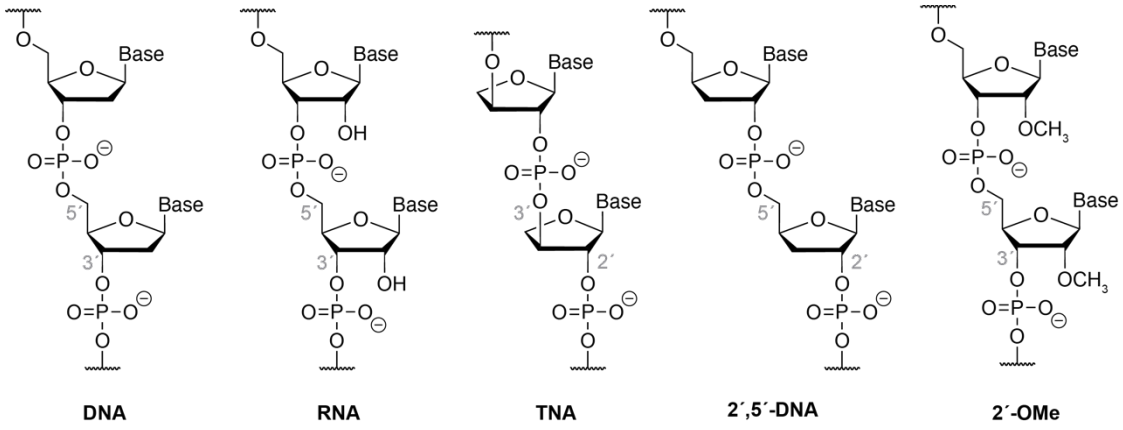

Figure 1.1. Chemical structures of the linearized backbones of DNA, RNA, TNA, 2',5'-linked DNA, and 2'-methoxy RNA. *a-L-threose nucleic acid (TNA) has one less atom in its backbone unit than DNA and RNA and shares an electron rich group at the 2' position with 2',5'-DNA and 2'-methoxy RNA.*

Here we examine the stability and mechanism of acid-mediated degradation of a specific type of XNA known as a-L-threose nucleic acid (TNA, Figure 1.1) (24). TNA has received significant interest as an evolvable artificial genetic polymer due to its 2',3'-phosphodiester linked backbone structure, which is refractory to nuclease digestion (25), yet still capable of forming stable antiparallel Watson-Crick duplex structures with complementary strands of DNA and RNA (24,26). Time course studies performed under acidic conditions and elevated temperature (pH 3.3 at 90°C) reveal that TNA is noticeably more pH stable than equivalent strands of natural DNA and RNA. Using 2',5'-linked DNA and 2'-*O*-methoxy-RNA (OMe), we show that the enhanced stability of TNA to low pH environments is due to the position of the 2'-phosphodiester linkage, which destabilizes formation of the oxocarbenium intermediate responsible for depurination and subsequent strand cleavage. Further biochemical studies indicate that depurination is rate limiting and that strand cleavage proceeds by β-elimination of the 2'-phosphodiester linkage as opposed to β-elimination of the 3'-phosphodiester linkage observed in DNA. These findings offer new insights into the beneficial properties of XNAs as they apply to future applications in XNA therapeutics.

1.3 Materials and Methods

Phosphoramidite preparation. DNA, 2',5'-linked DNA, and 2'-OMe RNA phosphoramidite monomers were purchased from Glen Research. TNA phosphoramidites with standard bases were obtained by chemical synthesis as previously described (27,28). The abasic TNA phosphoramidite with a photocleavable 1-(2-methyl)nitrophenethyl (NPE) group was obtained by chemical synthesis as detailed in the Supplementary Information. All nonaqueous reactions were performed using oven-dried glassware under inert gas atmosphere. All chemicals and solvents were of laboratory grade as obtained from commercial suppliers and were used without further purification. Thin-layer chromatography (TLC) was performed on TLC aluminum sheets covered with silica gel 60 F254 (Sigma-Aldrich, St. Louis, Missouri). Flash column chromatography (FC): SiliCycle 40-60 mesh silica gel (SiliCycle Inc., Quebec City, Canada). Yields are reported as isolated yields of pure compounds. ^{1}H, ^{13}C, and ^{31}P NMR spectra were obtained using Bruker DRX400 NMR spectrometer (Bruker, Billerica, Massachusetts). δ values in ppm relative to Me_4Si or corresponding deuterium solvents as internal standard (^{1}H and ^{13}C). ^{31}P NMR values are reported in ppm relative to an external standard of 85% H_3PO_4.

Oligonucleotide preparation. All oligonucleotides (Table S1) were synthesized in-house by solid-phase oligonucleotide synthesis on a 1 mmol scale, deprotected by 28% aqueous ammonium hydroxide for 18 hours at 55°C, and purified by using an oligonucleotide purification cartridge (OPC) and RP-HPLC, except for the RNA oligonucleotides and DNA standards, which were ordered from Integrated DNA Technologies (IDT). Oligonucleotides ordered from IDT were used without further purification. NPE-protected TNA oligonucleotides were dissolved in 200 μL of water to a final concentration of 200 μM and deprotected at room

temperature using an Analytik Jena UVP Crosslinker CL-1000L at an energy setting of 80 mJ/cm^2 for 7 minutes. Glen-Pak™ DNA Purification Cartridges were purchased from Glen Research. The Zorbax SB-C18 HPLC column (9.4 mm x 250 mm, 5 mM) for semi-preparative HPLC and Discovery C18 HPLC column (4.6 mm x 10 cm, 5 mM) for analytical HPLC were purchased from Agilent and Millipore Sigma, respectively.

Acid stability assay. Oligonucleotides were dissolved to a final concentration of 40 mM in 120 mM citrate phosphate buffer (pH 3.3) in a total reaction volume of 100 mL and heated at 90°C on a pre-heated heat block. At designated time points, the reactions were removed from the heat block, briefly vortexed, and allowed to cool (~2 min). In each case, aliquots of 20 mL were then taken from the reaction samples and quenched in 80 mL of 50 mM triethylammonium bicarbonate (TEAB) (pH 8.5) to a final concentration of 8 mM for analysis by RP-HPLC.

Acid stability analysis by RP-HPLC. RP-HPLC analysis was performed on a Discovery C18 HPLC column with buffer A as 50 mM TEAB (pH 8.5) and buffer B as acetonitrile. An increasing gradient of 0% to 20% buffer B was generated over 14 min with a flow rate of 1.00 mL/min at a set temperature of 40°C. The percent full-length product (%FLP) was determined as the relative area percentage under the absorbance curve at 260 nm calculated by the Chromeleon Chromatography Data System (CDS) Software. The %FLP at each time point was then divided by the %FLP at time point t=0 and multiplied by 100, normalizing the %FLP at t=0 to 100. The normalized values were then graphed in LabPlot2 and fitted to the exponential function ($y=ae^{bx}$) to calculate the half-lives. Additionally, $\ln[S]/[S_0]$ was plotted versus time and fit to a linear function of first order kinetics, where $[S]/[S_0]$ is the ratio of the remaining FLP to the starting FLP as determined by HPLC peak integration at the specified

time points. The rate constants for acid-mediated degradation were then obtained from the slope of the linear fit.

Mechanistic study of acid-mediated degradation. The oligonucleotide sequence used to study the degradation mechanism was 5'/3'-TTT TTT ATT TTT TTT T-3'/2'. The asymmetric oligonucleotide design (T_6 vs T_9) allowed for easy differentiation of the cleavage products by mass spectrometry. The depurination assay was performed in a manner identical to the acid stability assay with sample collection either up to the time point when the FLP was mostly degraded or 24 hours.

Acid-mediated degradation analysis by MALDI-TOF. The samples collected from the mechanistic study using the asymmetric sequence were desalted with ZipTip C18 pipette tips and pipetted directly onto a MALDI-TOF steel target plate (~1 mL). The spot on the plate was then dried by briefly heating at 55°C (~2 min) and covered with 1 μL of matrix (18 mg/mL 2,4,6-trihydroxy-acetophenone (THAP) and 6 mg/mL dibasic ammonium citrate in HPLC grade 50:50 MeCN/water) for characterization on a Bruker Daltronics Microflex MALDI-TOF mass spectrometer.

Molecular dynamics setup and simulations. A BespokeFit workflow was utilized using OpenFF Toolkit (https://github.com/openforce-field/openff-toolkit/tree/0.7.2) and OpenEye tools (OpenEye Scientific Software, Inc.) to generate and parameterize a force field for a ring-opened aldehyde TNA monomer using xTB (gfn2xtb) (27,28). OpenFF Interchange was used to create the initial topology and coordinates (https://github.com/openforcefield/openff-interchange). Molecular dynamics simulations were prepared and ran using GROMACS (v2022.1; gcc.8.4.0) as described by Lemkul, with discrepancies indicated subsequently (29,30). In brief, the molecule was solvated in a cubic water box (spc216) with periodic

boundary conditions in three dimensions and a buffering distance of 1 nm for a total of 856 water molecules treated using the SETTLE algorithm (31). A 50,000-step steepest descent energy minimization was performed on the monomer plateauing at -7.64e+05 kcal/mol. Initial velocities were generated from a Maxwell distribution at 363K. The system was equilibrated in a canonical ensemble (NVT) and then an isobaric-isothermic ensemble (NPT) for 100 ps each at 363K to stabilize the system. The production run was done for 10 ns, with a time step of 2 fs. Replicates of the simulation were performed starting from the same initial topology and coordinates created using Interchange. Dihedral angles were analyzed from trajectories using a custom script in PyMOL (v2.0, Schrödinger, LLC.) and visualized using Matplotlib (32).

1.4 Results and Discussion

The mechanism of acid-mediated DNA strand cleavage has been known for more than 50 years (33), and the susceptibility of RNA therapeutics to chemical degradation in low pH environments remains an important part of the drug discovery process (34). As illustrated in Figure 1.2, the exposure of DNA to low pH environments facilitates protonation of purine nucleotides at the *N*7 position **2**, and subsequent depurination via cleavage of the glycosidic bond **3**. However, we wish to point out that the first protonation site on adenosine occurs at the *N*1 position **1**, but this step is generally excluded from the mechanism because it does not weaken the glycosidic bond to the extent as protonation at the *N*7 position (35). The addition of water to the resulting oxocarbenium intermediate **4** of the abasic deoxyribose sugar leads to the formation of hemiacetal **5** that resides in equilibrium (99:1) with its ring-opened aldehyde form **6** (36). Despite its low abundance, aldehyde **7** is particularly sensitive to strand scission through an E2 elimination reaction that occurs via deprotonation of the

proton alpha to the aldehyde group. In the case of RNA, acid-mediated strand cleavage occurs via attack of the 2' hydroxyl on the protonated phosphate group (37). However, at pH values less than 3, acid-catalyzed depurination competes with phosphate hydrolysis (38), noting that depurination is slower for RNA than DNA due to the electronegative oxygen atom at the 2' position, which inductively destabilizes the oxocarbenium ion intermediate (39,40). Substitution of the 2' hydroxyl group for a more electronegative atom like, fluorine, further destabilizes the oxocarbenium intermediate, reducing its susceptibility to strand cleavage by depurination, as seen in 2'-fluorinated RNA (F-RNA) (41). This effect also accounts for the enhanced acid stability observed in FANA (22).

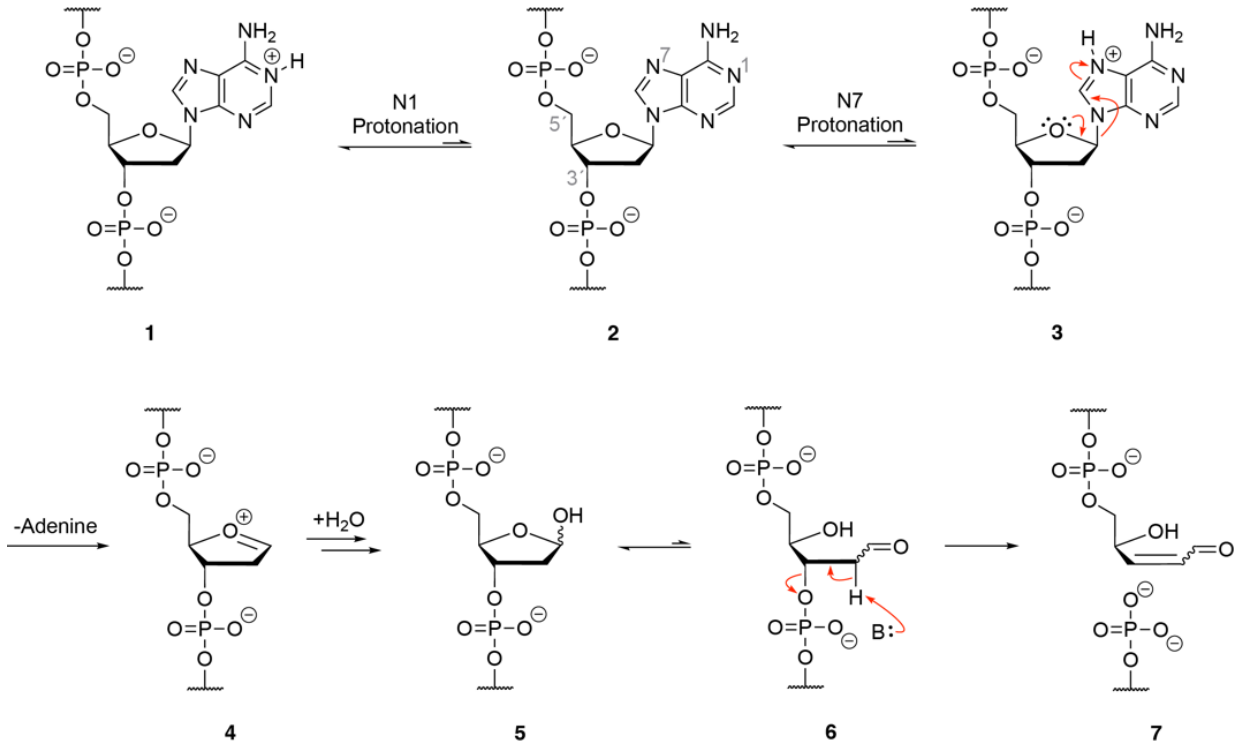

Figure 1.2. General mechanism of acid-mediated degradation of DNA. *Under acidic conditions, purine 2 is protonated at its N7 position, weakening the N-glycosidic bond of 3 and generating an abasic site after elimination of purine. A hemiacetal 5 is formed in equilibrium with its ring-opened aldehyde 6 form after hydration of the oxocarbenium ion 4. Strand scission occurs by an E2 elimination to produce an upstream cleavage product with a 3'-terminal aldehyde (7, top) and a downstream cleavage product with a 5'-terminal monophosphate (7, bottom).*

Based on the mechanism of acid-mediated DNA strand cleavage, we predicted that TNA would share a similar destabilizing effect on the oxocarbenium ion intermediate responsible for depurination as previously observed for F-RNA and FANA (22,41). To explore this prediction in greater detail, we compared the pH stability of a randomly generated 24 nucleotide (nt) sequence prepared as DNA, RNA, TNA, and 2',5'-linked DNA (Figure 1.1). Initial studies were performed using the DNA and TNA molecules to evaluate a range of conditions, including varying the pH, temperature, and incubation time. Since no degradation was observed for solutions held at 37°C (pH 4) for up to 48 hours, a full pH range of 4 – 10 was explored at 55°C. Under these conditions, TNA remained intact, while the DNA molecule showed noticeable signs of degradation after 24 hours of incubation at pH 4 (Supplementary Figure 1). For feasibility reasons, all subsequent stability studies were performed in 120 mM citrate phosphate buffer (pH 3.3) at 90°C, which allowed acid-mediated degradation to be monitored on a reasonable timescale. At designated time points, aliquots were removed, quenched with 0.05 M triethylammonium bicarbonate (TEAB) (pH 8.5), and directly analyzed by ion pair reverse phase high pressure liquid chromatography (RP-HPLC).

In the low pH high temperature environment, TNA was found to be more resistant than DNA and RNA toward acid-mediated chemical degradation. Half-life values ($t_{1/2}$) of 10.9 and 40.8 minutes were observed for DNA and RNA, which correspond to rate constants of 8.4×10^{-4} s^{-1} and 1.9×10^{-4} s^{-1}, respectively (Figure 1.3A, Supplementary Figure 2). By comparison, TNA with its unusual 2',3'-linked phosphodiester backbone, remained largely unmodified (> 90% of full-length product) after 1 hour of incubation with a calculated $t_{1/2}$ value of 6.3 hours and a rate constant of 3.3×10^{-5} s^{-1} (Figure 1.3A, Supplementary Figure 2). Postulating that the observed acid stability of TNA was due to the location of the phosphodiester

group at the 2' position as opposed to the more common 3' position found in DNA and RNA, we chose to compare TNA to a naturally occurring analog of DNA known as 2',5'-linked DNA (42), a product of the interferon regulated synthesis of 2',5'-oligoadenylate (43). Under the low pH and high temperature conditions, 2',5'-linked DNA exhibits a $t_{1/2}$ value of 9.9 hours with an observed rate constant of 2.5 x 10^{-5} s^{-1} (Figure 1.3B, Supplementary Figure 2), making it slightly more stable than TNA against acid-mediated degradation. Based on these results, the order of increasing stability observed for our randomly generated 24 nt sequence is DNA < RNA << TNA < 2',5'-DNA as visualized by RP-HPLC analysis (Figure 1.3C).

The enhanced stability observed for TNA and 2',5'-linked DNA strongly supports the hypothesis that the location of the phosphodiester linkage is important for stabilizing both genetic systems against acid-mediated chemical degradation. Although we suspect that the chemical underpinnings of the enhanced acid stability are due to destabilization of the oxocarbenium ion responsible for adenosine depurination and strand cleavage, we cannot dis-

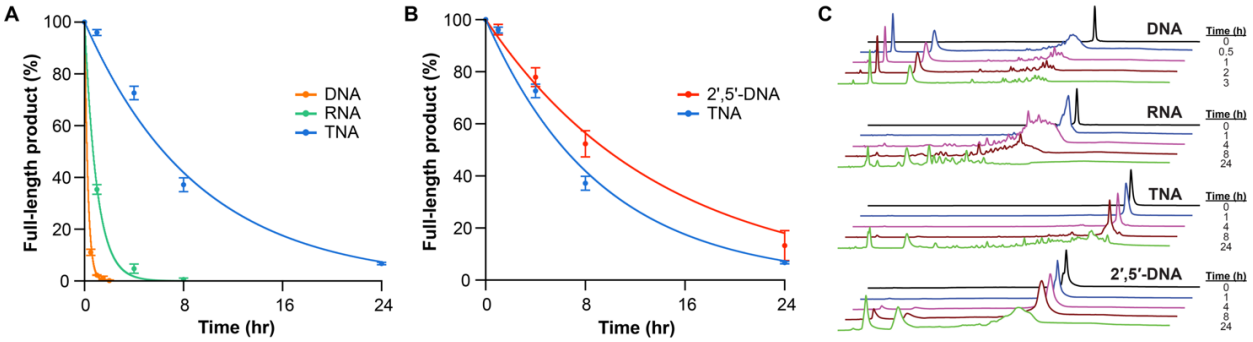

Figure 1.3. Time-dependent acid stability. *A-B) Acid-mediated oligonucleotide decay curves. Degradation profiles of DNA, RNA, TNA, and 2',5'-DNA oligonucleotides prepared with the same nucleotide sequence (5'/3'-CCGTAGTGAAAGATCCCTGTTCAG-3'/2') were monitored as a function of time by RP-HPLC. Error bars denote ± standard deviation of the mean for 3 independent replicates. All reactions were performed in 120 mM citrate phosphate buffer (pH 3.3) poised at 90°C. C) Representative reverse phase HPLC chromatograms observed for each genetic system show oligonucleotide degradation as a function of time.*

count the possibility that other steric or electronic effects may be contributing to the observed stability of TNA and 2',5'-linked DNA in a low pH environment. In an effort to gain deeper insight into the mechanism of acid-mediated degradation, we designed an asymmetric oligonucleotide sequence (T_6AT_9) that contained a central adenosine residue flanked by six thymidine residues on the 5' side and nine thymidine residues on the 3' side of the purine. The asymmetric design made it possible to follow the degradation pathway by standard analytical techniques of RP-HPLC and mass spectrometry. Oligonucleotides prepared with the T_6AT_9 sequence were incubated for various times in 120 mM citrate phosphate buffer (pH 3.3) at 90°C. Aliquots collected at desired times of the decay assay were quenched with 0.05 M TEAB (pH 8.5) and directly analyzed by RP-HPLC. Prior to HPLC analysis, a small portion of the sample was removed for mass spectrometry analysis.

Upon exposure to acid, we predicted that the asymmetric DNA oligonucleotide would degrade into two main cleavage products, 5'-dT_6-AP-3' and 5'-phos-dT_9-3' (Figure 1.4A, where AP signifies the depurinated residue), which is consistent with the classic E2 elimination mechanism proposed for acid-mediated DNA strand cleavage (Figure 1.4B) (33,34). After 200 minutes of incubation at 90°C (pH 3.3), two large peaks were observed in the RP-HPLC traces, along with several smaller peaks (Figure 1.4C, Supplementary Figure 3). Mass spectrometry analysis identified the two large peaks as the depurinated form of the T_6AT_9 strand and the downstream cleavage product of 5'-phos-dT_9-3' (Supplementary Figure 4). The depurinated T_6AT_9 intermediate was detected as the dehydrated form, which is likely due to MALDI-TOF analysis. Most of the smaller peaks observed in the RP-HPLC trace were identified using a combination of authentic standards and mass spectrometry (Figure 1.4C, Supplementary Figure 4). The smaller peaks are primarily the result of further degradation

of the 5'-dT_6-AP-3' and 5'-phos-dT_9-3' fragments, including the 5'-dT_6-phos-3' and 5'-dT_6-3' intermediates from the upstream cleavage product and the 5'-dT_9-3' intermediate from the downstream cleavage product. Although the upstream product (5'-dT_6-AP-3') was not observed by HPLC, this intermediate was detected by mass spectrometry (Supplementary Figure 4). Interestingly, a control experiment performed with 5'-phos-dT_9-3' confirmed that dephosphorylation occurs under the low pH conditions (Supplementary Figure 5), indicating

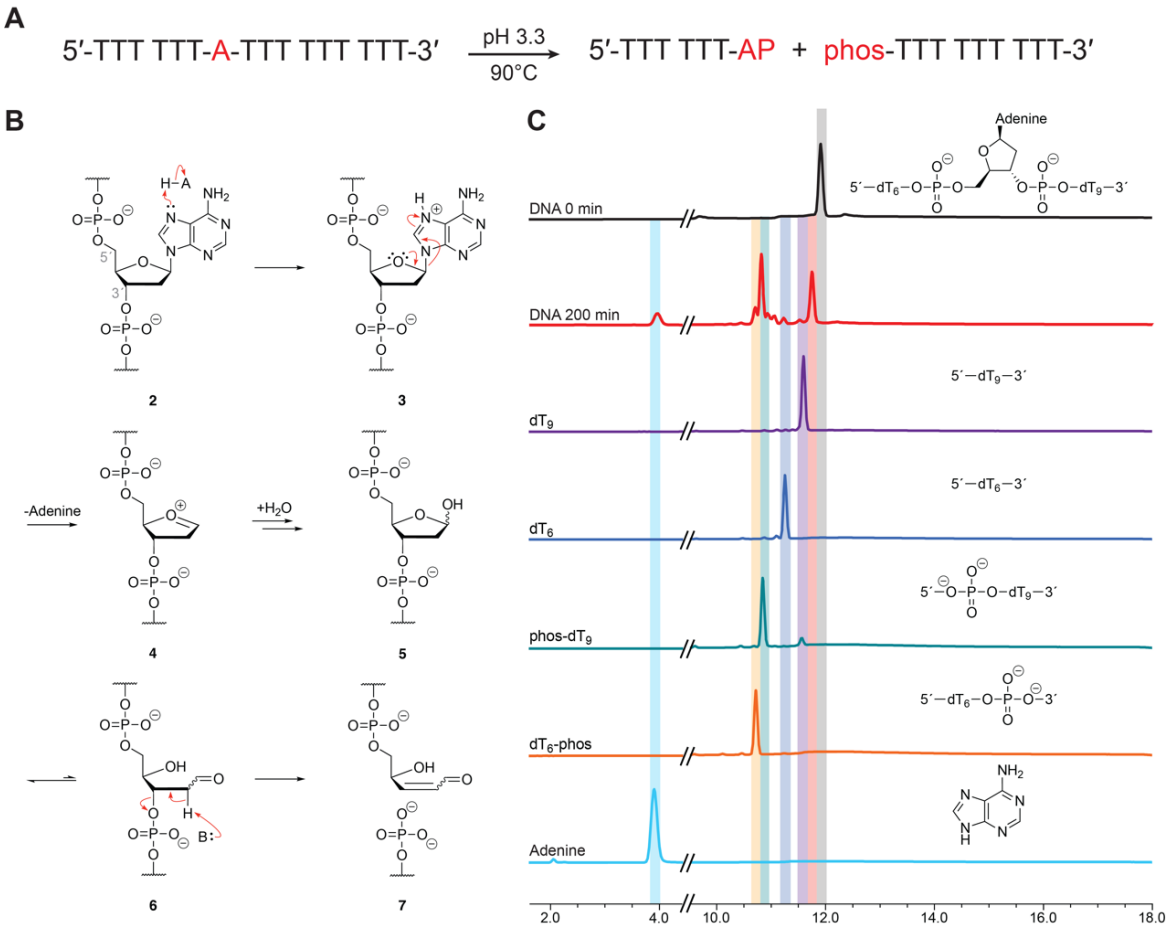

Figure 1.4. Mechanism of acid-mediated DNA strand cleavage. *A) Asymmetric oligonucleotide design. Acid-mediated cleavage results in an upstream cleavage product with a 3' terminal abasic site (AP) and a downstream product with a 5'-monophosphate (phos). B) Degradation involves the formation of an abasic strand that undergoes ring opening and strand cleavage via E2 elimination of the 3'-phosphodiester linkage. C) Representative reverse phase HPLC chromatograms comparing the 5'-d(T_6AT_9)-3' strand before and after 200 minutes of acid treatment to authentic standards prepared for key intermediates.*

that multiple different hydrolysis reactions are taking place as the initial cleavage products undergo further decay. Time-dependent studies show that depurination is rapid for the asymmetric DNA sequence (Supplementary Figure 3), suggesting that adenine departure is the fast step of acid-mediated DNA degradation.

A similar mechanistic study was performed on the asymmetric sequence prepared as TNA. This genetic system was more difficult to analyze due to the presence of phosphodiester linkages at both the 2' and 3' positions of the sugar. As such, it was unclear whether strand scission would occur via elimination of the 3' phosphodiester linkage, as is commonly observed for DNA and RNA, or through a novel degradative pathway involving elimination of the 2' phosphodiester linkage (Figure 1.5A-B). Time-dependent HPLC traces collected over a 22-hour period of incubation at 90°C (pH 3.3) yielded the full-length T_6AT_9 sequence with several smaller peaks (Figure 1.5C). RP-HPLC comparisons performed with authentic standards (Figure 1.5C) identified two of the smaller peaks as the phosphorylated and dephosphorylated forms of the downstream 2' cleavage product (3'-phos-tT_9-2' and 3'-tT_9-2'). We confirmed that the 3'-tT_9-2' intermediate can form under the current conditions by evaluating the decay profile for an authentic standard of 3'-phos-tT_9-2' prepared by solid-phase synthesis (Supplementary Figure 5B).

To better understand the mechanism of TNA degradation, we used mass spectrometry to identify additional intermediates that were present at levels below the analytical limit of detection for HPLC analysis. In addition to the downstream intermediates previously identified by RP-HPLC, mass spectrometry confirmed the presence of various upstream degradative products including the abasic derivative, 3'-tT_6-AP-2' and its deglycosylated form (Sup-

plementary Figure 6). This result implies that acid-mediated TNA degradation primarily occurs via elimination of the 2' phosphodiester linkage with depurination being the rate limiting step of degradation (Figure 1.5A-B). Additionally, we also observe what appears to be evidence of a competing *syn*-elimination pathway via addition of the anomeric hydroxyl group to the 2'-phosphodiester linkage (Supplementary Figure 7), resulting in a product with an observed mass of 1961.4 (Supplementary Figure 6). However, given the small size

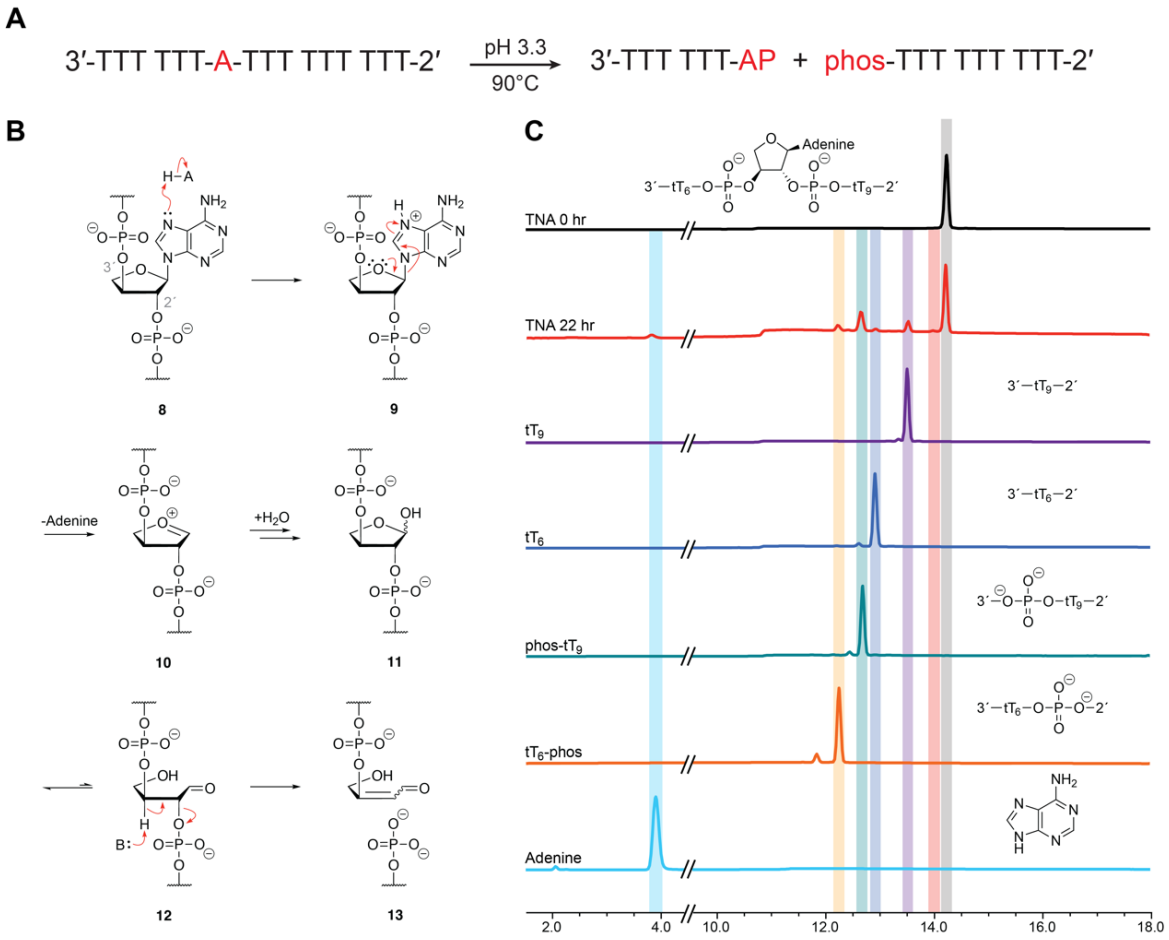

Figure 1.5. Mechanism of acid-mediated TNA strand cleavage. *A) Asymmetric oligonucleotide design. Acid-mediated cleavage results in an upstream cleavage product with a 2'-terminal abasic site (AP) and a downstream product with a 3'-monophosphate (phos). B) Degradation involves the formation of an abasic strand that undergoes ring opening and strand cleavage via β-elimination of the 2'-phosphodiester linkage. C) Representative reverse phase HPLC chromatograms comparing the 5'-t(T_6AT_9)-3' strand before and after 22 hours of acid treatment to authentic standards prepared for key intermediates.*

of this peak in the abasic TNA control assay (see Supplementary Figure 9), we postulate that *syn*-elimination is a minor pathway as compared to β-elimination.

To further evaluate the cleavage mechanism, we prepared and analyzed the abasic intermediate (tT_6-tAP-tT_9, where tAP signifies the abasic residue) that arises following depurination of the asymmetric TNA strand. The TNA oligonucleotide was synthesized using a novel abasic TNA phosphoramidite that was prepared by chemical synthesis following methodology that was previously established for RNA (Figure 1.6A) (44). The abasic phosphoramidite **19** was prepared from racemic 1-(2-nitrophenyl)ethan-1-ol **14** as the glycosyl acceptor and a fully protected a-L threofuranosyl sugar **15** as the glycosyl donor. In presence of trimethylsilyl trifluoromethanesulfonate (TMSOTf) in CH_3CN at −35°C, the reaction produced a diastereomeric mixture of glycosylated products. After removal of the 3'-O-TBDPS group, the glycosylated products were separated by silica gel column chromatography to give **16a** and **16b** in a total yield of 49% for the two steps. The structure of **16a** was confirmed by comparing the ^{1}H NMR of the corresponding product obtained from enantiopure (*R*)-1-(2-nitrophenyl)ethan-1-ol. Since we were not concerned about the stereochemistry, compound **16b** was selected based on purity and converted to the desired phosphoramidite **19** by protection of 3'-OH group with 4,4'-dimethoxytritylchloride (DMTCl), removal of the 2′ benzoyl group with 1M NaOH, and treatment of **18** with 2,2-cyanoethyl-*N*,*N*-diisopropylchlorophosphoramidite in the presence of Hünig's base. The TNA phosphoramidite **19** was then incorporated into the asymmetric sequence by solid-phase synthesis, and the final abasic TNA oligonucleotide was obtained after deprotection of the NPE group by UV irradiation (Supplementary Figure 8).

Time-dependent HPLC and mass spectrometry analysis of the abasic TNA strand indicate that strand cleavage is complete by 2 hours (Figure 1.6B), while the equivalent adenosine-containing TNA strand remains mostly undegraded (> 90%) after 22 hours of incubation (Figure 1.6C). The difference in the rates of degradation between the abasic control and standard base TNA strand confirms that depurination is the rate limiting step of acid-mediated TNA degradation. Mass spectrometry analysis of the abasic strand identified the ex-

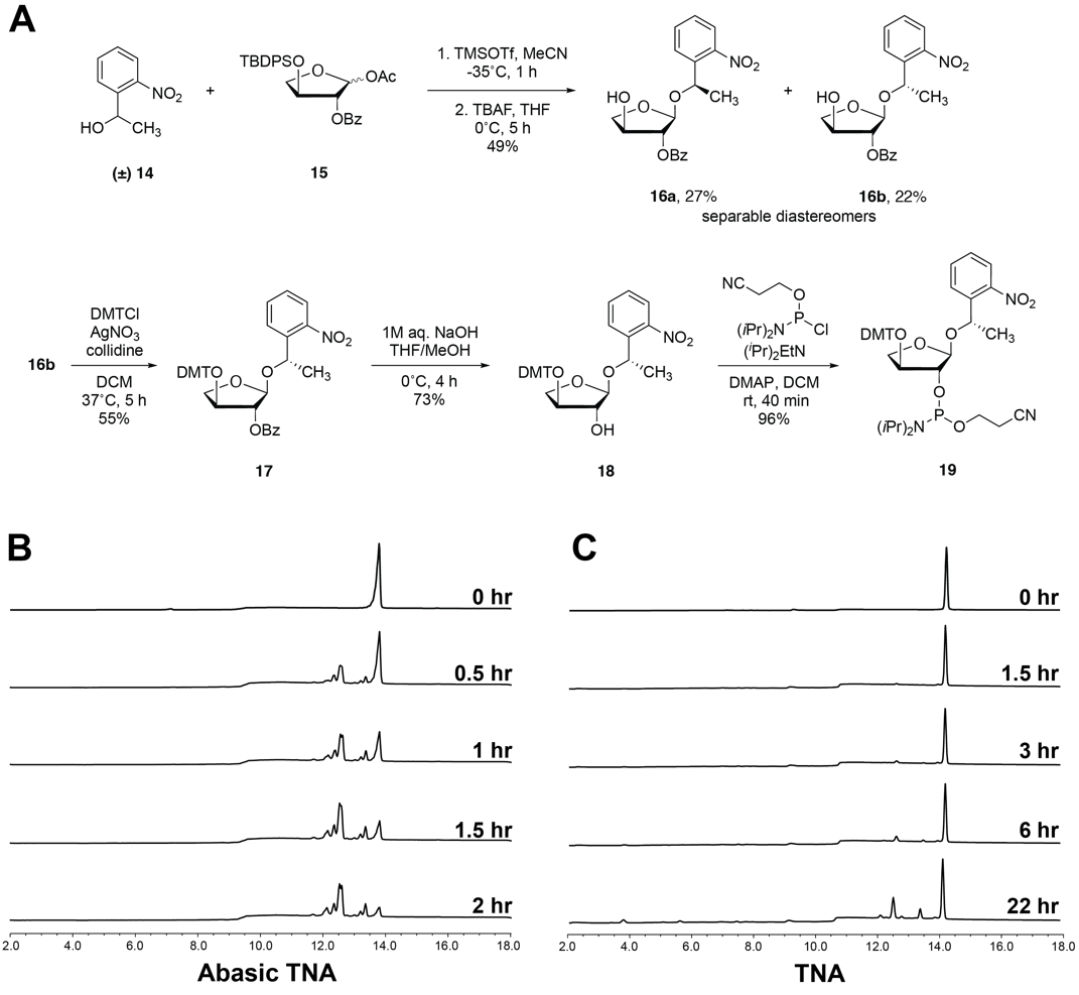

Figure 1.6. Synthesis and evaluation of an abasic TNA toward acid-mediated TNA degradation. *A) Reaction scheme used to prepare the abasic TNA phosphoramidite. B-C) Time-dependent HPLC analysis of acid-mediated degradation of an abasic TNA strand (tT_6-tAP-tT_9, where tAP signifies the abasic residue) versus an all-TNA strand (tT_6-tA-tT_9). The abasic TNA strand shows faster degradation kinetics than the all-TNA strand under the same reaction conditions (pH 3.3 at 90°C).*

pected cleavage products, 3'-tT_6-AP-2' and 3'-phos-tT_9-2', along with the same minor products previously observed for the adenosine-containing strand (Supplementary Figure 9). Although the abasic TNA strand contained trace amounts of the n-1 and n-2 as byproducts from solid-phase synthesis, their presence did not affect the results of the assay. In fact, MALDI-TOF analysis showed that the n-1 byproduct degrades in a manner similar to the full-length product (Supplementary Figure 9). Importantly, mass spectrometry analysis did not identify the 3'-AP-tT_9-2' intermediate, providing further evidence for strand cleavage via β-elimination of the 2'-phosphodiester linkage.

In an effort to gain insight into the regioselectivity of the elimination mechanism in TNA, we evaluated a TNA monomer in its ring-opened aldehyde form in water at 363K (90°C) via 10 ns molecular dynamics simulations. Torsion analysis about the C3'-C2' bond revealed that protons HC3' and HC2' (denoted H_a and H_b, respectively) are virtually antiperiplanar to

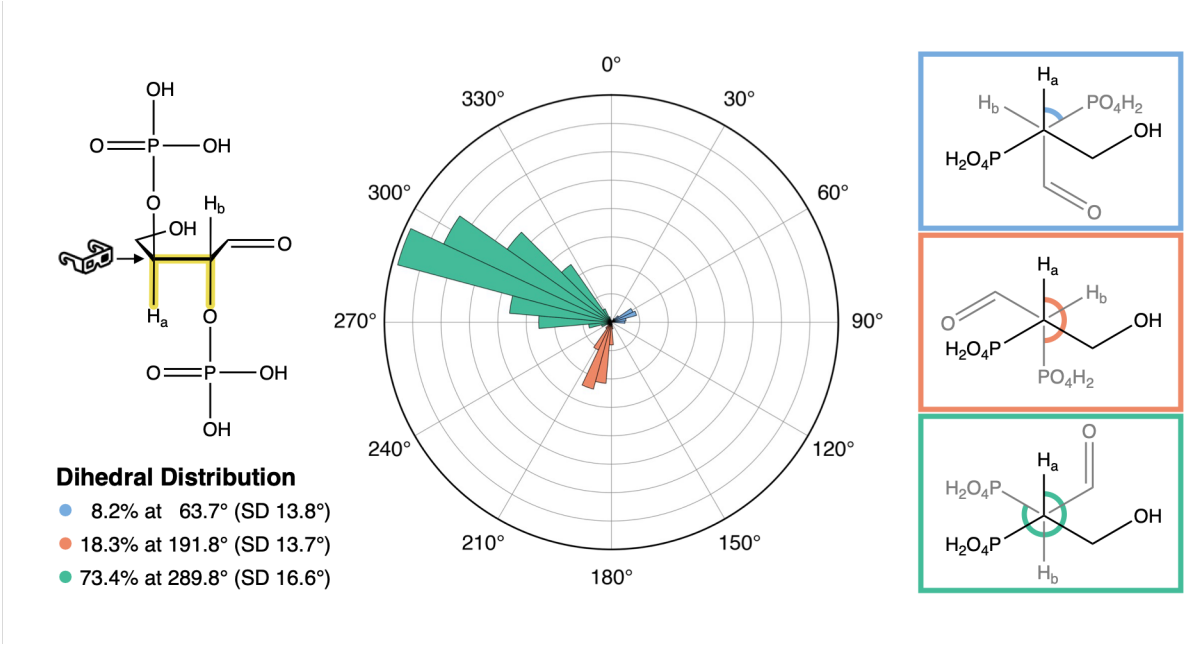

Figure 1.7. Conformational sampling via molecular dynamics. *The dihedral distribution about the highlighted bond (H – C3' – C2' – O) is plotted following a 10 ns molecular dynamics simulation of the ring-open aldehyde TNA fragment in water. Newman projections are depicted for angles 60°, 180°, and 300°. Additional replicates of the 10 ns simulation are reported in Supplementary Figure 11.*

their corresponding phosphates during 22.9 ± 2.7% of the time sampled (Figure 1.7, Supplementary Figure 11). While feasible, both protons are concomitantly *anti* to the corresponding phosphates with no clear structurally favorable path of elimination. While we cannot exclude possible steric and electronic effects of the full oligonucleotide strand on the preferred conformation for elimination, it is evident that there is preference toward elimination of the 2' phosphodiester linkage based on our analytical HPLC and mass spectrometry data.

1.5 Conclusion

In summary, our results demonstrate that TNA is significantly more resistance to acid-mediated degradation than natural DNA and RNA. Mechanistic studies suggest that the enhanced stability is due to inductive destabilization of the oxocarbenium intermediate, which is analogous to previous studies on 2'-methoxy-RNA and consistent with our control experiments on 2',5'-DNA. We further show that acid-mediated strand cleavage in TNA occurs via β-elimination of the 2'-phosphodiester linkage rather than the 3’-phosphodiester linkage observed for DNA, illustrating the complexity of the chemistry behind the properties of artificial genetic polymers. These observations offer further insight into the unique biophysical properties of XNAs and provide further support for expanding the use of artificial genetic polymers in biomedical applications involving extreme conditions that are not suitable for DNA and RNA.

1.6 Data Availability

All data are available upon reasonable request.

1.7 Funding

This work was supported by grants from the National Science Foundation (CHM: 2001434 and MCB: 1946312).

1.8 Conflict of Interest

The authors declare no competing financial interests.

1.9 Acknowledgements

We wish to thank members of the Chaput lab for their helpful comments on the manuscript; D. Mobley, A. Caldaruse, and A. Nandkeolyar for help with computational modeling; and OpenEye Scientific Academic Licensing (https://www.eyesopen.com) for their open-source software and tools. This work utilized the infrastructure for high-performance and high-throughput computing, research data storage and analysis, and scientific software tool integration built, operated, and updated by the Research Cyberinfrastructure Center (RCIC) at the University of California, Irvine (UCI). The RCIC provides cluster-based systems, application software, and scalable storage to directly support the UCI research community (https://rcic.uci.edu).

1.10 Author Contributions

E.L., N.S., and J.C. conceived the study and designed the research plan. E.L. and N.S. performed the chemical synthesis and purification of the TNA oligonucleotides. E.L. performed the acid stability experiments. M.H. performed the molecular dynamics simulation. B.B. performed the chemical synthesis and purification of the abasic TNA phosphoramidite. E.L. and J.C. wrote the manuscript with input from all authors.

1.11 References

(1) Griffin, L.C., Tidmarsh, G.F., Bock, L.C., Toole, J.J. and Leung, L.L. (1993) In vivo anticoagulant properties of a novel nucleotide-based thrombin inhibitor and demonstration of regional anticoagulation in extracorporeal circuits. *Blood*, **81**, 3271-3276.

(2) Kratschmer, C. and Levy, M. (2017) Effect of Chemical Modifications on Aptamer Stability in Serum. *Nucleic Acid Ther.*, **27**, 335-344.

(3) Freier, S.M. and Altmann, K.-H. (1997) The ups and downs of nucleic acid duplex stability: structure-stability studies on chemically modified DNA:RNA duplexes. *Nucleic Acids Res.*, **25**, 4429-4443.

(4) McKenzie, L.K., El-Khoury, R., Thorpe, J.D., Damha, M.J. and Hollenstein, M. (2021) Recent progress in non-native nucleic acid modifications. *Chem. Soc. Rev.*, **50**, 5126-5164.

(5) Deleavey, G.F. and Damha, M.J. (2012) Designing chemically modified oligonucleotides for targeted gene silencing. *Chem. Biol.*, **19**, 937-954.

(6) Burnett, J.C. and Rossi, J.J. (2012) RNA-based therapeutics: current progress and future prospects. *Chem. Biol.*, **19**, 60-71.

(7) Khvorova, A. and Watts, J.K. (2017) The chemical evolution of oligonucleotide therapies of clinical utility. *Nat. Biotechnol.*, **35**, 238-248.

(8) Bennett, C.F. (2019) Therapeutic Antisense Oligonucleotides Are Coming of Age. *Annu Rev Med*, **70**, 307-321.

(9) Keefe, A.D., Pai, S. and Ellington, A.D. (2010) Aptamers as therapeutics. *Nat. Rev. Drug Discov.*, **9**, 537-550.

(10) Prakash, T.P. and Bhat, B. (2007) 2'-Modified oligonucleotides for antisense therapeutics. *Curr Top Med Chem*, **7**, 641-649.

(11) Nawrot, B., Widera, K., Wojcik, M., Rebowska, B., Nowak, G. and Stec, W.J. (2007) Mapping of the functional phosphate groups in the catalytic core of deoxyribozyme 10-23. *FEBS J*, **274**, 1062-1072.

(12) Hoshika, S., Leal, N.A., Kim, M.J., Kim, M.S., Karalkar, N.B., Kim, H.J., Bates, A.M., Watkins, N.E., Jr., SantaLucia, H.A., Meyer, A.J. *et al.* (2019) Hachimoji DNA and RNA: A genetic system with eight building blocks. *Science*, **363**, 884-887.

(13) Krueger, A.T. and Kool, E.T. (2009) Redesigning the architecture of the base pair: toward biochemical and biological function of new genetic sets. *Chem. Biol.*, **16**, 242-248.

(14) Eschenmoser, A. (1999) Chemical etiology of nucleic acid structure. *Science*, **284**, 2118-2124.

(15) Chaput, J.C. (2021) Redesigning the Genetic Polymers of Life. *Acc. Chem. Res.*, **54**, 1056-1065.

(16) Chaput, J.C. and Herdewijn, P. (2019) What Is XNA? *Angew. Chem. Int. Ed. Engl.*, **58**, 11570-11572.

(17) Anosova, I., Kowal, E.A., Dunn, M.R., Chaput, J.C., Van Horn, W.D. and Egli, M. (2016) The structural diversity of artificial genetic polymers. *Nucleic Acids Res.*, **44**, 1007-1021.

(18) Duffy, K., Arangundy-Franklin, S. and Holliger, P. (2020) Modified nucleic acids: replication, evolution, and next-generation therapeutics. *BMC Biol*, **18**, 112.

(19) Morihiro, K., Kasahara, Y. and Obika, S. (2017) Biological applications of xeno nucleic acids. *Mol. Biosyst.*, **13**, 235-245.

(20) Tu, T., Huan, S., Ke, G. and Zhang, X. (2022) Functional Xeno Nucleic Acids for Biomedical Application. *Chem Res Chin Univ*, 1-7.

(21) Campbell, M.A. and Wengel, J. (2011) Locked vs. unlocked nucleic acids (LNA vs. UNA): contrasting structures work towards common therapeutic goals. *Chem. Soc. Rev.*, **40**, 5680-5689.

(22) Watts, J.K., Katolik, A., Viladoms, J. and Damha, M.J. (2009) Studies on the hydrolytic stability of 2'-fluoroarabinonucleic acid (2'F-ANA). *Org. Biomol. Chem.*, **7**, 1904-1910.

(23) Dowdy, S.F. (2017) Overcoming cellular barriers for RNA therapeutics. *Nat. Biotechnol.*, **35**, 222-229.

(24) Schöning, K.U., Scholz, P., Guntha, S., Wu, X., Krishnamurthy, R. and Eschenmoser, A. (2000) Chemical etiology of nucleic acid structure: the a-threofuranosyl-(3'-->2') oligonucleotide system. *Science*, **290**, 1347-1351.

(25) Culbertson, M.C., Temburnikar, K.W., Sau, S.P., Liao, J.-Y., Bala, S. and Chaput, J.C. (2016) Evaluating TNA stability under simulated physiological conditions. *Bioorg. Med. Chem. Lett.*, **26**, 2418-2421.

(26) Yang, Y.-W., Zhang, S., McCullum, E.O. and Chaput, J.C. (2007) Experimental evidence that GNA and TNA were not sequential polymers in the prebiotic evolution of RNA. *J. Mol. Evol.*, **65**, 289-295.

(27) Horton, J.T., Boothroyd, S., Wagner, J., Mitchell, J.A., Gokey, T., Dotson, D.L., Behara, P.K., Ramaswamy, V.K., Mackey, M., Chodera, J.D. *et al.* (2022) Open Force Field BespokeFit: Automating Bespoke Torsion Parametrization at Scale. *J Chem Inf Model*, **62**, 5622-5633.

(28) Bannwarth, C., Caldeweyher, E., Ehlert, S., Hansen, A., Pracht, P., Seibert, J., Spicher, S. and Grimme, S. (2021) Extended tight-binding quantum chemistry methods. *WIREs Computational Molecular Science*, **11**, e1493.

(29) Abraham, M.J., Murtola, T., Schulz, R., Páll, S., Smith, J.C., Hess, B. and Lindahl, E. (2015) GROMACS: High performance molecular simulations through multi-level parallelism from laptops to supercomputers. *SoftwareX*, **1**, 19-25.

(30) Lemkul, J.A. (2018) From proteins to perturbed hamiltonians: A suite of tutorials for the GROMACS-2018 molecular simulation package [article v1. 0]. *Living Journal of Computational Molecular Science*, **1**, 33011.

(31) Miyamoto, S. and Kollman, P.A. (1992) Settle - an Analytical Version of the Shake and Rattle Algorithm for Rigid Water Models. *J. Comput. Chem.*, **13**, 952-962.

(32) Hunter, J.D. (2007) Matplotlib: A 2D graphics environment. *Comput Sci Eng*, **9**, 90-95.

(33) Zoltewicz, J.A., Clark, D.F., Sharpless, T.W. and Grahe, G. (1970) Kinetics and mechanism of the acid-catalyzed hydrolysis of some purine nucleosides. *J. Am. Chem. Soc.*, **92**, 1741-1749.

(34) Pogocki, D. and Schoneich, C. (2000) Chemical stability of nucleic acid-derived drugs. *J Pharm Sci*, **89**, 443-456.

(35) Hotokka, M. and Lonnberg, H. (1996) Hydrolysis of adenosine. A semiempirical and ab initio study. *J Mol Struc-Theochem*, **363**, 191-201.

(36) Wilde, J.A., Bolton, P.H., Mazumder, A., Manoharan, M. and Gerlt, J.A. (1989) Characterization of the Equilibrating Forms of the Aldehydic Abasic Site in Duplex DNA by O-17 Nmr. *J. Am. Chem. Soc.*, **111**, 1894-1896.

(37) Oivanen, M., Kuusela, S. and Lonnberg, H. (1998) Kinetics and Mechanisms for the Cleavage and Isomerization of the Phosphodiester Bonds of RNA by Bronsted Acids and Bases. *Chem. Rev.*, **98**, 961-990.

(38) Jarvinen, P., Oivanen, M. and Lonnberg, H. (1991) Interconversion and Phosphoester Hydrolysis of 2',5'-Dinucleoside and 3',5'-Dinucleoside Monophosphates - Kinetics and Mechanisms. *J. Org. Chem.*, **56**, 5396-5401.

(39) Garrett, E.R. and Mehta, P.J. (1972) Solvolysis of adenine nucleosides. I. Effects of sugars and adenine substituents on acid solvolyses. *J. Am. Chem. Soc.*, **94**, 8532-8541.

(40) York, J.L. (1981) Effect of the Structure of the Glycon on the Acid-Catalyzed Hydrolysis of Adenine Nucleosides. *J. Org. Chem.*, **46**, 2171-2173.

(41) Barchi, J.J., Jr., Karki, R.G., Nicklaus, M.C., Siddiqui, M.A., George, C., Mikhailopulo, I.A. and Marquez, V.E. (2008) Comprehensive structural studies of 2',3'-difluorinated nucleosides: comparison of theory, solution, and solid state. *J. Am. Chem. Soc.*, **130**, 9048-9057.

(42) Jung, K.-E. and Switzer, C. (1994) 2',5'-DNA containing guanine and cytosine forms stable duplexes. *J. Am. Chem. Soc.*, **116**, 6059-6061.

(43) Justesen, J., Ferbus, D. and Thang, M.N. (1980) Elongation mechanism and substrate specificity of 2',5'-oligoadenylate synthetase. *Proc. Natl. Acad. Sci. U.S.A.*, **77**, 4618-4622.

(44) Jacobs, A.C., Resendiz, M.J. and Greenberg, M.M. (2011) Product and mechanistic analysis of the reactivity of a C6-pyrimidine radical in RNA. *J. Am. Chem. Soc.*, **133**, 5152-5159.

(45) Furukawa, Y., Kobayashi, K., Kanai, Y. and Honjo, M. (1965) Synthesis of 2'-O-methyluridine, 2'-O-methylcytidine and their relating compounds. *Chem Pharm Bull (Tokyo)*, **13**, 1273-1278.

CHAPTER 2: Allele-Specific Knockdown by an Engineered DNAzyme Capable of RNase H1 Evasion

Erica M. Lee[1†], Kim Nguyen[1†], Noah A. Setterholm[1], Turnee N. Malik[1], and John C. Chaput[1-4*]

[†]These authors contributed equally

Affiliations

[1]Department of Pharmaceutical Sciences, University of California, Irvine, CA 92697, United States

[2]Department of Chemistry, University of California, Irvine, CA 92697, United States

[3]Department of Molecular Biology and Biochemistry, University of California, Irvine, CA 92697, United States

[4]Department of Chemical and Biomolecular Engineering, University of California, Irvine, CA 92697, United States

Chapter 2 is an adaptation of the material previously published in Nucleic Acids Research 2026, 54(1), gkaf1476 (https://doi.org/10.1093/nar/gkaf1476) used with permission from Oxford University Press (CC BY 4.0).

2.1 Abstract

DNA enzymes (DNAzymes) offer an attractive therapeutic approach for targeting disease-associated mutations in mRNA transcripts, but face limitations in development due to unintended engagement by RNase H1. Although chemical optimization has led to designs with improved catalytic activity, strategies to mitigate RNase H1 recognition remain underexplored. Here, we report the incorporation of threose nucleic acid (TNA) into the backbone architecture of the 10-23 DNAzyme variant known as Dz46. Substitution of the dC3 position in the catalytic loop with TNA increases activity, whereas installation of two TNA residues in the binding arm abrogates competition by RNase H1. The resulting enzyme enables allele-specific knockdown of an oncogenic KRAS mutation in mammalian cells and facilitates general knockdown of PCSK9 and GATA3 targets. Together, these results demonstrate the utility of TNA as a chemical tool for enhancing DNAzyme performance and evading RNase H1 activity in cells.

2.2 Introduction

RNA-cleaving DNA enzymes (DNAzymes) represent a powerful class of gene silencing agents that combine the programmability of antisense oligonucleotides (ASOs) with the catalytic potential of ribozymes (1,2). Among the set of nucleic acid enzymes developed to date, 10–23 remains the most widely studied example due to its simple architecture, programmable binding arms, and ability to precisely catalyze site-specific cleavage at purine–pyrimidine junctions, most effectively at G–U dinucleotide junctions (3-5). Yet despite their mechanistic appeal and favorable safety profile (6), DNAzymes have faced significant obstacles to therapeutic translation (7). This problem is primarily due to their limited catalytic activity under physiological conditions where the concentration of free magnesium (Mg^{2+}) is limiting (8),

and unintended engagement by RNase H1, a cellular enzyme that utilizes the binding arms to cleave RNA following an antisense mechanism (9-11).

Allele-specific knockdown has long been a highly sought-after goal in precision medicine. In particular, there is great interest in recognizing and selectively targeting alleles that carry disease-causing single-point mutations (SNPs), which account for more than half of all disease-associated genetic mutations (12). Although ASOs and small-interfering RNAs (siRNAs) have made significant progress toward this objective (13-15), additional work is needed to develop reagents that are generalizable and broadly applicable across the transcriptome. While protein-based gene silencing agents remain the foundation of most FDA-approved technologies (16), the intrinsic ability of DNAzymes to recognize specific dinucleotide junctions offers compelling reason for their continued development as allele-specific gene silencing agents (7).

Chemical evolution offers a powerful approach for improving the performance of oligonucleotide therapeutics (16,17). Chemical modifications, particularly the incorporation of xeno-nucleic acids (XNAs) (18,19), such as 2′-*O*-methoxy ribonucleic acid (OMe) (20), locked nucleic acid (LNA) (21), and 2′-fluoroarbino nucleic acid (FANA) (22) into the backbone structure of in vitro selected DNAzymes have yielded chemically-modified versions of the wild-type sequence that function with enhanced catalytic activity, chemical stability, and biocompatibility (23-29). These synthetic chemotypes have been deployed to increase nuclease stability and to enhance RNA cleavage activity (23-32). Dz46, a chemically modified version of the classic 10-23 DNAzyme (Figure 2.1a), was found to achieve ~65 turnovers in 30 minutes under physiological conditions, comparing favorably to the unmodified DNA sequence under forcing conditions of 50 mM $MgCl_2$ (pH 8.0) (25). However, despite a high level

of chemical modification, Dz46 is still recognized by RNase H1, indicating that further modifications are needed to achieve autonomous cleavage activity in cells.

Here we explore the use of a-L-threofuranosyl nucleic acid (TNA, Figure 2.1a) as an approach for modulating DNAzyme activity. We show that TNA substitution at the dC3 position of the catalytic core of Dz46 enhances activity, while dual TNA substitutions made to the binding arm abrogate RNase H1-mediated strand cleavage. RNA and protein knockdown assays performed in mammalian cells endogenously expressing heterozygous and homozygous alleles of wild-type and mutant KRAS G12V provide strong evidence of a DNAzyme-mediated RNA cleavage mechanism that functions independent of RNase H1 engagement. Additionally, Dz46 was shown to function with general knockdown activity against PCSK9 and GATA3. Together, these findings highlight the potential of TNA as a nucleic acid analog for engineering DNAzymes with improved cellular activity and provide a framework for leveraging XNA chemistry in the development of next-generation oligonucleotide therapeutics.

2.3 Materials and Methods

General information. Oligonucleotides were synthesized in-house by solid-phase oligonucleotide synthesis on a Dr. Oligo 48 DNA synthesizer (Biolytic) or purchased from Integrated DNA Technologies (Coralville, Iowa). DNA, LNA, 2′-OMe RNA, MOE RNA phosphoramidites were purchased from Glen Research (Sterling, Virginia). TNA phosphoramidites were obtained by chemical synthesis as previously described (33). Glen-Pak DNA Purification Cartridges were purchased from Glen Research. The Zorbax SB-C18 HPLC column (9.4 mm x 250 mm, 5 mM) for semi-preparative HPLC and Discovery C18 HPLC column (4.6 mm x 10 cm, 5 mM) for analytical HPLC were purchased from Agilent and Millipore Sigma, respectively. Full-length recombinant human RNase H1 was purchased from Abcam (Cat# Ab153634).

RNase T1 was purchased from Thermo Fisher Scientific (Cat# EN0541). Dulbecco's Modified Eagle Medium (DMEM) was purchased from Thermo Fisher Scientific (Cat# 10-017-CM; Waltham, MA). RPMI 1640 medium was purchased from ATCC (Cat# ATCC 30-2001). All cell lines were purchased from ATCC: NCI-H441 lung adenocarcinoma (Cat# ATCC-CRM-HTB-174), HCC827 lung adenocarcinoma (Cat# CRL-2868), SW620 colorectal adenocarcinoma (Cat# CCL-227), HeLa cervical adenocarcinoma (Cat# CCL-2), MCF7 breast adenocarcinoma (Cat# HTB-22). Reagents used for transfection, RNA and protein related assays purchased from different companies are listed: JetPrime DNA Transfection kit (Polyplus Transfection, France), Trizol Reagent (Invitrogen), RNA Clean & Concentration-5 kit (Zymo Research, Cat# R1015). SuperScript III First-strand Synthesis System (Invitrogen-Life Technologies, CA). DreamTaq DNA polymerase (Fisher Scientific, Cat# FEREP0702), Zymo DNA-Clean and Concentration-5 kit (Zymo, Cat# D4003), proteinase inhibitor cocktail Set VII (EMB, Cat# 539138-1ML), Turbo DNase (Life Tech., Cat# AM2239), RNase A (Thermo Fisher, Cat# FEREN0531), BCA assay (BioSciences, Cat# 786-570), 4-20% gradient 10-well MiniProtean gel (Bio-Rad, Cat# 4561094). Trans-Blot Turbo Transfer unit (Bio-Rad, Cat# 1704150), Intercept (TBS) Protein-Free Blocking buffer (IBB) (Licor, Cat# LIC-927-80003). Antibodies were purchased from Proteintech and Santa Cruz Biotech: rabbit anti-KRas (Proteintech, Cat# 12063-1-AP), mouse anti-beta-Actin (Proteintech; Cat# 66009-1-1g), mouse monoclonal Gapdh antibody (Proteintech, Cat# 60004-1-IG), mouse monoclonal Pcsk9 antibody (Santa Cruz Biotech, Cat#: sc-515082), Rabbit polyclonal Gata3 antibody (Proteintech, Cat# 10417-1-AP). Secondary antibodies were ordered from Licor: Licor IRDye® 800CW Anti-Rabbit IgG Goat Secondary Antibody (Licor, Cat# 926-32211), Licor IRDye® 680RD Anti-Mouse IgG Goat Polyclonal Goat Secondary Antibody (Licor, Cat# 926-68070).

DNAzyme synthesis. All DNAzymes were prepared by solid-phase oligonucleotide synthesis using an automated Dr. Oligo DNA synthesizer on a 1 μmol scale universal CPG column (Glen Research) with optimized coupling times for modified phosphoramidites. Oligonucleotides were removed from the column and deprotected by incubation in ammonia gas for 2 h at 80°C (60 psi), and purified on a Glen-Pak™ DNA Purification Cartridge (Glen Research) followed by ion-pair reversed-phase HPLC as previously described (34). The samples were lyophilized to dryness, resuspended in water, and UV quantified. The synthesized DNAzymes were sodium salt exchanged prior to use in cells and verified by MALDI-TOF mass spectroscopy.

Cleavage product analysis. To generate an RNA ladder, 1 μM of Cy5-labeled 60-nt RNA was digested by 1 U of RNase T1 (1000 U/μL) in 50 mM Tris (pH 7.5), 10 mM NaCl, and 140 mM KCl at room temperature for 1 min. For DNAzyme-catalyzed reactions, 250 nM Dz and 250 nM Cy5-labeled 60-nt RNA (1S:1E) were incubated in the same buffer used for RNase T1 digestion but with the addition of 1 mM $MgCl_2$. For both reactions, a 1.5 μL aliquot of the reaction mixture was removed and quenched in 16.5 μL formamide buffer (99% deionized formamide, 25 mM EDTA). Quenched samples were denatured at 95°C for 10 min and resolved using 15% denaturing PAGE. Gels were imaged using an Odyssey CLx imaging system (LI-COR) and quantified using Image Studio Lite (LI-COR).

TNA walk of the catalytic domain. DNAzyme variants were evaluated for activity under multiple turnover conditions with 10 nM Dz and 1000 nM 16-nt RNA substrate (100S:1E) in simulated physiological reaction buffer comprised of 50 mM Tris-HCl (pH 7.5), 10 mM NaCl, 140 mM KCl, and 1 mM $MgCl_2$. Dzs and substrates were annealed in reaction buffer without

$MgCl_2$ by heating for 5 min at 95°C and then cooling for 5 min at 4°C. Reactions were equilibrated to 37°C for 2 min before initiating the reaction with the addition of $MgCl_2$. After heating at 37°C for 30 min, a 1.5 µL aliquot of the reaction mixture was removed and quenched in 16.5 µL formamide stop buffer (99% deionized formamide, 25 mM EDTA). Quenched samples were denatured at 95°C for 10 min and resolved using 20% denaturing PAGE. Gels were imaged using an Odyssey CLx imaging system (LI-COR) and quantified using Image Studio Lite (LI-COR).

Kinetic assay. Dz46 variants were assayed under multiple turnover conditions with 50 nM Dz and 500 nM 60-nt RNA substrate (10S:1E and 100S:1E) in simulated physiological reaction buffer comprised of 50 mM Tris-HCl (pH 7.5), 10 mM NaCl, 140 mM KCl, and 1 mM $MgCl_2$. Reactions were equilibrated to 37°C for 2 min (no annealing step) before initiating the reaction with the addition of $MgCl_2$ and kept at 37°C throughout the time course. At designated times between 0 and 60 min, 1.5 µL aliquots of the reaction mixture were removed and quenched in 16.5 µL formamide stop buffer (99% deionized formamide, 25 mM EDTA). Quenched samples were treated and analyzed as described above.

Initial velocity (v_0) determination. Initial rates (v_0) were calculated by a linear fit of the first 10-15% RNA cleavage events observed in the kinetic assay using equation (1):

$$v_o = \frac{(Y_f - Y_o) \times [S_0]}{(t_f - t_0)} \quad (1)$$

where v_0 is the initial velocity ($nM*min^{-1}$), Y_f is the percentage of cleaved substrate at finite time t when the first 10-15% cleavage reached, Y_0 is the percentage of cleaved substrate at t_0, $[S]_0$ is the initial substrate concentration (nM) at t_0.

The percentage of cleaved substrate (y-axis) and reaction time (x-axis) in minutes (min) was fitted to the pseudo-first order association kinetics of a substrate and an enzyme equation (2) using Prism 9 (GraphPad, USA) to graph the kinetic curve:

$$Y = Y_0 + (Y_\infty - Y_0) \times (1 - e^{-k_{obs} \times t}) \quad (2)$$

where Y is the percentage of cleaved substrate at finite time t, Y_0 is the percentage of cleaved substrate at t_0, Y_∞ is the percentage of cleaved substrate at infinite time where the reaction is plateau, k_{obs} is the observed pseudo-first order (substrate/enzyme interaction) rate constant (min^{-1}).

RNase H1 analysis. To evaluate RNase H1 recognition of the Dz-substrate complexes, cleavage assays were performed in the presence and absence of RNase H1. Cleavage activity was evaluated using 250 nM of Dz or ASO mixed with the 60-nt RNA substrates in a 1:1 ratio: 125 nM WT KRAS with a 5'-Cy5 tag and 125 nM G12V KRAS with a 5'-Alexa Fluor 750 tag. Reactions were performed at 37°C in simulated physiological reaction buffer containing 50 mM Tris-HCl (pH 7.5), 10 mM NaCl, 140 mM KCl, and 1 mM $MgCl_2$, with or without 5 ng/μL human RNase H1. Aliquots (1.5 μL) were removed after 30 min, quenched, and resolved using 20% denaturing PAGE as described above.

Melting temperature (Tm) study. All melts were performed with 1:1 oligonucleotide stoichiometry (1 μM DNAzyme + 1 μM RNA substrate) in 1 M NaCl, 50 mM Tris-HCl, 1 mM $MgCl_2$ at pH 7.5. Prior to melting, the strands are annealed in an Eppendorf tube by heating to 95ºC for 5 minutes and cooling on ice. Melting curves were obtained in the reverse and forward melting directions in a quartz cuvette of 1-cm path length with a temperature gradient of 20º to 90ºC and a ramping rate of 1°C per min by monitoring the change in UV absorbance at 260 nm across the temperature range using a Cary 100 UV-Vis spectrophotometer equipped with

a Peltier thermal controller. Tm values were determined by the hyperchromicity method using the Cary software package.

Cell lines and mammalian cell culture conditions. MCF7, HCC827, SW620 and NCI-H441 cells were cultured in RPMI 1640. HeLa was cultured in DMEM. Media were supplemented with 10% fetal bovine serum and 1% penicillin-streptomycin (1 mg/mL) and grown at 37°C, 5% CO_2.

Transfection. Cells were seeded in 6-cm (5 mL) culture dishes and allowed to grow for 24-48 hours until they reach 40-50% confluency. Cells were treated with 500 nM Dz using the JetPrime DNA Transfection Kit according to manufacturer's instructions with the exception that 40 µL of JetPrime reagent and 250 µL of JetPrime buffer were used per transfection of a 5 mL culture. The 500 nM Dz treatment was administered as a double-dosing regimen with the first transfection of 250 nM Dz at 0 hours and a second transfection of 250 nM Dz at 6 hours for HeLa cells and 24 hours for NCI-H441, HCC827, SW620, and MCF7 cells. HeLa cells were harvested at 24 hours and NCI-H441, HCC827, SW620, and MCF7 cells were harvested at 48 hours.

Total RNA isolation and reverse transcription-polymerase chain reaction (RT-PCR). Total RNA isolation was performed on each cell pellet using 1 mL/pellet of Trizol Reagent according to the manufacturer's instructions. The extracted total RNA was re-suspended in 44 µL of water. Total RNA was then treated with Turbo DNAse (20 U/reaction) at 37°C for 30 min with shaking, followed by purification using the RNA Clean & Concentration-5 Kit according to manufacturer's recommended protocol. Total RNA was eluted from IC columns twice with 22 µL of water, resulting in a total volume of 44 µL. 200 to 1000 ng of DNA-free RNA was subjected to cDNA synthesis using the SuperScript III First-strand Synthesis System with

random hexamer primers in a 20-µL reaction according to the manufacturer's instructions. Template mRNA in the RNA:cDNA hybrid was removed by RNase H (2U/cDNA reaction) digestion, resulting in a final volume of 21 µL. cDNA was then diluted to a final concentration of 5 ng/µL based on the starting amount of total RNA used in the cDNA synthesis and taken forward to PCR. Per 25-µL PCR reaction, 5 to 10 µL of 5 ng/µL cDNA was used. PCR thermal parameters used: 1x (94°C-2min), 40x (94°C-20sec, 57°C-15sec, 70°C-10sec), 1x (70°C-5min) for HCC827, HeLa, and MCF7 cells; SW620 cells used 18x amplification. Refer to Supplementary Table 8 for primers used in this assay.

Restriction fragment length polymorphism assay (PCR-RFLPA). PCR-RFLPA was used to differentiate WT and G12V KRAS alleles as previously described (25,35,36). In brief, cDNA was amplified by PCR using a unique sense primer that carries a single substitution (G to C) at the first nucleotide position (bold) of KRAS codon 11 (**G**CT to **C**CT). This substitution introduces *BstN*I recognition site ("CCWGG"), which spans from KRAS codon 11 (**C**CT) to codon 12 (GGT), in WT KRAS but not the G12V allele. Treatment of the amplicons with *BstN*I endonuclease shortens the WT allele by 50 nts relative to the G12V allele, making the two alleles distinguishable by 3% agarose gel electrophoresis. Refer to Supplementary Table 9 for primers used in this assay.

Total protein isolation and immunoblot analysis. At 24 and 48 hours post-transfection, cells were scraped from the plates and spun down at 1000 x g for 5 min at room temperature. Cell pellets subjected to protein isolation were re-suspended with 50-150 µL (10x volume of dried cell pellet) of RIPA lysis buffer (50 mM Tris-HCl at pH 7.5, 150 mM NaCl, 0.1% Triton, 0.5% Na-deoxycholate & 0.1% SDS, 5 mM EDTA). 8 µL of Protease Inhibitor Cocktail Set VII, 4 µL of Turbo DNase, 4 µL of RNase A were supplemented per 1 mL of RIPA Lysis buffer. Re-

suspended cells were incubated on ice for 0.5 h, subjected to three freeze-thaw cycles to lyse cells, and centrifuged at 15,000 rpm for 20 min at 4°C to collect the supernatant containing total protein. Total protein lysate was subjected to a BCA assay at 37°C for 30 min and quantified using the NanoDrop BCA application to determine protein concentration. 15-30 μg of total protein was resolved in a 4-20% gradient 10-well MiniProtean gel. The resolved proteins were transferred to a nitrocellulose membrane using a Trans-Blot Turbo Transfer unit. The membrane was allowed to air-dry for 0.5 h and blocked with Intercept Protein-Free Blocking Buffer (IBB) for 1 hour at RT. The membrane was probed overnight at 4°C with fresh IBB supplemented with 0.2% Tween-20 (IBBT) + rabbit anti-Kras at 1:2000 dilution or mouse anti-β-actin (loading control) at 1:10000 dilution, and then an additional 1 hour at RT on the following day. For Pcsk9, mouse monoclonal antibody (1:500 dilution) was used. For Gata3, rabbit polyclonal antibody (1:1000 dilution) was used. Mouse monoclonal Gapdh antibody (1:10000 dilution) was used for the loading control for Pcsk9 and Gata3 blots. Blots were washed 3x10 min/each with 1xTBST (150 mM NaCl, 50 mM Tris-HCl, pH 7.6 + 0.1%Tween-20) at RT, and subsequently incubated in 0.02% SDS supplemented-IBBT + Licor IRDye® 800CW Anti-Rabbit IgG Goat Secondary Antibody or Licor IRDye® 680RD Anti-Mouse IgG Goat Polyclonal Goat Secondary Antibody at 1:20000 dilution at RT for 1 h. Finally, blots were washed 3x10 min/each with 1xTBST at RT. Blots were imaged using an Odyssey CLx imaging system (LI-COR) and quantified using Image Studio Lite (LI-COR).

2.4 Results

We set out to optimize Dz46 through an iterative chemical evolution strategy involving rational design, synthesis, and testing of chemically modified variants (25). Our goal was to identify positions within the DNAzyme where substitutions with XNAs, specifically TNA,

could enhance catalytic activity and evade RNase H1 recognition. TNA, an RNA analog with a four-carbon threose sugar replacing the five-carbon ribose sugar found in RNA, was selected for its nuclease resistance and ability to hybridize with DNA and RNA (37,38). Since TNA amidites and oligonucleotides are not widely available from commercial sources, the TNA-modified Dz46 variants were prepared by solid-phase oligonucleotide synthesis (Supplementary Tables 1-6) using chemically synthesized TNA phosphoramidites and the resulting oligonucleotides were purified by ion-pair reversed-phase high performance liquid chromatography (HPLC) (33,34). Natural DNA and RNA oligonucleotides were obtained from commercial sources (Supplementary Tables 7-9).

To ensure physiological relevance, all DNAzyme activity assays were performed under multiple turnover conditions in buffer mimicking the ionic strength of the intracellular environment [1 mM $MgCl_2$, 140 mM KCl, 10 mM NaCl, and 50 mM Tris-HCl (pH 7.5)] at 37°C. The functional impact of each chemical perturbation toward DNAzyme activity was analyzed by denaturing polyacrylamide gel electrophoresis (PAGE), and initial velocities (v_0) of the final constructs selected for analysis were determined using a 60-nucleotide (nt) RNA substrate at a 100:1 substrate-to-enzyme ratio (S:E). The DNAzyme cut site of the 60-nt substrate was confirmed by an RNA ladder generated by RNase T1, an endonuclease that cleaves single-stranded RNA after guanosine residues, producing a series of truncations, including the expected 30-nt product (Supplementary Figure 1).

Catalytic Core Optimization

We first performed a TNA walk of the catalytic loop (positions 1-15 and flanking sites 0 and 16) to assess the tolerance of each position to chemical perturbation (Figure 2.1a). Although this region of the sequence had previously undergone extensive optimization, its

compatibility with TNA remained unexplored (25). We generated 17 TNA-substituted Dz46 variants, each retaining the complete set of Dz46 modifications, including LNA and OMe in the binding arms, and 2′-*O*-methoxyethoxy ribonucleic acid (MOE), OMe, and phosphorothioate (PS) in the catalytic loop (Figure 2.1a). The catalytic activity of each variant was initially evaluated using a short size-matched 16-nt RNA substrate under 100:1 (S:E) multiple turnover conditions (Supplementary Figure 2). The resulting cleavage profile reveals that substitutions made to positions 3, 8, and 9 enhance catalytic activity, while positions 0, 2, 4, 6, and 10 were intolerant to the TNA modification (Supplementary Figure 2). The tolerance of position 8 toward substitution with sugar-modified analogs (25-28) aligns with its placement near metal-ion binding site II, as reported previously for the NMR structure of 10-23 (39). However, the tolerance of TNA substitution at positions 3 and 9 were thought to be more interesting, as these residues, to the best of our knowledge, were not identified previously as permissive sites of chemical modification, making them novel sites for chemical optimization.

To examine the robustness of the substitutions, the TNA walk was repeated using a 60-nt RNA substrate under 10:1 and 100:1 (S:E) multiple turnover conditions (Figure 2.1b-c, Supplementary Figure 2). Several observations were made by comparing the results from the assays performed using different substrate lengths and concentrations. First, DNAzyme activity observed on the 60-nt substrate mirrors the activity observed for the 16-nt substrate. Second, DNAzyme activity is reduced under the more challenging conditions of increased substrate concentration. Third, the difference in activity between variants with TNA substitutions at positions 3 and 9 becomes more evident under the stringent conditions (Figure 2.1b-c), emphasizing the enhanced activity of the variant with TNA at position 3. This

last observation is consistent with a noticeably slower bursting profile for the variant with TNA at position 9 as compared to the variant with TNA at position 3 (Supplementary Figure 3). In a 60-min time course under 100:1 (S:E) conditions on the 60-nt substrate, the variant with TNA at position 3 reaches 50% RNA cleavage at ~30 min and maintains an enhanced

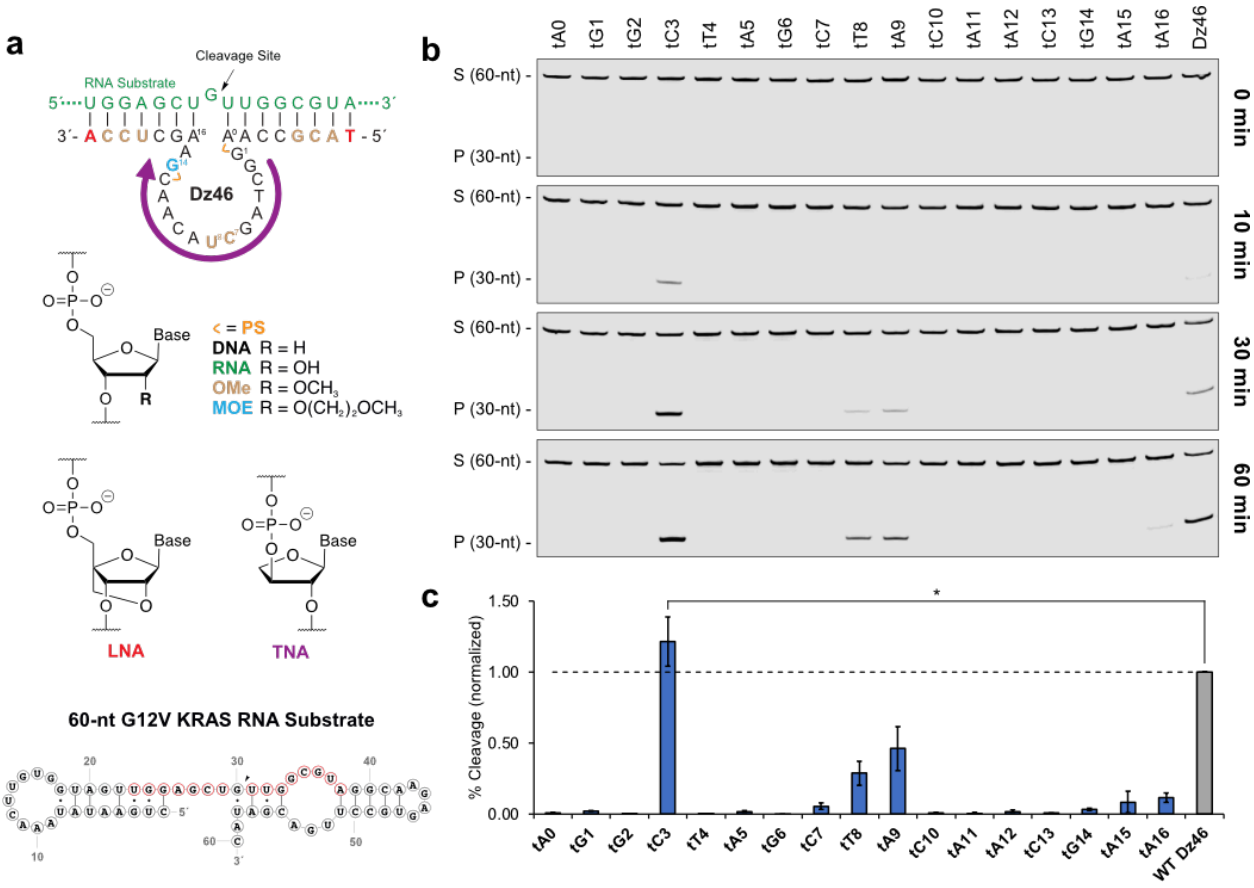

Figure 2.1. Optimizing the catalytic core of Dz46 with TNA. a) *Cartoon representation showing a TNA walk of the catalytic core of Dz46, chemical structures of modified nucleotides found in Dz46 analogs, and a 60-nt KRAS G12V RNA substrate depicting the region recognized by Dz46 in red used for kinetics.* ***b)*** *Representative denaturing PAGE gels showing 100:1 (S:E) multiple turnover RNA cleavage activity of a 60-nt substrate over the course of 60 min.* ***c)*** *Bar graph corresponding to (b) showing RNA cleavage activity normalized to that of Dz46 at 30 min. Data presented as the mean ± standard deviation (n=3 for all constructs except for Dz46 and tC3, n=6 for Dz46 and tC3). Two-tailed p-value determined by Welch's t-test (*, p<0.05). All reactions were performed under simulated physiological conditions in a buffer containing 1 mM $MgCl_2$, 50 mM Tris (pH 7.5), 10 mM NaCl, and 140 mM KCl at 37°C. Abbreviations: DNA (2'-deoxyribonucleic acid), RNA (ribonucleic acid), OMe (2'-deoxy-2'-methoxyribonucleic acid), MOE (2'-deoxy-2'-methoxyethoxyribonucleic acid), LNA (locked nucleic acid), TNA (threose nucleic acid), and PS (phosphorothioate). S: 5′-Cy5-labeled full-length substrate, P: 5′-Cy5-labeled cleavage product.*

catalytic activity relative to that of our previously described Dz46 variant (Figure 2.1b-c) (25).

Binding Arm Optimization

Next, we investigated whether TNA substitutions in the binding arms could reduce RNase H1 recognition without compromising catalytic function. Previous studies have implicated RNase H1 as the primary driver of targeted RNA cleavage in cultured mammalian cells treated with DNAzymes (9-11). In such cases, competition is thought to exist between the intrinsic activity of the DNAzyme and RNase H1, which recognizes complementary DNA-RNA duplexes as substrates for cleavage (40). Studies have shown that RNase H1 requires a minimum of 4 consecutive base pairs (bp) to trigger cleavage of the RNA (40-42), but it is noted that the DNA "gap" requirement may deviate by 1 to 2 additional bp due to the helical structure of the duplex with various positions and modifications considered (43). Dz46, even with its current modifications at the terminal positions of the binding arms, still meets the minimum 4 bp requirement and contains segments in the catalytic core region where off-target binding could, in theory, occur. Ultimately, however, the balance between the two mechanisms, DNAzyme- vs. RNase H-mediated strand cleavage, depends on the type and extent of chemical modifications found in the DNAzyme, with unmodified sequences driven by RNase H1 (9-11) and modified sequences favoring a DNAzyme-mediated cleavage mechanism (25).

One model for evaluating RNase H1 recognition of the DNAzyme-RNA complex involves a two-color analysis of allele-specific RNA cleavage (25). In this assay, synthetic RNA strands for wild-type and mutant substrates are separately prepared with 5'-modified Cy5 (red) and Alexa Fluor 750 (green) tags, respectively. In our case, we use an RNA sequence corresponding to KRAS G12V, a prominent mutation found in many human cancers (44).

Since DNAzymes can be programmed to exclusively cleave only one of the alleles, assays performed in the presence of both allelic substrates should exclusively yield a cleavage product for the on-target KRAS G12V strand. However, because the DNAzyme binds, but does not cleave, the off-target wild-type strand, assays performed in the presence of RNase H1 can yield one or more alternative length products due to RNase H1-mediated cleavage of the off-target strand. Although RNase H1-mediated cleavage of the on-target strand is possible, this reaction is rarely observed as the DNAzyme can kinetically outcompete RNase H1 for the correct allelic target. For example, Dz46 has been shown to yield a longer-length product due to unwanted RNase H1-mediated cleavage of the wild-type KRAS strand with no interference of the KRAS G12V strand (25). One minor caveat of this assay is that Alexa Fluor 750 is prone to signal bleed from the 800 nm (green) channel to the 700 nm (red) channel in the infrared Odyssey CLx imaging system, which can be excluded from analysis by separately evaluating each substrate (Supplementary Figure 4).

The two-color RNase H1 assay was validated with standard controls that include inactive (IB) and non-binding (NB) versions of Dz46 as well as an ASO, which behave as expected. The inactive DNAzyme and ASO controls yield cleavage products only in the presence of RNase H1, while the non-binding DNAzyme shows no signs of RNA cleavage, regardless of whether RNase H1 is present or absent (Figure 2.2). For the IB control, preferential cleavage of the G12V substrate by RNase H1 was observed (Figure 2.2b-c). This is likely due to increased hybridization of the DNAzyme to the on-target G12V substrate versus the off-target wild-type substrate, which carries a 1 bp mismatch in the binding arm. Together, the controls provide evidence of an existing antisense mechanism that competes with the intrinsic catalytic activity of the DNAzyme.

In an effort to reduce RNase H1 recognition of the enzyme-substrate complex, we examined Dz46 and an analog of Dz46 (NS580) that contain and lack TNA in their binding arms (Figure 2.2a). In the absence of RNase H1, all four DNAzymes (Dz46, Dz46+, NS580, and NS580+) exclusively cleave the mutant substrate, demonstrating >99% specificity for the target allele (Figure 2.2). However, in the presence of RNase H1, Dz46 and NS580 treated samples yield the desired G12V cleavage product as well as a longer length RNase H1-mediated product caused by cleavage of the off-target wild-type allelic strand (Figure 2.2, Supplementary Figure 5). Strikingly, the RNase H1-mediate product is largely abrogated in the samples treated with Dz46+ and NS580+, which carry TNA in their binding arms. The reduced ability for RNase H1 to recognize DNAzymes carrying TNA modifications in their binding

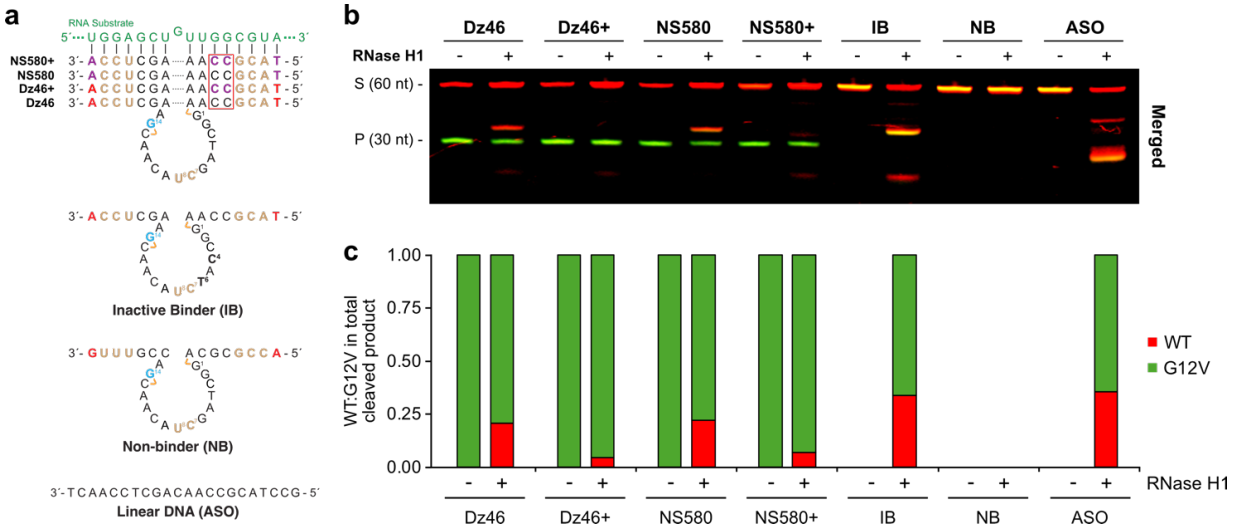

Figure 2.2. Optimizing the binding arms of Dz46 for reduced RNase H activity. a) *Variants of Dz46 carrying TNA in the binding arm, along with the non-binder (NB), inactive binder (IB), and ASO controls.* ***b)*** *Representative denaturing PAGE gel showing RNA cleavage profiles in reactions containing both the wild-type (red) and G12V (green) substrates (1:1) in the absence (–) or presence (+) of 5 ng/μL human RNase H1 after a 30 min incubation (n=2). Merged image of Cy5 (red) and AlexaFluor750 (green) channels are shown.* ***c)*** *Bar graph corresponding to (b) showing the fraction of G12V and WT cleavage in absence and presence of RNase H1. Reactions were performed under simulated physiological conditions in a buffer containing 1 mM $MgCl_2$, 50 mM Tris (pH 7.5), 10 mM NaCl, and 140 mM KCl at 37°C. S: 5′-labeled full-length substrate, P: 5′-labeled cleavage product. DNAzyme chemistry is color-matched to Figure 2.1.*

arms favors an autonomous DNAzyme-mediated cleavage mechanism that functions independent of any cellular protein machinery.

Combining Catalytic and Binding Arm Modifications

We next asked whether modifications identified in the catalytic loop and binding arms could be combined to establish a TNA-modified Dz46 variant that functioned with enhanced catalytic activity and RNase H1 evasion. We prepared a triply modified Dz46 variant, termed tC3+, containing TNA at position 3 of the catalytic loop as well as positions -2 and -3 of the 5' binding arm and compared the activity of this DNAzyme to its predecessors Dz46, tC3, and Dz46+ (Figure 2.3a). The tC3, Dz46+, and tC3+ variants all show improved initial rates over the parent Dz46, with the largest improvement in activity observed for DNAzymes carrying the TNA substitution at position 3 of the catalytic core. The tC3+ variant retained strong catalytic activity (v_0 = 24.9 ± 2.4 nM/min) comparable to that of tC3 (v_0 = 25.1 ± 1.4 nM/min), both of which were faster than Dz46 (v_0 = 15.7 ± 1.2 nM/min) and Dz46+ (v_0 = 19.1 ± 1.1 nM/min) (Figure 2.3b, Supplementary Figure 6). Interestingly, even though tC3+ and tC3 have similar burst profiles, tC3+ achieved more cleavage over time than tC3 (Figure 2.3b, Supplementary Figure 6). It is possible that the lower binding affinity (ΔTm = −2˚C) observed in Dz46 variants with TNA substitution in the binding arms resulted in better product release (Supplementary Figure 7), improving overall activity under multiple turnover conditions.

In allele-specific assays, tC3+ selectively cleaved the G12V substrate and showed no signs of RNase H1 recognition (Figure 2.3c-d, Supplementary Figure 8), unlike Dz46 and tC3, which produce RNase H1-mediated cleavage products of the wild-type strand. These results

establish tC3+ as a lead construct with both high catalytic activity and strong resistance to RNase H1.

Activity in Cultured Mammalian Cells

Recognizing the ability for tC3+ to resist RNase H1 recognition under cell-free conditions, we wished to confirm this activity in a cellular context. Homozygous SW620 (*G12V/G12V*) and HCC827 (*WT/WT*) cell lines exclusively expressing either the G12V or wild-type KRAS genes, respectively, offer a convenient way to test for RNase H1 activity. Since the DNAzymes used in this assay are engineered to recognize the G12V allele, any mRNA knockdown in the HCC827 cell line would be consistent with RNase H1 recognition, while mRNA knockdown in the SW620 cell line could be attributed to either DNAzyme cleavage or RNase H1 (Figure 2.4a). At 48 hours post-transfection, cells treated with Dz46, tC3, and tC3+ exhibit 27-51% knockdown of the KRAS G12V allele in SW620 cells (Figure 2.4b, Supplementary Figure 9). However, only tC3+ variant was able to evade RNase H1 recognition in the HCC827 cell line, corroborating our cell-free analysis (Figure 2.3).

As expected, NB-treated cells show no activity in either cell line, as this control has no sequence complementarity to the KRAS target. However, close analysis of the data does show an unusual pattern where the IB control appears to selectively knockdown KRAS transcript levels in the HCC827 cell line while showing no knockdown activity in the SW620 cell line (Figure 2.4b). We attribute this difference to different levels of RNase H1 in the two cell lines, which is consistent with prior work measuring RNase H1 levels across cell lines (25). Alternatively, it is also possible that the transfection efficiency of the HCC827 cell line is reproducibly higher than the SW620 cell line.

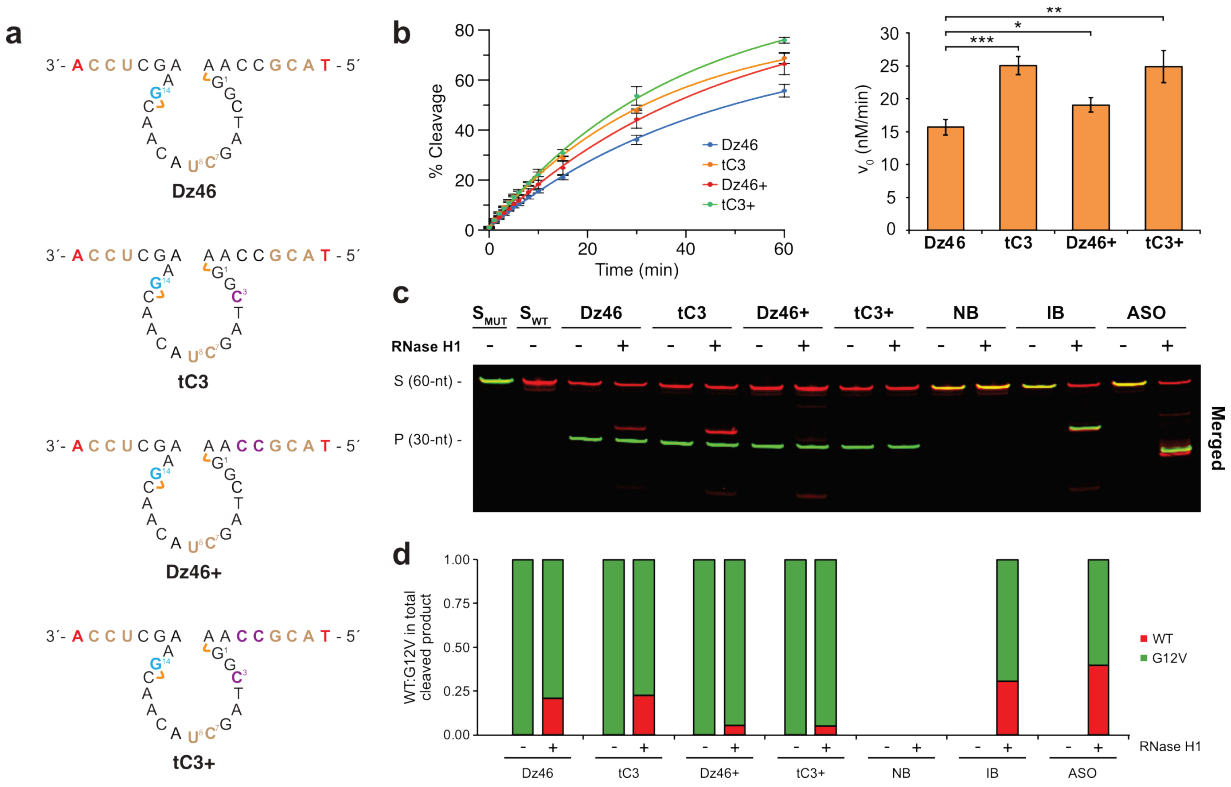

Figure 2.3. Engineering Dz46 variants with enhanced activity and RNase H1 resistance. a) *Engineered Dz46 variants carrying TNA at position dC3 of the catalytic loop (tC3), TNA at -2 and -3 positions of the 5' binding arm (Dz46+), TNA in both the catalytic loop and 5' binding arm (tC3+).* ***b)*** *Kinetic curves and initial velocity bar graphs showing RNA cleavage profiles of Dz46, tC3, Dz46+, and tC3+. Activity measured under 100:1 (S:E) multiple turnover conditions using a 60-nt RNA substrate with a time course of 0, 1, 2, 3, 4, 5, 6, 8, 10, 15 and 30 min. Data presented as the mean ± standard deviation (n=3). Two-tailed p-value determined by Welch's t-test (*, p<0.05; **, p<0.01; ***, p<0.001).* ***c)*** *Representative denaturing PAGE gel showing RNA cleavage profiles in reactions containing both the wild-type (red) and G12V (green) substrates (1:1) in the absence (–) or presence (+) of 5 ng/μL human RNase H1 after a 30 min incubation (n=2). Merged image of Cy5 (red) and AlexaFluor750 (green) channels are shown.* ***d)*** *Bar graph corresponding to (c) showing the fraction of G12V and WT cleavage in absence and presence of RNase H1. All reactions were performed under simulated physiological conditions in a buffer containing 1 mM $MgCl_2$, 50 mM Tris (pH 7.5), 10 mM NaCl, and 140 mM KCl at 37°C. S: 5′-Cy5-labeled full-length substrate, P: 5′-Cy5-labeled cleavage product. DNAzyme chemistry is color-matched to Figure 2.1.*

Next, we performed a restriction fragment length polymorphism (RFLP) analysis of DNAzyme activity in heterozygous KRAS (*G12V*/*WT*) H441 cells expressing both the WT and G12V alleles at a ratio of roughly 1:4 copies per cell, respectively (36). This assay uses RT-PCR to introduce a *Bst*NI restriction site into the wild-type allele, which is then selectively

cleaved upon incubation with *Bst*NI restriction endonuclease to yield two bands that are distinguishable by agarose gel analysis. Allele-specific knockdown is then assessed by quantifying the ratio of the G12V to WT band intensities within a treated sample. NB and IB controls show expected G12V:WT ratios that were observed in untreated samples of RFLP analysis (Figure 2.4c), where G12V levels are 2 to 3-fold higher than WT levels (25,35). All of the active DNzymes tested reduce G12V mRNA levels relative to the wild-type mRNA levels by ~3-fold (Figure 2.4c), confirming selective knockdown of the mutant allele. The apparent

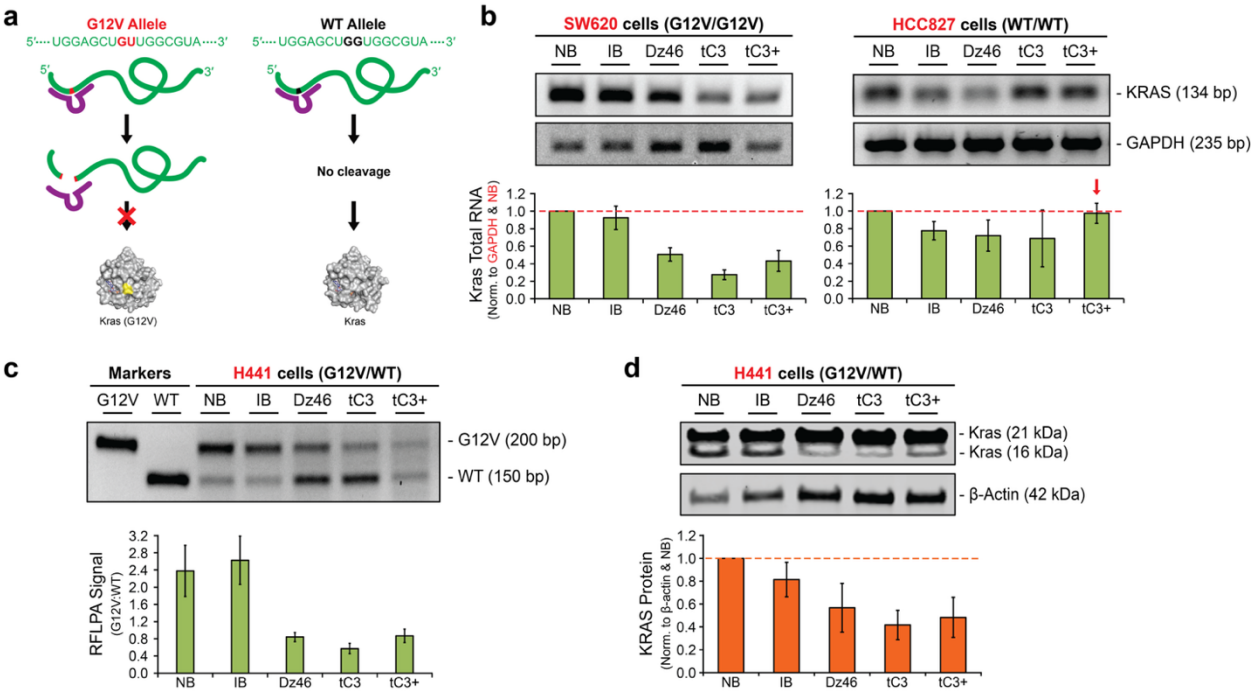

Figure 2.4. Allele specific knock-down of KRAS G12V in cells. a) *Cartoon representation of allele-specific RNA cleavage.* ***b)*** *Representative agarose gel and corresponding bar graph showing total KRAS levels after DNAzyme treatment of homozygous cell lines for KRAS G12V (SW620, n=3) and KRAS wild-type (HCC827, n=2). Red arrow signifies RNase H1 evasion.* ***c)*** *Representative agarose gel and corresponding bar graph showing allele-specific RNA cleavage of KRAS G12V in H441 cells treated with Dz46 variants. Samples were evaluated by restriction fragment length polymorphism (RFLP) analysis (n=3).* ***d)*** *Representative immunoblots and corresponding bar graph of total KRAS protein isolated from DNAzyme-treated H441 cells probed with anti-KRAS and b-Actin antibodies (n=4). Data presented as the mean ± standard deviation. All experiments were evaluated 48 hours post-transfection and normalized to the NB control.*

increase in WT levels observed in the agarose gel (Figure 2.4c) is due to changes in the ratio of WT-to-mutant levels in the DNAzyme-treated samples due to knockdown of the G12V allele.

Western blot analysis showed protein-level KRAS knockdown of 43% (Dz46), 58% (tC3), and 52% (tC3+) relative to a non-binding control. Since we were unable to find a satisfactory G12V-specific antibody, this assay was performed using an antibody that recognizes both isoforms of KRAS (16 and 21 kDa, Figure 2.4d). Interestingly, cells treated with the IB control show ~20% reduction in total KRAS protein with no concomitant change in KRAS mRNA level (Figure 2.4d). In the absence of any observable mRNA knockdown, we attribute this result to a steric block mechanism during protein translation, where binding of the IB control to the mRNA transcript partially inhibits protein translation. Since very few DNAzyme studies evaluate protein knockdown levels in cells, insufficient data is available to comment on how frequently IB controls act as a steric block during protein translation.

General Knockdown of other Therapeutic Targets

To assess the broader potential of the tC3+ DNAzyme, we extended our analysis to two clinically relevant gene targets: proprotein convertase subtilisin/kexin type 9 (PCSK9) and GATA binding protein 3 (GATA3). These targets were selected for their clinical relevance to hypercholesterolemia and inflammatory diseases, respectively, thereby providing a test of DNAzyme versatility and effectiveness across diverse cellular contexts using a general knockdown (non-allelic) approach (45,46).

PCSK9 is a liver-secreted protease that plays a central role in cholesterol homeostasis by promoting the degradation of low-density lipoprotein receptors (LDLR) on hepatocyte surfaces (47). Inhibition of PCSK9 increases LDLR availability, leading to enhanced clearance

of circulating LDL cholesterol, a mechanism that underpins the success of PCSK9-targeted monoclonal antibody therapies (48). However, with the FDA approval of inclisiran (49), a first-in-class siRNA drug to lower cholesterol by targeting PCSK9, it has been demonstrated that oligonucleotide-based approaches may offer a more cost-effective and tissue-targetable alternative (16). We designed constructs targeting a GU dinucleotide junction in exon 13 of PCSK9 mRNA (nucleotides 2710–2711), a canonical cleavage site for the 10-23 catalytic motif. Using HeLa cells as a model system, we measured mRNA levels by RT-PCR 24 hours post-transfection (Figure 2.5a–b, Supplementary Figure 9). All three active DNA-zymes, Dz46, tC3, and tC3+, exhibited robust mRNA knockdown, reducing PCSK9 transcript levels by 74%, 86%, and 99%, respectively, relative to the non-binding control. Immunoblot analysis confirmed the functional outcome of this knockdown, with mature PCSK9 protein levels decreasing by 30–40%, with the greatest effect observed for tC3+ (Figure 2.5c). This result demonstrates that tC3 is capable of high-efficiency gene silencing at both the RNA and protein levels for targets beyond KRAS.

GATA3, a zinc finger transcription factor, is a master regulator of Th2 cell differentiation and immune activation, and is also implicated in the pathogenesis of several diseases including asthma (50), breast cancer (51), and certain leukemias (52). Elevated GATA3 expression has been observed in the airway epithelium of patients with severe asthma, where it contributes to chronic inflammation and cytokine dysregulation (53). GATA3 is also highly expressed in luminal breast cancer, where it exists as both a full-length 50 kDa protein and a truncated 37 kDa isoform resulting from a frameshift mutation (54); the latter displays increased stability due to its prolonged half-life (>8 hours) (55). To explore whether our DNAzymes could knock down GATA3, we designed constructs targeting a GU junction in

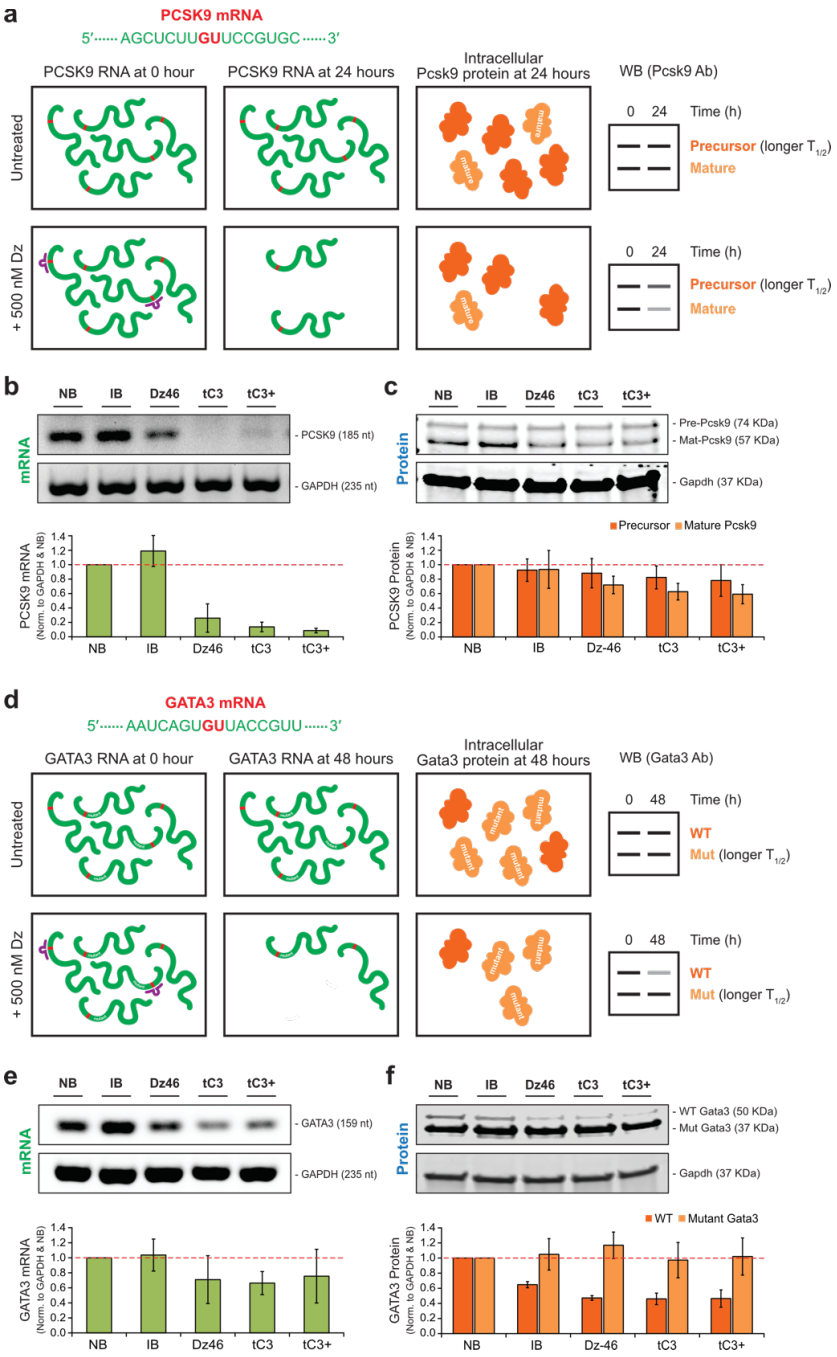

Figure 2.5. DNAzyme-mediated knockdown of PCSK9 and GATA3. a) *Cartoon representation of PCSK9 mRNA targeting and Pcsk9 protein knockdown.* ***b)*** *Representative agarose gel and corresponding bar graph of PCSK9 mRNA knockdown observed in HeLa cells.* ***c)*** *Representative immunoblots and corresponding bar graph of PCSK9 protein knockdown observed in HeLa cells.* ***d)*** *Cartoon representation of GATA3 mRNA targeting and Gata3 protein knockdown.* ***e)*** *Representative agarose gel and corresponding bar graph of GATA3 mRNA knockdown observed in MCF7 cells.* ***f)*** *Representative immunoblots and corresponding bar graph of GATA3 protein knockdown observed in MCF7 cells. Error bars denote ± standard deviation of the mean for 3 independent experiments. All data were normalized to the NB control. Abbreviations: NB, non-binder; IB, inactive binder; tC3, Dz46, DNAzyme 46; Dz46 with tC3 modification; tC3-Int, Dz46 with tC3 and TNA in the 5′ binding arm.*

exon 6 of the GATA3 transcript (nucleotides 2490–2491), and transfected MCF7 breast cancer cells with Dz46, tC3, and tC3+ variants (Figure 2.5d, Supplementary Figure 9).

At the mRNA level, GATA3 knockdown was modest but consistent, with reductions of 29% (Dz46), 36% (tC3), and 24% (tC3+) compared to the non-binding control (Figure 2.5e). Notably, these reductions were more pronounced at the protein level, wherein the full-length GATA3 protein was diminished by ~55% across all active variants (Figure 2.5f). The truncated isoform was not reduced, potentially due to its long half-life (55). Interestingly, even the IB control showed a 35% reduction in GATA3 protein levels, suggesting that IB control could once again be acting as a steric block during protein translation.

2.5 Discussion

We demonstrate that the incorporation of TNA into Dz46 facilitates enhanced catalytic activity and strong RNase H1 evasion. This advance addresses two important limitations of RNA-cleaving DNAzymes: (i) modest activity under physiological conditions and (ii) unintended activation of cellular RNase H1, thereby establishing a new framework for engineering autonomous gene silencing agents based on XNA chemistry.

The systematic TNA walk across the catalytic core revealed unexpected hotspots of tolerance, particularly at positions C3 and A9, which were not known previously as permissive sites for chemical modification in the 10-23 DNAzyme framework. The improved activity observed with TNA substitution at dC3 suggests a beneficial alteration in the local structural environment of the DNAzyme, possibly enhancing metal ion coordination or stabilizing the catalytic geometry. Importantly, the increased activity of the tC3 variant was preserved in longer RNA substrates and in cellular knockdown assays, validating its functional rele-

vance beyond cell-free models. These findings expand the repertoire of chemical modifications compatible with the 10–23 motif and open new avenues for enhancing DNAzyme performance through nucleic acid engineering (17).

Equally notable is the strategic placement of adjacent TNA residues in the 5' binding arm, which was sufficient to significantly reduce RNase H1-mediated cleavage without sacrificing catalytic efficiency. This outcome contrasts with earlier attempts to reduce RNase H1 recognition through competitive models that enhance catalytic turnover (25). Our data confirm that RNase H1 cleavage of the wild-type KRAS allele can be abrogated through precise modification of the binding arm, enabling true allele-specific discrimination against the G12V oncogenic variant. This effect was maintained in cellular assays, where tC3+ achieved selective KRAS knockdown in heterozygous and homozygous mutant cell lines, with essentially no activity against the wild-type allele.

The generalizability of the tC3+ architecture was tested against two additional therapeutic targets, PCSK9 and GATA3, which differ significantly in their expression, biological role, and molecular complexity. The marked knockdown of PCSK9 at both the RNA and protein levels positions tC3+ as a candidate for hepatic gene silencing applications, particularly in the context of cholesterol-lowering therapies. For GATA3, while mRNA knockdown was more moderate, protein-level reductions were substantial, particularly for the full-length isoform. This disconnect between RNA and protein knockdown levels highlights the nuanced relationship between protein target stability, transcript accessibility, and DNAzyme activity in different cellular environments, and underscores the importance of protein-level validation in functional studies.

A consistent theme across all experimental systems is the superior performance of the tC3+ variant within the set of DNAzymes tested. By integrating catalytic enhancement and RNase H1 evasion into a single construct, this variant overcomes limitations typically encountered when modifications are applied in isolation, for example using structure-based approaches. These results affirm the utility of combining iterative design methods with nucleic acid chemistry to develop next-generation DNAzymes with improved pharmacodynamic properties. The demonstration of efficacy across three clinically relevant targets using allele-specific and general knockdown activity further supports the therapeutic potential of this strategy.

In summary, our findings establish TNA as a powerful tool for engineering DNAzymes with enhanced intracellular activity and allele-specific precision. The modular design of tC3+ supports its adaptation to a broad range of gene targets, paving the way for future studies focused on pharmacokinetics, biodistribution, and in vivo efficacy. More broadly, our work highlights the value of XNA chemistry in advancing oligonucleotide therapeutics and suggests that further exploration of non-canonical sugar backbones may yield additional gains in therapeutic utility.

2.6 Data Availability

All data are available upon reasonable request.

2.7 Funding

This work was supported by a sponsored research project from 1E Therapeutics.

2.8 Conflict of Interest

The authors and the University of California-Irvine have filed a patent application on the DNAzyme chemistry. JC is a consultant for 1E Therapeutics.

2.9 Acknowledgements

We wish to thank members of the Chaput lab for their helpful comments on the manuscript.

2.10 Author Contributions

J.C. conceived the project. All authors designed the experiments. E.L., K.N., N.S., and T.M. performed the experiments. J.C. wrote the manuscript with input from all authors.

2.11 References

(1) Silverman, S.K. (2016) Catalytic DNA: Scope, Applications, and Biochemistry of Deoxyribozymes. *Trends Biochem. Sci .* **41**, 595-609.

(2) Yang, M., Xie, Y., Zhu, L., Li, X. and Xu, W. (2024) Functional nucleic acid enzymes: nucleic acid-based catalytic factories. *ACS Catalysis*, **14**, 16392-16422.

(3) Santoro, S.W. and Joyce, G.F. (1997) A general purpose RNA-cleaving DNA enzyme. *Proc. Natl. Acad. Sci. U.S.A.*, **94**, 4262-4266.

(4) Santoro, S.W. and Joyce, G.F. (1998) Mechanism and utility of an RNA-cleaving DNA enzyme. *Biochemistry*, **37**, 13330-13342.

(5) Joyce, G.F. (2001) RNA cleavage by the 10-23 DNA enzyme. *Methods Enzymol.*, **341**, 503-517.

(6) Fokina, A.A., Stetsenko, D.A. and Francois, J.C. (2015) DNA enzymes as potential therapeutics: towards clinical application of 10-23 DNAzymes. *Expert Opin. Biol. Ther.*, **15**, 689-711.

(7) Malik, T.N. and Chaput, J.C. (2021) XNA enzymes by evolution and design. *Current Research in Chemical Biology*, **1**, 100012.

(8) Victor, J., Steger, G. and Riesner, D. (2018) Inability of DNAzymes to cleave RNA in vivo is due to limited Mg2+ concentration in cells. *Eur Biophys J*, **47**, 333-343.

(9) Young, D.D., Lively, M.O. and Deiters, A. (2010) Activation and deactivation of DNAzyme and antisense function with light for the photochemical regulation of gene expression in mammalian cells. *J. Am. Chem. Soc.*, **132**, 6183-6193.

(10) Wang, F., Saran, R. and Liu, J. (2015) Tandem DNAzymes for mRNA cleavage: choice of enzyme, metal ions and the antisense effect. *Bioorg. Med. Chem. Lett.*, **25**, 1460-1463.

(11) Hollenstein, M. (2015) DNA Catalysis: The Chemical Repertoire of DNAzymes. *Molecules*, **20**, 20777-20804.

(12) Rees, H.A. and Liu, D.R. (2018) Base editing: precision chemistry on the genome and transcriptome of living cells. *Nat. Rev. Genet.*, **19**, 770-788.

(13) Helm, J., Schols, L. and Hauser, S. (2022) Towards Personalized Allele-Specific Antisense Oligonucleotide Therapies for Toxic Gain-of-Function Neurodegenerative Diseases. *Pharmaceutics*, **14**, 1708.

(14) Yamada, K., Hildebrand, S., Davis, S.M., Miller, R., Conroy, F., Sapp, E., Caiazzi, J., Alterman, J.F., Roux, L., Echeverria, D. *et al.* (2021) Structurally constrained phosphonate internucleotide linkage impacts oligonucleotide-enzyme interaction, and modulates siRNA activity and allele specificity. *Nucleic Acids Res.*, **49**, 12069-12088.

(15) Conroy, F., Miller, R., Alterman, J.F., Hassler, M.R., Echeverria, D., Godinho, B., Knox, E.G., Sapp, E., Sousa, J., Yamada, K. *et al.* (2022) Chemical engineering of therapeutic siRNAs for allele-specific gene silencing in Huntington's disease models. *Nat. Commun.*, **13**, 5802.

(16) Egli, M. and Manoharan, M. (2023) Chemistry, structure and function of approved oligonucleotide therapeutics. *Nucleic Acids Res.*, **51**, 2529-2573.

(17) Khvorova, A. and Watts, J.K. (2017) The chemical evolution of oligonucleotide therapies of clinical utility. *Nat. Biotechnol.*, **35**, 238-248.

(18) Chaput, J.C. and Herdewijn, P. (2019) What Is XNA? *Angew. Chem. Int. Ed. Engl.*, **58**, 11570-11572.

(19) Chaput, J.C., Egli, M. and Herdewijn, P. (2025) The XNA Alphabet. *Nucleic Acids Res.*, **53**, gkaf635, https://doi.org/610.1093/nar/gkaf1635.

(20) Martin, P. (1995) A New Access to 2'-O-Alkylated Ribonucleosides and Properties of 2'-O-Alkylated Oligoribonucleotides. *Helv. Chim. Acta*, **78**, 486-504.

(21) Koshkin, A.A., Nielsen, P.E., Meldgaard, M., Rajwanshi, V.K., Singh, S.K. and Wengel, J. (1998) LNA (locked nucleic acid): an RNA mimic forming exceedingly stable LNA:LNA duplexes *J. Am. Chem. Soc.*, **120**, 13252-13253.

(22) Damha, M.J., Wilds, C.J., Noronha, A., Brukner, I., Borkow, G., Arion, D. and Parniak, M.A. (1998) Hybrids of RNA and arabinonucleic acids (ANA and 2'F-ANA) are substrates for Ribonuclease H. *J. Am. Chem. Soc.*, **120**, 12976-12977.

(23) Wang, Y., Nguyen, K., Spitale, R.C. and Chaput, J.C. (2021) A biologically stable DNAzyme that efficiently silences gene expression in cells. *Nat. Chem.*, **13**, 319-326.

(24) Chiba, K., Yamaguchi, T. and Obika, S. (2023) Development of 8-17 XNAzymes that are functional in cells. *Chem. Sci.*, **14**, 7620-7629.

(25) Nguyen, K., Malik, T.N. and Chaput, J.C. (2023) Chemical evolution of an autonomous DNAzyme with allele-specific gene silencing activity. *Nat. Commun.*, **14**, 2413.

(26) Schubert, S., Gul, D.C., Grunert, H.P., Zeichhardt, H., Erdmann, V.A. and Kurreck, J. (2003) RNA cleaving '10-23' DNAzymes with enhanced stability and activity. *Nucleic Acids Res.*, **31**, 5982-5992.

(27) Nawrot, B., Widera, K., Wojcik, M., Rebowska, B., Nowak, G. and Stec, W.J. (2007) Mapping of the functional phosphate groups in the catalytic core of deoxyribozyme 10-23. *FEBS J*, **274**, 1062-1072.

(28) Cozens, C., Mutschler, H., Nelson, G.M., Houlihan, G., Taylor, A.I. and Holliger, P. (2015) Enzymatic Synthesis of Nucleic Acids with Defined Regioisomeric 2'-5' Linkages. *Angew. Chem. Int. Ed. Engl.*, **54**, 15570-15573.

(29) Liu, Y., Zhang, S., Zhang, M., Liu, X., Wu, Y., Wu, Q., Chaput, J.C. and Wang, Y. (2025) Chemical evolution of ASO-like DNAzymes for effective and extended gene silencing in cells. *Nucleic Acids Res.*, **53**, gkaf144, https://doi.org/110.1093/nar/gkaf1144.

(30) Wang, Y., Ngor, A.K., Nikoomanzar, A. and Chaput, J.C. (2018) Evolution of a general RNA-cleaving FANA enzyme. *Nat. Commun.*, **9**, 5067.

(31) Wang, Y., Wang, Y., Song, D., Sun, X., Li, Z., Chen, J.Y. and Yu, H. (2022) An RNA-cleaving threose nucleic acid enzyme capable of single point mutation discrimination. *Nat. Chem.*, **14**, 350-359.

(32) Taylor, A.I., Pinheiro, V.B., Smola, M.J., Morgunov, A.S., Peak-Chew, S., Cozens, C., Weeks, K.M., Herdewijn, P. and Holliger, P. (2015) Catalysts from synthetic genetic polymers. *Nature*, **518**, 427-430.

(33) Sau, S.P., Fahmi, N.E., Liao, J.-Y., Bala, S. and Chaput, J.C. (2016) A scalable synthesis of α-L-threose nucleic acid monomers. *J. Org. Chem.*, **81**, 2302-2307.

(34) Lee, E.M., Setterholm, N.A., Hajjar, M., Barpuzary, B. and Chaput, J.C. (2023) Stability and mechanism of threose nucleic acid toward acid-mediated degradation. *Nucleic Acids Res.*, **51**, 9542-9551.

(35) Nguyen, K., Wang, Y.J., England, W.E., Chaput, J.C. and Spitale, R.C. (2021) Allele-Specific RNA Knockdown with a Biologically Stable and Catalytically Efficient XNAzyme. *J. Am. Chem. Soc.*, **143**, 4519-4523.

(36) Sunaga, N., Shames, D.S., Girard, L., Peyton, M., Larsen, J.E., Imai, H., Soh, J., Sato, M., Yanagitani, N., Kaira, K. *et al.* (2011) Knockdown of oncogenic KRAS in non-small cell lung cancers suppresses tumor growth and sensitizes tumor cells to targeted therapy. *Mol Cancer Ther*, **10**, 336-346.

(37) Schöning, K.U., Scholz, P., Guntha, S., Wu, X., Krishnamurthy, R. and Eschenmoser, A. (2000) Chemical etiology of nucleic acid structure: the a-threofuranosyl-(3'-->2') oligonucleotide system. *Science*, **290**, 1347-1351.

(38) Culbertson, M.C., Temburnikar, K.W., Sau, S.P., Liao, J.-Y., Bala, S. and Chaput, J.C. (2016) Evaluating TNA stability under simulated physiological conditions. *Bioorg. Med. Chem. Lett.*, **26**, 2418-2421.

(39) Borggrafe, J., Victor, J., Rosenbach, H., Viegas, A., Gertzen, C.G.W., Wuebben, C., Kovacs, H., Gopalswamy, M., Riesner, D., Steger, G. *et al.* (2022) Time-resolved structural analysis of an RNA-cleaving DNA catalyst. *Nature*, **601**, 144-149.

(40) Cerritelli, S.M. and Crouch, R.J. (2009) Ribonuclease H: the enzymes in eukaryotes. *FEBS J*, **276**, 1494-1505.

(41) Williams, J.S., Lujan, S.A. and Kunkel, T.A. (2016) Processing ribonucleotides incorporated during eukaryotic DNA replication. *Nat Rev Mol Cell Biol*, **17**, 350-363.

(42) Crossley, M.P., Brickner, J.R., Song, C., Zar, S.M.T., Maw, S.S., Chedin, F., Tsai, M.S. and Cimprich, K.A. (2021) Catalytically inactive, purified RNase H1: A specific and sensitive probe for RNA-DNA hybrid imaging. *J Cell Biol*, **220**, e202101092.

(43) Yazbeck, D.R., Min, K.L. and Damha, M.J. (2002) Molecular requirements for degradation of a modified sense RNA strand by Escherichia coli ribonuclease H1. *Nucleic Acids Res.*, **30**, 3015-3025.

(44) McCormick, F. (2015) KRAS as a Therapeutic Target. *Clin. Cancer Res.*, **21**, 1797-1801.

(45) Liu, C., Chen, J., Chen, H., Zhang, T., He, D., Luo, Q., Chi, J., Hong, Z., Liao, Y., Zhang, S. *et al.* (2022) PCSK9 Inhibition: From Current Advances to Evolving Future. *Cells*, **11**, 2972.

(46) Ray, A. and Cohn, L. (1999) Th2 cells and GATA-3 in asthma: new insights into the regulation of airway inflammation. *J Clin Invest*, **104**, 985-993.

(47) Lagace, T.A. (2014) PCSK9 and LDLR degradation: regulatory mechanisms in circulation and in cells. *Curr Opin Lipidol*, **25**, 387-393.

(48) Warden, B.A., Fazio, S. and Shapiro, M.D. (2020) The PCSK9 revolution: Current status, controversies, and future directions. *Trends Cardiovasc Med*, **30**, 179-185.

(49) Lamb, Y.N. (2021) Inclisiran: First Approval. *Drugs*, **81**, 389-395.

(50) Zhang, D.H., Yang, L., Cohn, L., Parkyn, L., Homer, R., Ray, P. and Ray, A. (1999) Inhibition of allergic inflammation in a murine model of asthma by expression of a dominant-negative mutant of GATA-3. *Immunity*, **11**, 473-482.

(51) Perou, C.M., Sorlie, T., Eisen, M.B., van de Rijn, M., Jeffrey, S.S., Rees, C.A., Pollack, J.R., Ross, D.T., Johnsen, H., Akslen, L.A. *et al.* (2000) Molecular portraits of human breast tumours. *Nature*, **406**, 747-752.

(52) Perez-Andreu, V., Roberts, K.G., Harvey, R.C., Yang, W., Cheng, C., Pei, D., Xu, H., Gastier-Foster, J., E, S., Lim, J.Y. *et al.* (2013) Inherited GATA3 variants are associated with Ph-like childhood acute lymphoblastic leukemia and risk of relapse. *Nat. Genet.*, **45**, 1494-1498.

(53) Krug, N., Hohlfeld, J.M., Kirsten, A.M., Kornmann, O., Beeh, K.M., Kappeler, D., Korn, S., Ignatenko, S., Timmer, W., Rogon, C. *et al.* (2015) Allergen-induced asthmatic responses modified by a GATA3-specific DNAzyme. *N. Engl. J. Med.*, **372**, 1987-1995.

(54) Usary, J., Llaca, V., Karaca, G., Presswala, S., Karaca, M., He, X., Langerod, A., Karesen, R., Oh, D.S., Dressler, L.G. *et al.* (2004) Mutation of GATA3 in human breast tumors. *Oncogene*, **23**, 7669-7678.

(55) Adomas, A.B., Grimm, S.A., Malone, C., Takaku, M., Sims, J.K. and Wade, P.A. (2014) Breast tumor specific mutation in GATA3 affects physiological mechanisms regulating transcription factor turnover. *BMC Cancer*, **14**, 278.

CHAPTER 3: Dynamism and Evolvability in Nucleic Acid Enzymes

Erica M. Lee[1] and John C. Chaput[1-4]*

Affiliations

[1]Department of Pharmaceutical Sciences, University of California, Irvine, CA 92697-3958, United States

[2]Department of Chemistry, University of California, Irvine, CA 92697-3958, United States

[3]Department of Molecular Biology and Biochemistry, University of California, Irvine, CA 92697-3958, United States

[4]Department of Chemical and Biomolecular Engineering, University of California, Irvine, CA 92697-3958, United States

Chapter 3 is an adaption of the material in press in Nature Communications 2026.

3.1 Abstract

Protein dynamism and evolvability are key parameters linking enzyme flexibility to adaptive potential, yet how these concepts apply to nucleic acid enzymes remains largely unexplored. Here, we propose that threose nucleic acid (TNA), a genetic polymer that is more conformationally restricted than DNA, may be evolutionarily constrained by its preorganized backbone. RNA-cleavage profiles comparing the well-known 10-23 DNA enzyme (DNAzyme) with two in vitro selected TNA enzymes (threozymes) reveal striking differences in their temperature dependence. While the DNAzyme catalyzed reaction is optimal at 37°C and weakly active at 50°C, threozymes display the opposite trend, suggesting that TNA catalysis must overcome a higher free-energy barrier than DNA catalysis. Consistent with this view, the reaction becomes less temperature dependent for threozymes that operate with more flexible active sites. Together, these findings highlight the importance of backbone structure as a critical parameter for evolvability with implications for RNA world models and biomedical applications.

3.2 Introduction

A defining feature of protein enzymes is their capacity to explore conformational landscapes. Rather than acting as rigid scaffolds, most enzymes populate ensembles of interconverting states that collectively shape their catalytic efficiency and evolutionary potential through active sites that position reactive groups to achieve a stable transition state[1]. Mutations can alter these ensembles by stabilizing alternative conformations that allow new enzyme functions to emerge from existing folds[2-4]. This coupling between conformational dynamics and function led to the view that enzyme evolution proceeds through conformational

landscapes where structural plasticity enables proteins to access new catalytic states, thereby making dynamism an important determinant of evolvability[5].

The rise of diverse classes of genetic polymers, so-called xeno-nucleic acids or XNAs, provides an opportunity to ask whether the principles linking dynamics and evolution in proteins also extend to nucleic acid enzymes[6,7]. Unlike proteins, whose folding behavior is largely driven by side chain packing in a hydrophobic core[8,9], nucleic acid structure is dictated by the composition and geometry of the sugar-phosphate backbone[10,11]. Even subtle chemical changes can profoundly alter the folding stability, helical geometry, and base pairing preferences of a genetic system[12]. As an example, deoxyxylo nucleic acid (dXyloNA), an epimer of DNA with inverted stereochemistry at the 3' hydroxy, forms a left-handed duplex with helical parameters that are distinct from either DNA or RNA[13]. Such observations suggest that backbone chemistry may strongly control the folding of a genetic system, enabling some polymers to access conformationally diverse and functionally productive landscapes while restricting others to narrower regions of structure-function space. From this perspective, nucleic acid backbones could represent a critical determinant of evolvability, dictating the extent to which sequences can be converted into folds and folds into functions.

Among the XNA systems capable of Darwinian evolution, 3',2'-a-L-threose nucleic acid (TNA, Fig. 3.1a) has received considerable attention from the origins community as a possible progenitor of RNA and from the synthetic biology community as an alternative genetic polymer with potential applications in biotechnology and medicine[14-18]. Despite having a shorter backbone based on a four-carbon threose sugar, TNA forms stable antiparallel Watson-Crick duplexes with itself as well as with complementary strands of DNA and RNA[19], and it can undergo Darwinian evolution using engineered polymerases[20]. These advances have

enabled the isolation of aptamers and catalysts from large, unbiased pools of random TNA sequences[21-25]. However, structural studies reveal that TNA is more conformationally restricted than DNA and RNA[26], raising the possibility that backbone geometry may influence the evolutionary landscape accessible to TNA enzymes.

Here, we examine how backbone chemistry shapes nucleic acid catalysis by comparing RNA cleavage activity mediated by the well-characterized 10-23 DNA enzyme (DNAzyme, Dz)[27] with that of two independently evolved TNA enzymes (threozymes, Tz) that act on the same substrate. Whereas the DNAzyme displays maximal activity near physiological temperature, the threozymes become increasingly active at elevated temperatures. These opposing temperature profiles suggest that TNA-mediated catalysis requires overcoming a larger free-energy barrier, consistent with a catalytic profile constrained by a more rigid backbone architecture. Notably, the temperature dependence narrows for TNA catalysts that operate with less defined active sites, indicating that increased structural flexibility alleviates this constraint. Together, these results show that backbone chemistry can shape the energetic landscape of nucleic acid catalysts and suggest that the architecture of a genetic polymer may place fundamental limits on its catalytic evolvability.

3.3 Results

Recognizing that TNA maintains a backbone repeat unit that is both shorter and more physically constrained than DNA and RNA (Fig. 3.1a)[19], we asked whether these properties might limit the ability of TNA to fold into structures with defined functional properties. We were particularly interested in how RNA-cleaving catalysts, one of the most accessible classes of nucleic acid enzymes[28-30], would compare when evolved in the context of a TNA backbone. Would in vitro selection produce a rich distribution of threozymes with varied catalytic

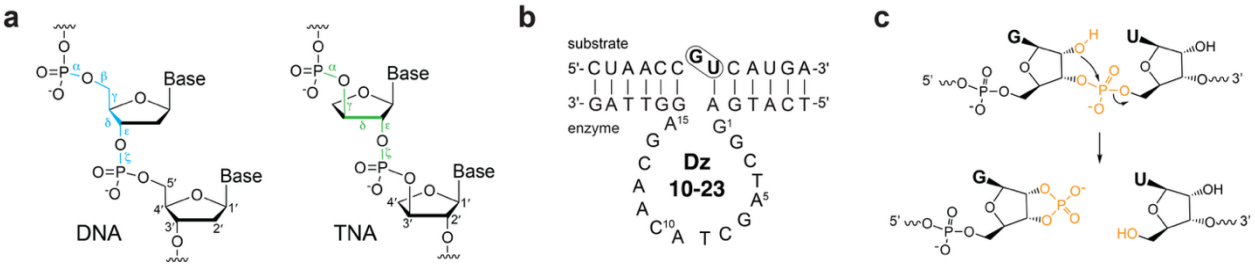

Figure 3.1. Nucleic acid catalysis. a, *Chemical structures, backbone torsion angles, and sugar atom numbering of DNA (blue) and TNA (green).* ***b,*** *Dz 10-23 in complex with an RNA substrate. The G-U cleavage site is shown in bold inside a circle.* ***c,*** *Mechanism of magnesium-dependent RNA cleavage.*

activities, as is commonly seen for DNA enzymes[31], or would the conformational preorganization of the TNA backbone compress the evolutionary landscape into a flatter horizon with only a limited set of functional solutions?

To address this question, we performed parallel in vitro selection experiments designed to isolate RNA-cleaving catalysts from pools of unbiased random-sequence TNA molecules. Guided by prior studies[32-34], we targeted a segment of the Kirsten rat sarcoma (KRAS) oncogene, one of the most frequently mutated drivers in human cancers[35]. The clinically relevant G12V variant, long considered difficult to target therapeutically[36], arises from a G→U mutation at position 2 of codon 12, producing a glycine to valine substitution in the translated protein sequence. This single-nucleotide difference creates a unique G-U junction in the mutant transcript that is absent from the wildtype sequence, enabling allele-specific targeting by RNA-cleaving DNAzymes[37].

Prior structural and biochemical studies have shown that the classic 10-23 DNAzyme cleaves such junctions via a general acid-base mechanism (Fig. 3.1b,c) whereby dG14 within the catalytic loop abstracts a proton from the O2' atom of the scissile rG residue, while a hydrated magnesium ion simultaneously donates a proton to the O5' atom of the adjacent U^{-1} residue[38,39]. The resulting O2' oxyanion then performs an in-line nucleophilic attack on the

adjacent phosphodiester bond, yielding an upstream fragment bearing a cyclic 2',3'-monophosphate and a downstream product with a 5' hydroxyl terminus. Whether TNA can be evolved to catalyze this reaction using a similarly constrained active site—one in which the substrate remains fully base-paired up to the exocyclic guanine at the G-U the cleavage site—remains unknown, raising the broader question of whether a conformationally restricted backbone can support the precise positioning and chemical cooperativity required for efficient phosphodiester cleavage.

The selection was performed using a DNA display strategy in which each TNA molecule was physically linked to its encoding double-stranded (ds) DNA template[40]. As illustrated in Figure 3.2, a 5'-phosphorylated DNA stem-loop structure was ligated onto the 3' end of two different chemically synthesized DNA libraries carrying random regions of either 15 or 20 consecutive nucleotides (nt) (Supplementary Table 1). The pools of self-priming

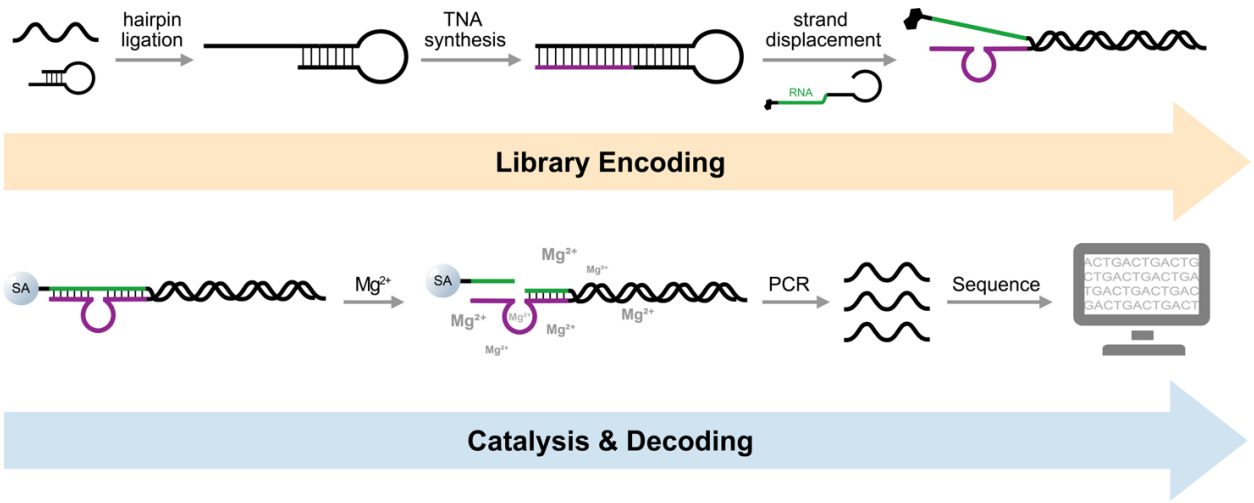

Figure 3.2. TNA libraries prepared and screened by DNA display. *A pool of single-stranded DNA (black) ligated to a self-priming stem-loop is extended with TNA (purple). Strand displacement initiated by a second primer extension reaction generates the genotype-phenotype linkage. The RNA substrate (green) is introduced via its conjugation to the strand displacement primer. The libraries are immobilized on streptavidin-coated (SA) magnetic beads and functional TNA molecules cleave themselves off the bead in the presence of magnesium ions. The recovered DNA is PCR amplified and used to generate another round of selection or sequenced.*

templates were then extended with chemically synthesized TNA triphosphates (tNTPs)[41,42] using the recently evolved 10-92 TNA polymerase[43]. The resulting TNA-DNA hairpin duplex was denatured in a strand displacement reaction using Bst DNA polymerase to extend a DNA primer annealed to the loop region of the hairpin with DNA (Supplementary Fig. 1). The product of this reaction were pools of single-stranded (ss) TNA molecules that had become physically linked to their encoding dsDNA. This design placed the TNA molecules across from the RNA substrate, introduced via the strand displacement primer.

Iterative cycles of in vitro selection and amplification were performed using libraries that oversampled the sequence space defined by 15- and 20 random nucleotide positions (N_{15} and N_{20}), corresponding to 60,200 and 60 copies per sequence, respectively. This library length was chosen to be consistent with Dz 10-23, which has a catalytic domain comprised of 15 unpaired nucleotides[27], and a slightly longer length to account for the reduced flexibility of TNA[26]. For each round of selection, the DNA display libraries were applied to a streptavidin-coated solid support and washed with selection buffer to remove the unbound molecules (Fig. 3.2). Functional TNA catalysts were then eluted by incubating the resin with selection buffer supplemented with 20 mM $MgCl_2$ at pH 7.5 and 37°C. Under these conditions, catalytically active sequences cleave a predefined G-U phosphodiester linkage in the RNA substrate (Fig. 3.1b), releasing the 3' cleavage product into the eluate. TNA sequences recovered from the eluate were isolated and amplified by the polymerase chain reaction (PCR) using DNA primers designed to recognize fixed sequences flanking the random region in the encoding DNA tag. The amplified DNA was made single stranded and used to generate new libraries of TNA molecules for subsequent rounds of selection.

As the selections progressed, the stringency was increased by progressively reducing both the incubation time and $MgCl_2$ concentration. The divalent metal ion cofactor was decreased from 20 to 0.5 mM $MgCl_2$, while the reaction time was shortened from 19 hours to 15 minutes. After 8 rounds of selection, DNA amplicons isolated from rounds 4, 6, and 8 of both selections were analyzed by next-generation sequencing (NGS) using an Illumina MiSeq platform. The six most enriched sequences from each selection (Supplementary Table 2) were synthesized in a 7+7 binding arm configuration by solid phase synthesis (SPS) using TNA phosphoramidites prepared by chemical synthesis[41]. The TNA sequences are largely unrelated to one another (Hamming distances: N15 members, 6-13; N20 members, 12-15), indicating that each molecule emerged as an independent solution to the problem of how TNA could catalyze the cleavage of an RNA substrate.

Each chemically synthesized threozyme was evaluated for its ability to cleave a 5' labelled RNA substrate under bimolecular, *in-trans* cleavage conditions, where the enzyme and substrate were provided as separate strands (Supplementary Tables 2-3). Under single turnover conditions (20 mM $MgCl_2$, 37°C, 24 hours), only the most enriched sequence from each selection (N15-1 and N20-1) exhibits detectable RNA cleavage activity, and only at trace levels (Fig. 3.3a, Supplementary Fig. 2). This result suggests that threozyme activity may be strongly influenced by temperature. One possible explanation is that the shorter, more conformationally constrained TNA backbone limits access to catalytically productive conformations at lower temperature, requiring thermal activation to facilitate the formation of an active complex. However, other factors, including substrate binding, metal ion coordination, or temperature-dependent folding equilibria, could also contribute to the observed behavior. Consistent with a strong temperature dependence, all six threozymes derived from the

N15 library and three of the six threozymes from the N20 library show increases in catalytic activity when the assay is repeated at 50°C (Fig. 3.3a, Supplementary Fig. 2). Notably, the top performing sequences (N15-1 and N20-1) exhibit a dramatic enhancement in reactivity, with substrate cleavage increasing from ~3-5% at 37°C to >50% at 50°C.

A time-course analysis of the top performing enzymes illustrates the temperature-dependent behavior (Fig. 3.3b-c, Supplementary Fig. 3) of the selected threozymes. Both N15-1 and N20-1 exhibit negligible activity at 37°C, whereas the same reactions performed at 50°C show rapid and sustained product formation. The N15-1 catalyzed reaction reaches ~80% product cleavage within 24 hours, while N20-1 achieves slightly higher activity (~90%) with faster initial rates. The kinetic profiles are consistent with a temperature-activated catalytic mechanism, where elevated temperature enhances the conformational dynamics required for phosphodiester bond cleavage.

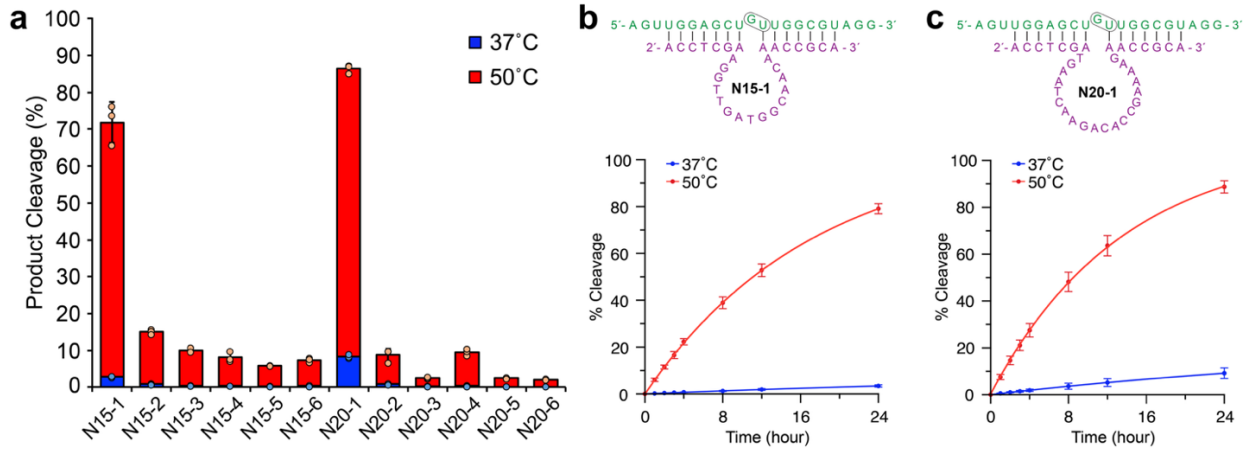

Figure 3.3. Threozyme-mediated RNA cleavage at moderate and elevated temperatures. a, *Activity screen. Single endpoint detection analysis of RNA cleavage mediated by the six most enriched threozymes isolated from the N15 and N20 libraries. Bar graphs denote average RNA cleavage activity after 24 hours of incubation at 37°C (blue) and 50°C (red).* ***b-c,*** *Kinetic curves. Reaction profiles showing RNA cleavage of the most active variants isolated from the N15 (N15-1, panel b) and N20 (N20-1, panel c) libraries at 37°C (blue) and 50°C (red). Enzyme-substrate complex is provided above the plot. The G-U cleavage is site denoted with a circle. Data presented as the mean ± standard deviation (n=3 independent experiments). All reactions were performed in 50 mM Tris (pH 7.5), 10 mM NaCl, 140 mM KCl, and 20 mM $MgCl_2$ with 250 nM substrate and 500 nM enzyme.*

To confirm that RNA cleavage occurs at the intended site, we compared the migration pattern of threozyme-mediated RNA cleavage products to an RNase T1 digestion ladder, which specifically cleaves RNA after guanosine residues, using denaturing PAGE. Both N15-1 and N20-1 generate an RNA product that co-migrates with the expected fragment corresponding to cleavage of the RNA substrate at the desired G-U dinucleotide junction (Supplementary Fig. 4). We next examined the magnesium dependence of the reaction. Increasing the Mg^{2+} concentration from 0 to 20 mM resulted in corresponding increases in RNA cleavage for both N15-1 and N20-1 (Supplementary Fig. 5), with no detectable activity observed in the absence Mg^{2+} ions (0 mM). These results indicate that catalysis proceeds through a magnesium-dependent cleavage mechanism, consistent with divalent metal ion-catalyzed phosphodiester cleavage. Finally, we evaluated the resistance of threozymes to biological nucleases. Preincubation of the enzyme-substrate complexes with Turbo DNase or human RNase H1 had no measurable effect on the catalytic activity of either N15-1 or N20-1 (Supplementary Fig. 6-7), indicating that both enzymes are refractory to biological nucleases. In contrast, Dz 10-23, used as a general model for DNAzyme-mediated RNA cleavage, lost all activity following DNase treatment and exhibited altered cleavage patterns in the presence of RNase H1 (Supplementary Fig. 6-7), consistent with its susceptibility to RNase H1-mediated strand cleavage[44]. Together, these findings reinforce the intrinsic biostability of TNA and highlight its promise for applications in biological environments where resistance to nuclease degradation is critical for function[45].

To evaluate how backbone chemistry might influence catalytic behavior, we evaluated the RNA cleavage activity of Dz 10-23 at physiological and elevated temperature[27]. To obtain measurable reaction kinetics that could be compared with those of the threozymes,

Dz 10-23 reactions were performed under deliberately attenuated conditions using 2 mM Mg^{2+} rather than 20 mM Mg^{2+}. Reactions were evaluated under multiple and single turnover conditions. Under multiple turnover conditions, Dz 10-23 exhibited robust catalytic activity at 37°C, achieving ~80% substrate cleavage in 150 minutes. In contrast, catalytic activity was markedly reduced at 50°C, with cleavage yields remaining below ~15%, even at extended reaction times (Fig. 3.4a, Supplementary Fig. 8). A similar trend was observed under single turnover conditions, where Dz 10-23 achieved ~90% substrate cleavage within 10 minutes at 37˚C but only ~15% at 50˚C (Supplementary Fig. 9). These observations indicate that Dz 10-23 activity decreases substantially at elevated temperature, which is consistent with previous reports describing the temperature-dependence of other RNA-cleaving DNAzymes[46,47].

Thermal denaturation profiles performed in the reaction buffer using a 2'-deoxyguanosine (dG) substitution at the cleavage junction indicate that while substrate dissociation could account for loss of activity at elevated temperature, the Tm value of Dz 10-23 is strikingly similar to that of Tz N20-1, which remains optimal at 50°C (Supplementary Fig. 10). It is worth noting that the dG substitution at the substrate cleavage site could lower the melting temperature of the enzyme-substrate complex by disrupting key interactions involving coordination of the catalytic metal-ion to the 2' hydroxyl group. Indeed, NMR analysis of Dz 10-23 reveals a highly dynamic loop structure coordinated to three divalent metal ions[39,48].

Next, we extended these studies to include chemically synthesized threozymes (Tz's 6-29 and 13-38) previously evolved to cleave RNA with a more flexible active site (Fig. 3.4b-c)[24]. Notably, these enzymes display a reduced temperature dependence, maintaining high catalytic activity at both 37°C and 50°C (Supplementary Fig. 11). The activity profiles of the enzymes evaluated in this study across a range of temperatures (Supplementary Fig. 12) re-

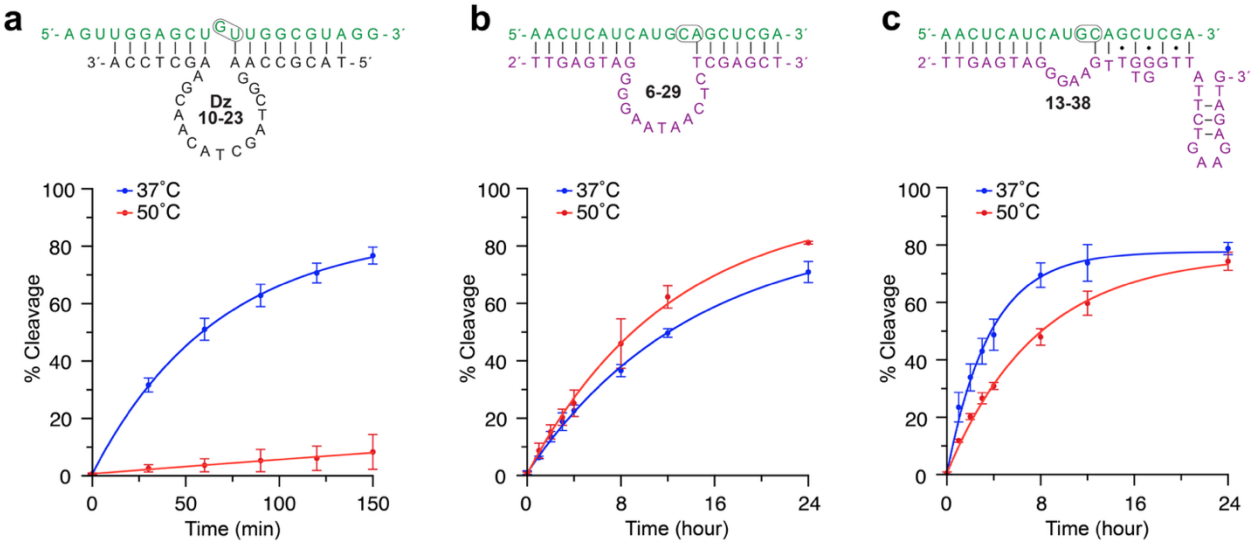

Figure 3.4. Comparative reaction profiles performed at moderate and elevated temperatures. a, *Kinetic curves of Dz 10-23.* ***b-c,*** *Kinetic curves of Tz's 6-29 and 13-38. Reaction profiles show RNA cleavage at 37°C (blue) and 50°C (red). Enzyme-substrate complex is provided above the plot. The cleavage site is denoted with a circle. Data presented as the mean ± standard deviation (n=3 independent experiments). All reactions were performed in 50 mM Tris (pH 7.5), 10 mM NaCl, and 140 mM KCl. Dz catalyzed reactions contained 2 mM $MgCl_2$ with 250 nM substrate and 25 nM enzyme, while the Tz catalyzed reactions contained 20 mM $MgCl_2$ with 250 nM substrate and 500 nM enzyme.*

veal a fundamental difference in the catalytic behavior of nucleic acid enzymes that operate with distinct active site architectures. Enzymes with more conformationally constrained active sites appear to function optimally within a narrow temperature regime, whereas those with more flexible active sites exhibit a broader thermal tolerance, retaining catalytic activity across a wider range of temperatures.

To further evaluate the influence of temperature on catalytic activity, apparent rate constants (k_{obs}) measured at 37°C and 50°C were used to estimate activation energies (E_a) for each catalyst (Supplementary Table 4). The two enzymes isolated from the random sequence libraries, Tz N15-1 and Tz N20-1, exhibit a strong positive temperature dependence, with k_{obs} increasing from 0.02 h^{-1} at 37°C to 0.06-0.07 h^{-1} at 50°C, corresponding to apparent activation energies of 77.5 ± 7.2 and 79.4 ± 2.7 kJ/mol, respectively. In contrast, previously

reported threozymes with more flexible active sites display a reduced or reversed temperature dependence. Tz 6-29 showed only a modest increase in activity with temperature (0.07 to 0.08 h^{-1}), yielding a near zero activation energy (9.1 ± 5.3 kJ/mol), while Tz 13-38 exhibited a 2-fold decrease in activity at elevated temperature (0.27 to 0.13 h^{-1}), corresponding to an apparent negative activation energy of -47.0 ± 5.7 kJ/mol. A similar but more pronounced trend was observed for Dz 10-23, which showed robust activity at 37°C (21.7 h^{-1}) but a greater than 10-fold reduction at 50°C (1.8 h^{-1}), yielding an apparent activation energy of -158.2 ± 14.4 kJ/mol. Collectively, these results demonstrate that the newly identified threozymes exhibit a fundamentally different temperature dependence from both Dz 10-23 and previously characterized threozymes, with catalytic activity increasing rather than decreasing with elevated temperature. This behavior is consistent with a model in which catalysis by the newly selected threozymes requires thermal activation to access productive conformational states.

3.4 Discussion

A central principle of enzymology is that catalytic function emerges from the ability of molecules to access ensembles of interconverting conformations[1]. In proteins, this dynamic plasticity provides a foundation for evolvability, enabling mutations to reshape conformational landscapes and reveal new catalytic states[2-4]. Our results suggest that an analogous principle applies to nucleic acid enzymes, but with an important distinction. While protein dynamics are encoded primarily through side chain interactions[8,9], nucleic acid dynamics are fundamentally constrained more directly by the chemical structure of their sugar-

phosphate backbone[10]. In this context, TNA provides an informative model system for examining how backbone geometry governs the relationship between molecular motion and catalytic function.

The opposing temperature-dependent activity profiles observed for similarly sized DNA and TNA catalysts acting on the same RNA substrate reveal differences in how nucleic acid enzymes access productive transition states. Dz 10-23 exhibits maximal activity near physiological temperature but is strongly attenuated at elevated temperature, whereas Tz's N15-1 and N20-1 display only minimal activity at 37°C and become highly active at 50°C. Based on this data and their associated melting curves, we suggest a model in which TNA catalysis depends on conformational states that are only sparsely populated at low temperature. Raising the temperature then provides the thermal energy necessary to overcome this barrier, allowing threozymes to access conformations that are more compatible with the geometric constraints of site-specific RNA hydrolysis.

Our comparison with previously reported threozymes that possess more flexible active sites reinforces this model. Unlike N15-1 and N20-1, these catalysts remain active across a broader range of temperatures, suggesting that local relaxation of the active site can partially offset intrinsic constraints imposed by the TNA backbone. Such findings point to a continuum in which catalytic efficiency is shaped by the balance between backbone structure and access to dynamic catalytic states. Highly constrained architectures may favor precise positioning but at the cost of reduced conformational flexibility, whereas less constrained systems may sample a broader range of states, including those compatible with catalysis. This interpretation is consistent with the NMR structure of 10-23 showing extensive sampling of conformational space (Supplementary Fig. 13)[39]. As expected, there is likely to be a

limit to this balance, as some genetic systems may prove too rigid or too flexible to support efficient catalysis, but systematically testing this idea across a range of XNA systems would offer clues into how different classes of nucleic acid systems fold and function[50]. Additionally, base modifications could influence the temperature-dependent activity of nucleic acid enzymes by altering the reaction mechanism[51-53].

These findings have important implications for the evolvability of nucleic acid enzymes. Although in vitro selection has now yielded multiple RNA-cleaving threozymes, demonstrating that functional solutions do exist in TNA sequence space, their comparatively low activity and pronounced temperature dependence suggests that the accessible fitness landscape is narrower than that observed for comparable DNA enzymes[28-30]. Such compression could help explain both the limited diversity of catalytic motifs recovered in our selections and the failure to isolate highly active threozymes under standard conditions. More broadly, our results support the idea that backbone chemistry does not simply modulate the stability of the polymer, but also defines the dynamic landscape from which catalytic function can emerge. Such factors could influence the choice of genetic polymers evaluated for practical applications as well as various scenarios used to describe the emergence of the RNA world[14-18].

In summary, our study establishes a direct link between backbone geometry and catalytic activity in nucleic acid enzymes. By showing that TNA-mediated catalysis is governed by the temperature-dependent activation of conformational states, we provide experimental evidence that backbone chemistry can impose fundamental limits on evolvability, which could have important implications for RNA world models and biomedical applications.

3.5 Methods

Materials. TNA triphosphates and phosphoramidites were synthesized in-house[41,42]. DNA phosphoramidite monomers were purchased from Glen Research (Sterling, VA). DNA triphosphates were purchased from Thermo Fisher Scientific (Waltham, MA). DNA/RNA oligonucleotides and DNA libraries were purchased from Integrated DNA Technologies (Coralville, Iowa). Glen-Pak DNA Purification Cartridges were purchased from Glen Research (Sterling, VA). T7 DNA ligase and 10-92 TNA polymerase were expressed and purified from E. coli[50]. T4 DNA ligase buffer, ThermoPol buffer, and Bst 3.0 DNA polymerase were purchased from New England Biolabs (Ipswich, MA). PCRBIO HiFi polymerase and PCRBIO HIFI buffer were purchased from PCR Biosystems (London, UK). Phenol:chloroform:isoamyl alcohol (25:24:1 v/v, saturated with 10 mM Tris, pH 8.0, 1 mM EDTA) was purchased from Sigma-Aldrich (St. Louis, MO). Amicon ultra-centrifugal filters were purchased from Millipore Sigma (Burlington, MO). DNA Clean and Concentrator-5 was purchased from Zymo Research (Irvine, CA). Dynabeads MyOne Strepavidin T1 beads were purchased from Thermo Fisher Scientific (Waltham, MA). MagneSphere 12-position rack was purchased from Promega (Madison, WI). RNase T1 and Turbo DNase were purchased from Thermo Fisher Scientific (Waltham, MA). Human RNase H1 was purchased from Abcam (Cambridge, UK). Refer to Supplementary Table 1 for DNA library and primer sequences. Refer to Supplementary Table 2 for threozyme sequences. Refer to Supplementary Table 3 for RNA substrate sequences.

Library preparation for DNA display selection strategy.

Library design. Inspired by the 10-23 DNAzyme framework, the DNA library features a central random region of 15 or 20 nucleotides (A:G:C:T = 25:25:25:25) as the catalytic core region. The random region is flanked by defined binding arm regions of 10 nucleotides that

recognize the desired RNA substrate. Expanding further beyond both binding arm regions are the primer-binding sites of 20 nucleotides.

Hairpin ligation. A self-priming DNA library was generated by ligating a DNA library (5 μM) to a phosphorylated DNA hairpin primer (6 μM) in 1x T4 DNA ligase buffer using T7 DNA ligase (1 μM). The DNA library was annealed to the DNA hairpin primer by heating at 95°C for 5 min and cooling on ice for 5 min. The reaction was then initiated with the addition of T7 DNA ligase and incubated overnight at 24°C. The resulting self-priming DNA library was purified by 10% denaturing polyacrylamide gel electrophoresis (PAGE), electroeluted, and desalted using an Amicon™ ultra-centrifugal filter.

TNA transcription. The self-priming DNA library was extended with tNTPs to generate a chimeric DNA/TNA heteroduplex. The reaction was initiated with the addition of 10-92 TNA polymerase (2 μM) followed by tNTPs (0.1 mM of each tATP/tCTP/tGTP/tTTP) and incubated for 1 h at 40°C. Afterwards, an equal volume of phenol:chloroform:isoamyl alcohol (25:24:1 v/v) was added to extract excess polymerase following manufacturer's protocol. Following extraction, the top aqueous layer was collected and desalted using an Amicon™ ultra-centrifugal filter.

Strand displacement. TNA was displaced by extending a chimeric 5'-biotin DNA primer containing the RNA substrate. First, the DNA primer (2 μM) was annealed to the hairpin loop of the library (1 μM) in 1x ThermoPol® buffer by heating to 95°C and cooling on ice for 5 min. The reaction was then supplemented with an additional 5 mM of $MgCl_2$ before adding Bst 3.0 DNA polymerase (80 U/mL) and dNTPs (0.5 mM of each dATP/dCTP/dGTP/dTTP) to initiate the reaction and incubated for 1 h at 50°C. Excess polymerase was extracted, and the aqueous layer was collected as described for TNA transcription. Residual phenol was removed by

adding 500 µL of ethanol to the desalted solution and the TNA library was dried by a SpeedVac concentrator.

Selection by DNA display strategy. MyOne T1 streptavidin beads (35.7 µL) were pre-treated for RNA applications following manufacturer's protocol and equilibrated in 500 µL of binding buffer (50 mM Tris (pH 7.5), 150 mM NaCl, 0.01% Tween-20, 0.5 mM EDTA) for 30 min at 24°C with rotation. The TNA library (100 pmol) was then incubated with the pre-treated magnetic beads in 500 µL of binding buffer for 30 min at 24°C with rotation to immobilize the library on the beads. The beads were washed 3-4 times with 500 µL of pre-cleavage buffer (50 mM Tris (pH 7.5), 10 mM NaCl, 140 mM KCl). Following the washes, 500 µL of cleavage buffer (50 mM Tris (pH 7.5), 10 mM NaCl, 140 mM KCl, 20 mM $MgCl_2$) was added to the reaction tube to initiate RNA cleavage. The selection stringency was increased over 8 rounds at a constant temperature of 37°C. The starting parameters were 20 mM $MgCl_2$ and 19 hours. The magnesium concentration and reaction time were incrementally decreased to a final condition of 0.5 mM $MgCl_2$ and 15 min.

Threozyme synthesis. All threozymes were prepared by solid-phase oligonucleotide synthesis using an automated Dr. Oligo DNA synthesizer on a 1-µmol scale universal CPG column (Glen Research) with optimized coupling times. Oligonucleotides were removed from the column and deprotected by incubation in ammonia gas for 2 h at 80°C (60 psi), and purified by ion-pair reversed-phase HPLC followed by a Glen-Pak™ DNA Purification Cartridge (Glen Research). The samples were lyophilized to dryness, resuspended in water, UV quantified, and verified by MALDI-TOF mass spectroscopy.

Activity assay. Threozymes were assayed under single turnover conditions with 500 nM Tz and 250 nM IR680-labeled RNA substrate (1:2, S:E) in reaction buffer comprised of 50 mM

Tris-HCl (pH 7.5), 10 mM NaCl, 140 mM KCl, and 20 mM $MgCl_2$. Reactions were initiated with the addition of $MgCl_2$ and incubated at either 37˚C or 50˚C for up to 24 hours. Aliquots (1.5 µL) of each reaction mixture were removed at designated time points and quenched in 16.5 µL formamide stop buffer (99% deionized formamide, 25 mM EDTA). Quenched samples were denatured at 95°C for 10 min and resolved using 20% denaturing PAGE. The gel was imaged using an Odyssey CLx imaging system (LI-COR) and quantified using Image Studio 5.2 (LI-COR).

Product validation. RNA substrate (1 µM) was digested by 1 U of RNase T1 in 50 mM Tris (pH 7.5), 10 mM NaCl, and 140 mM KCl at room temperature for 1 min to generate an RNA ladder. For threozyme-catalyzed reactions, 500 nM Tz and 250 nM IR680-labeled RNA substrate (1:2, S:E) were incubated in the same buffer used for RNase T1 digestion, but with the addition of 20 mM $MgCl_2$. Samples were collected, quenched, and analyzed as described for the activity assay.

Magnesium dependence screen. Threozymes were assayed under single turnover conditions with 500 nM Tz and 250 nM IR680-labeled RNA substrate (1:2, S:E) in reaction buffer comprised of 50 mM Tris-HCl (pH 7.5), 10 mM NaCl, 140 mM KCl, and varied concentrations of $MgCl_2$ (0, 1, 5, 10, and 20 mM). Reactions were initiated with the addition of $MgCl_2$ and incubated at 50˚C for 18 hours. Samples were collected, quenched, and analyzed as described for the activity assay.

Temperature dependence screen. DNAzymes and threozymes were assayed across a range of temperatures. All reactions were incubated in 50 mM Tris (pH 7.5), 10 mM NaCl, and 140 mM KCl for 8 hours. Dz catalyzed reactions contained 2 mM $MgCl_2$ with 250 nM IR680-labeled RNA substrate and 25 nM enzyme, while the Tz catalyzed reactions contained 20 mM

$MgCl_2$ with 250 nM IR680-labeled or Cy5-labeled RNA substrate and 500 nM enzyme. Samples were collected, quenched, and analyzed as described for the activity assay.

Turbo DNase assay. DNAzymes and threozymes were pretreated with Turbo DNase (2 U) in 50 mM Tris (pH 7.5), 10 mM NaCl, and 140 mM KCl at 37°C for 10 min and 60 min, respectively. Dz catalyzed reactions contained 2 mM $MgCl_2$, while Tz reactions contained 20 mM $MgCl_2$. After preincubation, the IR680-labeled RNA substrate was added to the reaction, reaching final concentrations of 250 nM substrate and 250 nM enzyme (1:1, S:E). For the Dz reactions, temperature was maintained at 37˚C after RNA substrate addition and allowed to incubate for an additional hour. For the Tz reactions, the temperature was increased to 50°C after RNA substrate addition and allowed to incubate for an additional 18 hours.

RNase H1 assay. DNAzymes and threozymes were assayed under single turnover with 250 nM enzyme and 250 nM IR680-labeled RNA substrate (1:1, S:E) in the absence and presence of RNase H1. All reactions were incubated in 50 mM Tris (pH 7.5), 10 mM NaCl, and 140 mM KCl at 37˚C. Dz catalyzed reactions contained 2 mM $MgCl_2$, while the Tz catalyzed reactions contained 20 mM $MgCl_2$. For the Tz reactions, the reaction temperature was increased to 50°C for an additional 4 hours after 1 hour of initial incubation at 37˚C.

Melting temperature (Tm) study. All melts were performed with 1:1 oligonucleotide stoichiometry (1 μM enzyme + 1 μM RNA substrate) in the same buffer used for the activity assay (50 mM Tris (pH 7.5), 10 mM NaCl, 140 mM KCl, and either 2 mM or 20 mM $MgCl_2$). Prior to melting, the strands were annealed in an Eppendorf tube by heating to 95ºC for 5 minutes and cooling on ice. Melting curves were obtained in the forward melting direction in a quartz cuvette of 1-cm path length with a temperature gradient of 20º to 90ºC and a ramping rate of 1°C per min by monitoring the change in UV absorbance at 260 nm using a Cary 100 UV-

Vis spectrophotometer equipped with a Peltier thermal controller. Tm values were determined by the hyperchromicity method using Cary WinUV 4.2 (468).

Rate constant (k_{obs}) determination. Observed rate constants of single turnover assays were obtained by fitting the percentage of the cleaved substrate over the reaction time to the one-phase association curve (1) using LabPlot 2.10.1 (KDE).

$$Y = Y_0 + (Y_{plateau} - Y_0) \times (1 - e^{-k_{obs} \times t}) \quad (1)$$

Y is the percent cleavage at finite time t, Y_0 is the percent cleavage at time equals zero, $Y_{plateau}$ is the percent cleavage at an infinite time where the reaction reaches a plateau, and k_{obs} is the observed pseudo-first-order rate constant.

Activation energy (E_a) determination. Apparent activation energies were calculated using the two-point form of the Arrhenius equation (2).

$$\ln \frac{k_2}{k_1} = \frac{E_a}{R}\left(\frac{1}{T_1} - \frac{1}{T_2}\right) \quad (2)$$

T_1 and T_2 are temperatures (K) of the reaction, k_1 and k_2 are observed rate constants of the reaction at the respective temperatures, R is the universal gas constant (8.314 $J/mol \cdot K$), and E_a is the activation energy.

Statistics and reproducibility. The mean and standard deviation were calculated in Microsoft Excel 16.78 (23100802). All experiments were reproduced in sets of two or three independent replicates. No data were excluded from the analyses. Samples sizes were determined using sample sizes standard in nucleic acid research (duplicate or triplicate). The investigators were not blinded to allocation during the experiments and outcome assessments.

3.6 Data Availability

The authors declare that the data supporting the findings of this study are available within the article and its Supplementary Information file. All raw DNA sequences collected from the threozyme selection have been deposited in the Sequence Read Archive and can be found in the NCBI BioProject database under accession code PRJNA1499794. Structural information referenced here can be found in the Protein Data Bank under accession code 7PDU.

3.7 Acknowledgements

We would like to thank N. Setterholm and M. Hajjar for technical assistance and members of the Chaput lab for their helpful comments and suggestions. We also gratefully acknowledge the Genomics Research and Technology Hub (GRT Hub) at UCI for their NGS services.

3.8 Funding

JC declares no relevant funding. EL declares no relevant funding.

3.9 Author Contributions

JC and EL conceived the project and designed the experiments. EL evolved the enzyme and performed the biochemical characterization. JC and EL wrote the manuscript.

3.10 Competing Interests

The authors declare no competing interests.

3.11 References

(1) Benkovic, S. J. & Hammes-Schiffer, S. A perspective on enzyme catalysis. *Science* **301**, 1196-1202 (2003).

(2) Khersonsky, O. & Tawfik, D. S. Enzyme promiscuity: a mechanistic and evolutionary perspective. *Annu. Rev. Biochem.* **79**, 471-505 (2010).

(3) Arnold, F. H. The nature of chemical innovation: new enzymes by evolution. *Q. Rev. Biophys.* **48**, 404-410 (2015).

(4) Hajjar, M. *et al.* Directed evolution of a TNA polymerase identifies independent paths to fidelity and catalysis. *Nat. Commun.* **17**, 925 (2026).

(5) Tokuriki, N. & Tawfik, D. S. Protein dynamism and evolvability. *Science* **324**, 203-207 (2009).

(6) Chaput, J. C., Egli, M. & Herdewijn, P. The XNA Alphabet. *Nucleic Acids Res.* **53**, gkaf635 (2025).

(7) Chaput, J. C. & Herdewijn, P. What Is XNA? *Angew. Chem. Int. Ed. Engl.* **58**, 11570-11572 (2019).

(8) Anfinsen, C. B. Principles that govern the folding of protein chains. *Science* **181**, 223-230 (1973).

(9) Dill, K. A. Dominant forces in protein folding. *Biochemistry* **29**, 7133-7155 (1990).

(10) Egli, M. & Pallan, P. S. Insights from crystallographic studies into the structural and pairing properties of nucleic acid analogs and chemically modified DNA and RNA oligonucleotides. *Annu Rev Biophys Biomol Struct* **36**, 281-305 (2007).

(11) Pallan, P. S., Lubini, P., Bolli, M. & Egli, M. Backbone-base inclination as a fundamental determinant of nucleic acid self- and cross-pairing. *Nucleic Acids Res.* **35**, 6611-6624 (2007).

(12) Anosova, I. *et al.* The structural diversity of artificial genetic polymers. *Nucleic Acids Res.* **44**, 1007-1021 (2016).

(13) Ramaswamy, A., Froeyen, M., Herdewijn, P. & Ceulemans, A. Helical structure of xylose-DNA. *J. Am. Chem. Soc.* **132**, 587-595 (2010).

(14) Orgel, L. E. A simpler nucleic acid. *Science* **290**, 1306-1307 (2000).

(15) Joyce, G. F. The antiquity of RNA-based evolution. *Nature* **418**, 214-221 (2002).

(16) Yu, H., Zhang, S. & Chaput, J. C. Darwinian evolution of an alternative genetic system provides support for TNA as an RNA progenitor. *Nat. Chem.* **4**, 183-187 (2012).

(17) Wang, F. *et al.* Cellular uptake, tissue penetration, biodistribution, and biosafety of threose nucleic acids: Assessing in vitro and in vivo delivery. *Mater Today Bio* **15**, 100299 (2022).

(18) Matsuda, S. *et al.* Shorter Is Better: The alpha-(l)-Threofuranosyl Nucleic Acid Modification Improves Stability, Potency, Safety, and Ago2 Binding and Mitigates Off-Target Effects of Small Interfering RNAs. *J. Am. Chem. Soc.* **145**, 19691-19706 (2023).

(19) Schöning, K. U. *et al.* Chemical etiology of nucleic acid structure: the a-threofuranosyl-(3' →2') oligonucleotide system. *Science* **290**, 1347-1351 (2000).

(20) Chaput, J. C. Redesigning the Genetic Polymers of Life. *Acc. Chem. Res.* **54**, 1056-1065 (2021).

(21) Lozoya-Colinas, A., Yu, Y. & Chaput, J. C. Functionally Enhanced XNA Aptamers Discovered by Parallelized Library Screening. *J. Am. Chem. Soc.* **145**, 25789-25796 (2023).

(22) Dunn, M. R., McCloskey, C. M., Buckley, P., Rhea, K. & Chaput, J. C. Generating biologically stable TNA aptamers that function with high affinity and thermal stability. *J. Am. Chem. Soc.* **142**, 7721-7724 (2020).

(23) Li, X., Li, Z. & Yu, H. Selection of threose nucleic acid aptamers to block PD-1/PD-L1 interaction for cancer immunotherapy. *Chem. Commun.* **56**, 14653-14656 (2020).

(24) Wang, Y. *et al.* An RNA-cleaving threose nucleic acid enzyme capable of single point mutation discrimination. *Nat. Chem.* **14**, 350-359 (2022).

(25) Wang, Y. *et al.* A Threose Nucleic Acid Enzyme with RNA Ligase Activity. *J. Am. Chem. Soc.* **143**, 8154-8163 (2021).

(26) Pallan, P. S. *et al.* Why does TNA cross-pair more strongly with RNA than with DNA? An answer from X-ray analysis. *Angew. Chem. Int. Ed.* **42**, 5893-5895 (2003).

(27) Santoro, S. W. & Joyce, G. F. A general purpose RNA-cleaving DNA enzyme. *Proc. Natl. Acad. Sci. U.S.A.* **94**, 4262-4266 (1997).

(28) Joyce, G. F. Directed Evolution of Nucleic Acid Enzymes. *Annu. Rev. Biochem.* **73**, 791-836 (2004).

(29) Silverman, S. K. Deoxyribozymes: selection design and serendipity in the development of DNA catalysts. *Acc. Chem. Res.* **42**, 1521-1531 (2009).

(30) Wilson, D. S. & Szostak, J. W. In vitro selection of functional nucleic acids. *Annu. Rev. Biochem.* **68**, 611-647 (1999).

(31) Cruz, R. P., Withers, J. B. & Li, Y. Dinucleotide junction cleavage versatility of 8-17 deoxyribozyme. *Chem. Biol.* **11**, 57-67 (2004).

(32) Wang, Y., Nguyen, K., Spitale, R. C. & Chaput, J. C. A biologically stable DNAzyme that efficiently silences gene expression in cells. *Nat. Chem.* **13**, 319-326 (2021).

(33) Nguyen, K., Malik, T. N. & Chaput, J. C. Chemical evolution of an autonomous DNAzyme with allele-specific gene silencing activity. *Nat. Commun.* **14**, 2413 (2023).

(34) Lee, E. M., Nguyen, K., Setterholm, N. A., Malik, T. N. & Chaput, J. C. Allele-specific knockdown by an engineered DNAzyme capable of RNase H1 evasion. *Nucleic Acids Res.* **54** (2026).

(35) McCormick, F. KRAS as a Therapeutic Target. *Clin. Cancer Res.* **21**, 1797-1801 (2015).

(36) Chiosea, S. I., Sherer, C. K., Jelic, T. & Dacic, S. KRAS mutant allele-specific imbalance in lung adenocarcinoma. *Mod. Pathol.* **24**, 1571-1577 (2011).

(37) Nguyen, K., Wang, Y. J., England, W. E., Chaput, J. C. & Spitale, R. C. Allele-Specific RNA Knockdown with a Biologically Stable and Catalytically Efficient XNAzyme. *J. Am. Chem. Soc.* **143**, 4519-4523 (2021).

(38) Santoro, S. W. & Joyce, G. F. Mechanism and utility of an RNA-cleaving DNA enzyme. *Biochemistry* **37**, 13330-13342 (1998).

(39) Borggrafe, J. *et al.* Time-resolved structural analysis of an RNA-cleaving DNA catalyst. *Nature* **601**, 144-149 (2022).

(40) Ichida, J. K. *et al.* An in vitro selection system for TNA. *J. Am. Chem. Soc.* **127**, 2802-2803 (2005).

(41) Sau, S. P., Fahmi, N. E., Liao, J.-Y., Bala, S. & Chaput, J. C. A scalable synthesis of α-L-threose nucleic acid monomers. *J. Org. Chem.* **81**, 2302-2307 (2016).

(42) Negria, S., Jia, Y., Setterholm, N. A., Barpuzary, B. & Chaput, J. C. Scalable Multistep One-Pot Synthesis of Natural and Modified Nucleoside Triphosphates. *J. Org. Chem.* **90**, 5936-5948 (2025).

(43) Maola, V. A. *et al.* Directed evolution of a highly efficient TNA polymerase achieved by homologous recombination. *Nature Catalysis* **7**, 1173-1185 (2024).

(44) Young, D. D., Lively, M. O. & Deiters, A. Activation and deactivation of DNAzyme and antisense function with light for the photochemical regulation of gene expression in mammalian cells. *J. Am. Chem. Soc.* **132**, 6183-6193 (2010).

(45) Culbertson, M. C. *et al.* Evaluating TNA stability under simulated physiological conditions. *Bioorg. Med. Chem. Lett.* **26**, 2418-2421 (2016).

(46) Ting, R., Thomas, J. M., Lermer, L. & Perrin, D. M. Substrate specificity and kinetic framework of a DNAzyme with an expanded chemical repertoire: a putative RNaseA mimic that catalyzes RNA hydrolysis independent of a divalent metal cation. *Nucleic Acids Res.* **32**, 6660-6672 (2004).

(47) Bonaccio, M., Credali, A. & Peracchi, A. Kinetic and thermodynamic characterization of the RNA-cleaving 8-17 deoxyribozyme. *Nucleic Acids Res.* **32**, 916-925 (2004).

(48) Borggrafe, J., Gertzen, C. G. W., Viegas, A., Gohlke, H. & Etzkorn, M. The architecture of the 10-23 DNAzyme and its implications for DNA-mediated catalysis. *FEBS J* **290**, 2011-2021 (2023).

(49) Anosova, I. *et al.* Structural insights into conformational differences between DNA/TNA and RNA/TNA chimeric duplexes. *ChemBioChem* **17**, 1705-1708 (2016).

(50) Nikoomanzar, A., Chim, N., Yik, E. J. & Chaput, J. C. Engineering polymerases for applications in synthetic biology. *Q. Rev. Biophys.* **53**, e8 (2020).

(51) Hollenstein, M., Hipolito, C. J., Lam, C. H. & Perrin, D. M. A self-cleaving DNA enzyme modified with amines, guanidines and imidazoles operates independently of divalent metal cations (M2+). *Nucleic Acids Res.* **37**, 1638-1649 (2009).

(52) Raz, M. H. & Hollenstein, M. Probing the effect of minor groove interactions on the catalytic efficiency of DNAzymes 8-17 and 10-23. *Mol. Biosyst.* **11**, 1454-1461 (2015).

(53) Paul, S., Wong, A., Liu, L. T. & Perrin, D. M. Selection of M(2+) -Independent RNA-Cleaving DNAzymes with Side-Chains Mimicking Arginine and Lysine. *Chembiochem* **23**, e202100600 (2022).

CHAPTER 4: Conclusion

4.1 Summary of Results

This dissertation set out to explore TNA not merely as a stable alternative to DNA and RNA, but as a functional genetic polymer capable of supporting molecular behaviors beneficial across different applications. The full extent of TNA's potential is still being uncovered, and insights gained will cultivate deeper understanding of nucleic acid structure and in-form the design of XNA-based molecular tools.

Chapter 1 established the chemical resilience of TNA under acidic, high-temperature conditions.[1] Comparing DNA, RNA, and TNA side-by-side at pH 3.3 and 90°C, TNA proved dramatically more resistant to acid degradation than either natural nucleic acid, with a half-life roughly 35-fold longer than DNA and 9-fold longer than RNA. Mechanistic work using RP-HPLC, mass spectrometry, and molecular dynamics traced this stability to the position of TNA's phosphodiester linkage at the 2′ position of the threose sugar, which inductively destabilizes the oxocarbenium ion intermediate responsible for acid-catalyzed depurination which is the rate-limiting step of degradation. Strand scission was shown to proceed through β-elimination of the 2′-phosphodiester linkage, a distinct pathway from the 3′-elimination mechanism that governs DNA breakdown, and this behavior was corroborated using 2′,5′-DNA and 2′-OMe-RNA as backbone-matched controls. Together, these findings provided the first detailed mechanistic account of TNA's acid stability, establishing a chemical rationale for its durability under harsh acidic conditions at high temperatures and offering insights into unique physicochemical properties available to evolvable non-natural genetic polymers.

Building on TNA's favorable biophysical properties, Chapter 2 applied TNA as a chemical modification to overcome a long-standing limitation of RNA-cleaving DNAzymes, that of

which is unwanted engagement by cellular RNase H1.[2] A systematic TNA walk through the catalytic core of the Dz46 DNAzyme identified position dC3 as a hotspot that enhanced RNA cleavage activity, while strategic placement of two TNA residues in the 5′ binding arm was sufficient to abolish RNase H1 recognition without sacrificing catalytic function. Combining both modifications into a single lead construct, tC3+, produced a DNAzyme with both improved turnover and near-complete RNase H1 evasion, enabling a truly autonomous, allele-specific cleavage mechanism. In mammalian cells, tC3+ achieved selective knockdown of oncogenic KRAS G12V mutation in both homozygous and heterozygous mammalian cell types while sparing the wild-type allele. Furthermore, the generalizability of the tC3+ architecture was validated against two additional clinically relevant targets, PCSK9 and GATA3, at both the RNA and protein level. This work demonstrated TNA as a powerful tool for engineering DNAzymes with enhanced intracellular activity and allele-specific precision, establishing a framework for XNA-based therapeutic DNAzyme design.

Chapter 3 investigated how TNA's backbone architecture constrains its evolutionary potential as a catalytic scaffold, extending the protein-folding principle that conformational dynamism underlies evolvability to nucleic acid enzymes.[3] Newly evolved threozymes selected to cleave the same KRAS G12V RNA substrate as the well-characterized 10-23 DNAzyme displayed an opposite temperature dependence. Dz 10-23 was maximally active at 37°C but lost most activity at 50°C, while the threozymes were nearly inactive at 37°C but became highly active at 50°C, with apparent activation energies indicating that TNA catalysis must overcome a substantially higher free-energy barrier than DNA catalysis. This behavior was interpreted as a signature of TNA's shorter, more conformationally restricted backbone, which limits access to catalytically productive folding states at low temperature and requires

thermal activation to populate them. Consistent with this model, previously reported threozymes engineered with more flexible active sites showed a much narrower temperature dependence, linking architectural flexibility to broadened catalytic tolerance and supporting the conclusion that backbone chemistry imposes fundamental limits on the evolvability of a genetic polymer.

4.2 Future Perspective

Taken together, this body of work reflects a broader pattern in XNA research. Fundamental questions about a synthetic genetic polymer's basic chemistry and structure have steadily given rise to practical tools with real-world promise. The structural and functional exploration of current XNAs like TNA will continue to inform design principles for future XNAs used in applied research. To truly reach XNA's full potential, continued progress will be needed in engineering enzymes to expand XNA manipulation and developing new chemistries to broaden its functional repertoire. Looking ahead, the next major leap for the field will depend less on discovering new applications and more on building the enzymatic infrastructure to support them. XNA-compatible enzymes remain limited to a small set of polymerases and reverse transcriptases with narrow substrate scope, and no enzyme yet exists that can edit XNA with the precision that restriction enzymes and ligases do for DNA. Expanding this toolkit through rational design and directed evolution would unlock more efficient in vitro selection, DNA-independent enzymatic XNA synthesis, and reliable sequencing strategies, all of which remain key bottlenecks in the field. As these tools mature, XNAs like TNA are well positioned to move beyond a chemical curiosity and into a mainstream platform for next-generation molecular medicine and biotechnologies.

4.3 References

(1) Lee, EM, Setterholm, NA, Hajjar, M, Barpuzary, B, Chaput, JC. Stability and mechanism of threose nucleic acid toward acid-mediated degradation. *Nucleic Acids Res.* **51**, 9542-9551 (2023). doi:10.1093/nar/gkad716.

(2) Lee, EM*, Nguyen, K*, Setterholm, NA, Malik, TN, Chaput, JC. Allele-specific knockdown by an engineered DNAzyme capable of RNase H1 evasion. *Nucleic Acids Res.* **54**, gkaf1476 (2026). doi:10.1093/nar/gkaf1476.

(3) Lee EM and Chaput JC. Dynamism and Evolvability in Nucleic Acid Enzymes (manuscript in press).

APPENDIX A: Supplementary Data for Chapter 1

Supplementary Table 1. List of oligonucleotides.

#	Identifier	Sequence	Length (bp)	Calc. MW (g/mol)	Obs. MW (g/mol)
1	RandSeq2 DNA	5'-d(CCG TAG TGA AAG ATC CCT GTT CAG)-3'	24	7352.8	7354.5
2	RandSeq2 RNA	5'-r(CCG UAG UGA AAG AUC CCU GUU CAG)-3'	24	7652.6	7654.7
3	RandSeq2 TNA	3'-t(CCG TAG TGA AAG ATC CCT GTT CAG)-2'	24	7016.3	7016.9
4	RandSeq2 2-5	5'-d(CCG TAG TGA AAG ATC CCT GTT CAG)-2'	24	7352.8	7357.9
5	DNA T_6AT_9	5'-d(TTT TTT ATT TTT TTT T)-3'	16	4814.2	4814.9
6	TNA T_6AT_9	3'-t(TTT TTT ATT TTT TTT T)-2'	16	4589.7	4590.6
7	TNA T_6tAPT_9	3'-t(TTT TTT) tAP t(TT TTT TTT T)-2'	16	4472.6	4473.4
8	2',5' T_6AT_9	5'-d(TTT TTT) A d(TT TTT TTT T)-2'	16	4814.2	4812.4
9	2'-OMe U_6AU_9	5'-m(UUU UUU AUU UUU UUU U)-3'	16	5084.2	5085.3
10	2'-OMe T_6mAT_9	5'-d(TTT TTT) mA d(TT TTT TTT T)-2'	16	4844.2	4846.3
11	DNA dT_9	5'-d(TTT TTT TTT)-3'	9	2675.8	2674.1
12	DNA pdT_9	5'-phos-d(TTT TTT ATT TTT TTT T)-3'	9	2755.8	2755.3
13	DNA dT_6	5'-d(TTT TTT)-3'	6	1763.2	1763.0
14	DNA dT_6p	5'-d(TTT TTT)-phos-3'	6	1843.2	1842.7
15	TNA tT_9	3'-t(TTT TTT TTT)-2'	9	2549.5	2549.7
16	TNA ptT_9	3'-phos-t(TTT TTT ATT TTT TTT T)-2'	9	2629.5	2629.7
17	TNA tT_6	3'-t(TTT TTT)-2'	6	1679.0	1680.1
18	TNA tT_6p	3'-t(TTT TTT)-phos-2'	6	1759.0	1759.4

All masses were determined by MALDI-TOF mass spectrometry.
tAP bases are abasic TNA.
Underlined bases are 2',5'-linked DNA.
mN bases are 2'-OMe RNA.

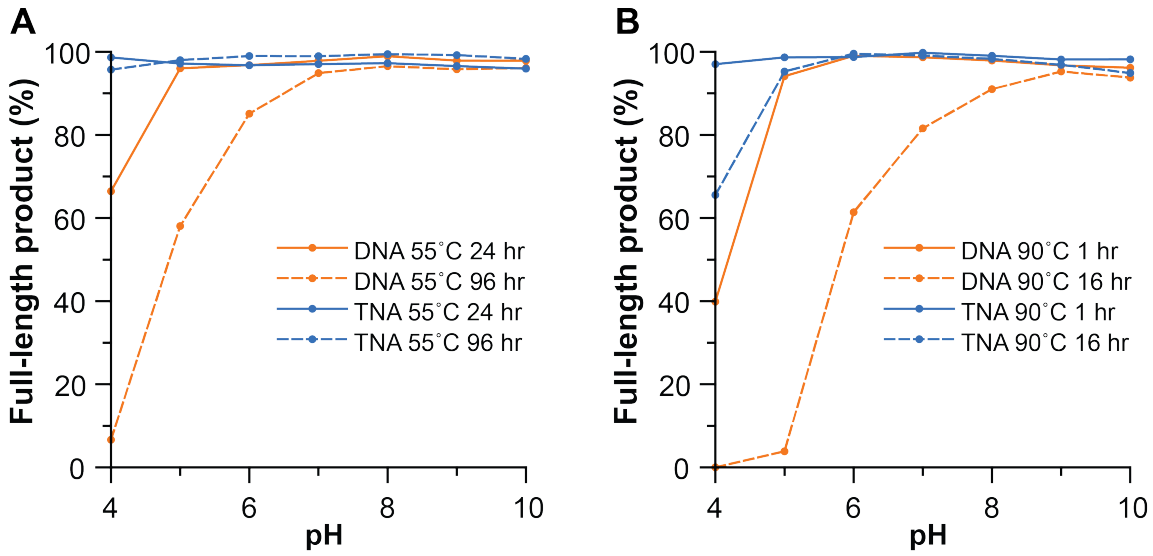

Supplementary Figure 1. Preliminary assessment of the acid stability of DNA and TNA under varying pH and temperature conditions. *A) Stability profile of DNA and TNA observed across a pH range of 4 to 10 at 55°C. B) Stability profile of DNA and TNA observed across a pH range of 4 to 10 at 90°C.*

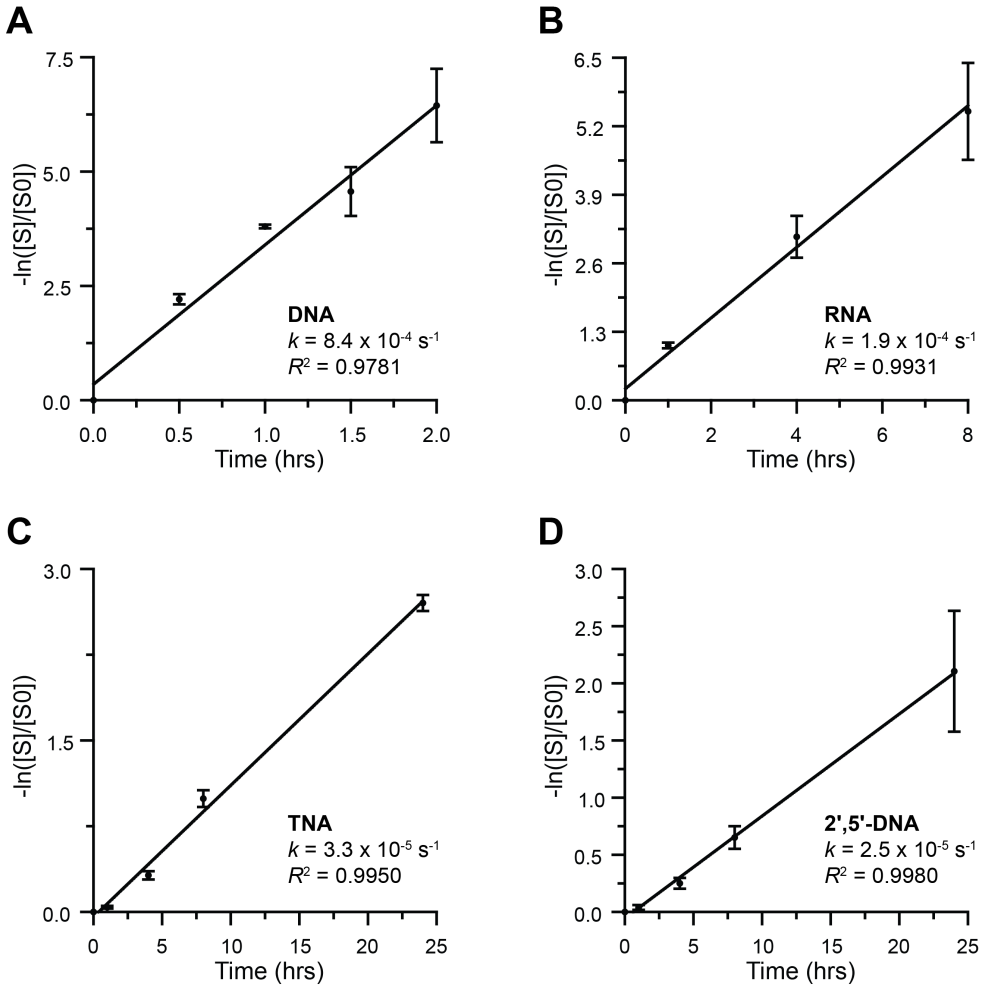

Supplementary Figure 2. Linear plots of ln[S]/[S$_0$] versus time. *First order rate constants (k) for acid-mediated degradation of DNA (A), RNA (B), TNA (C), and 2',5'-DNA (D) were obtained from the slope of the depicted linear plots, where [S]/[S$_0$] is the ratio of the remaining FLP to the starting FLP as determined by HPLC peak integration at the specified time points. Error bars denote ± standard deviation (n=3).*

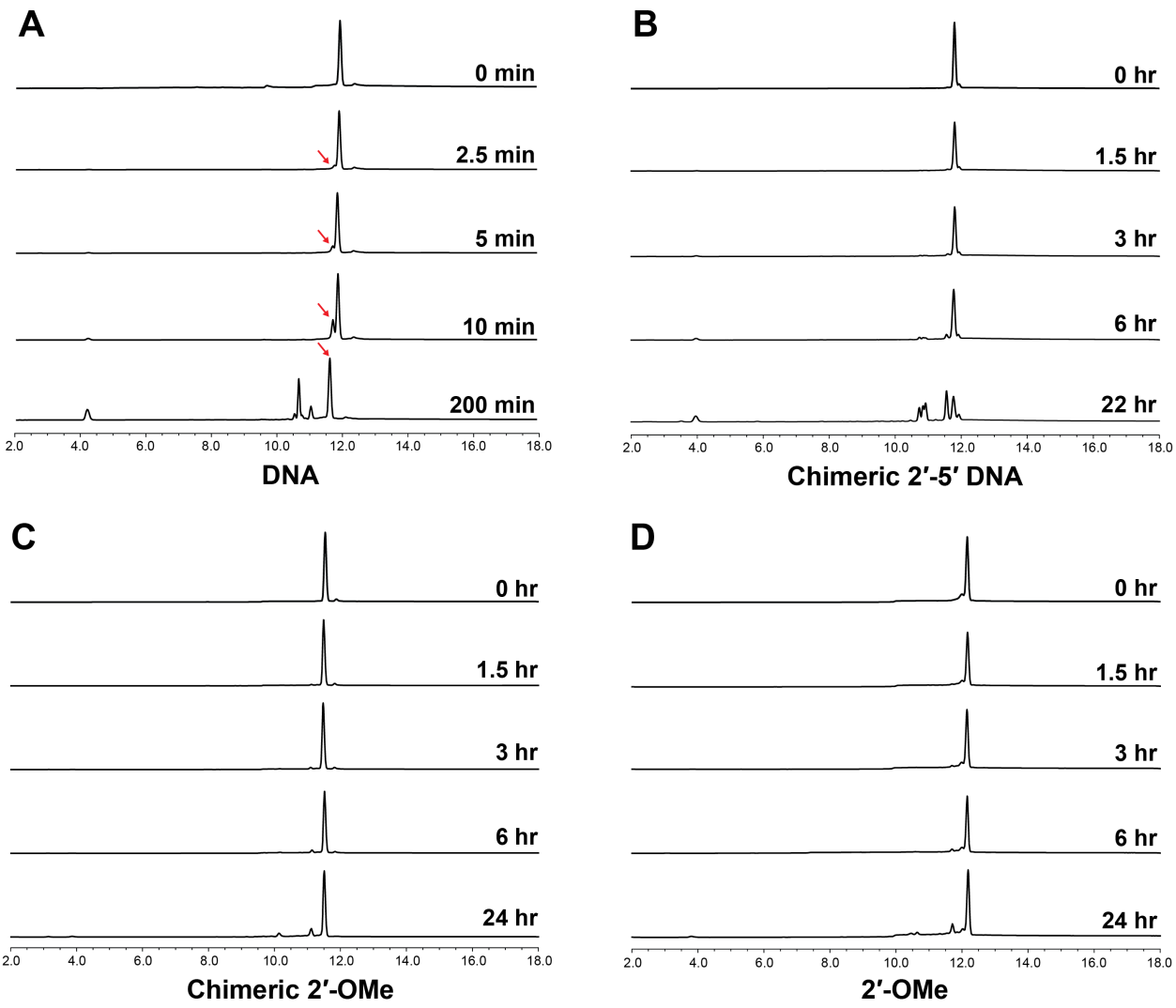

Supplementary Figure 3. Time-dependent HPLC analysis of acid-mediated cleavage of the asymmetric control strands. *Degradation profiles observed for the asymmetric T_6AT_9 sequence as the fully DNA strand (A), chimeric DNA strand with a central 2'-5' linked adenosine (B), chimeric DNA strand with a central 2'-OMe adenosine (C), and fully 2'-OMe strand (D). Reactions were performed using 40 μM oligonucleotide in 120 mM citrate phosphate buffer (pH 3.3) at 90°C. Red arrow indicates the depurinated product, as supported by MALDI-TOF data (Supplementary Figure 4).*

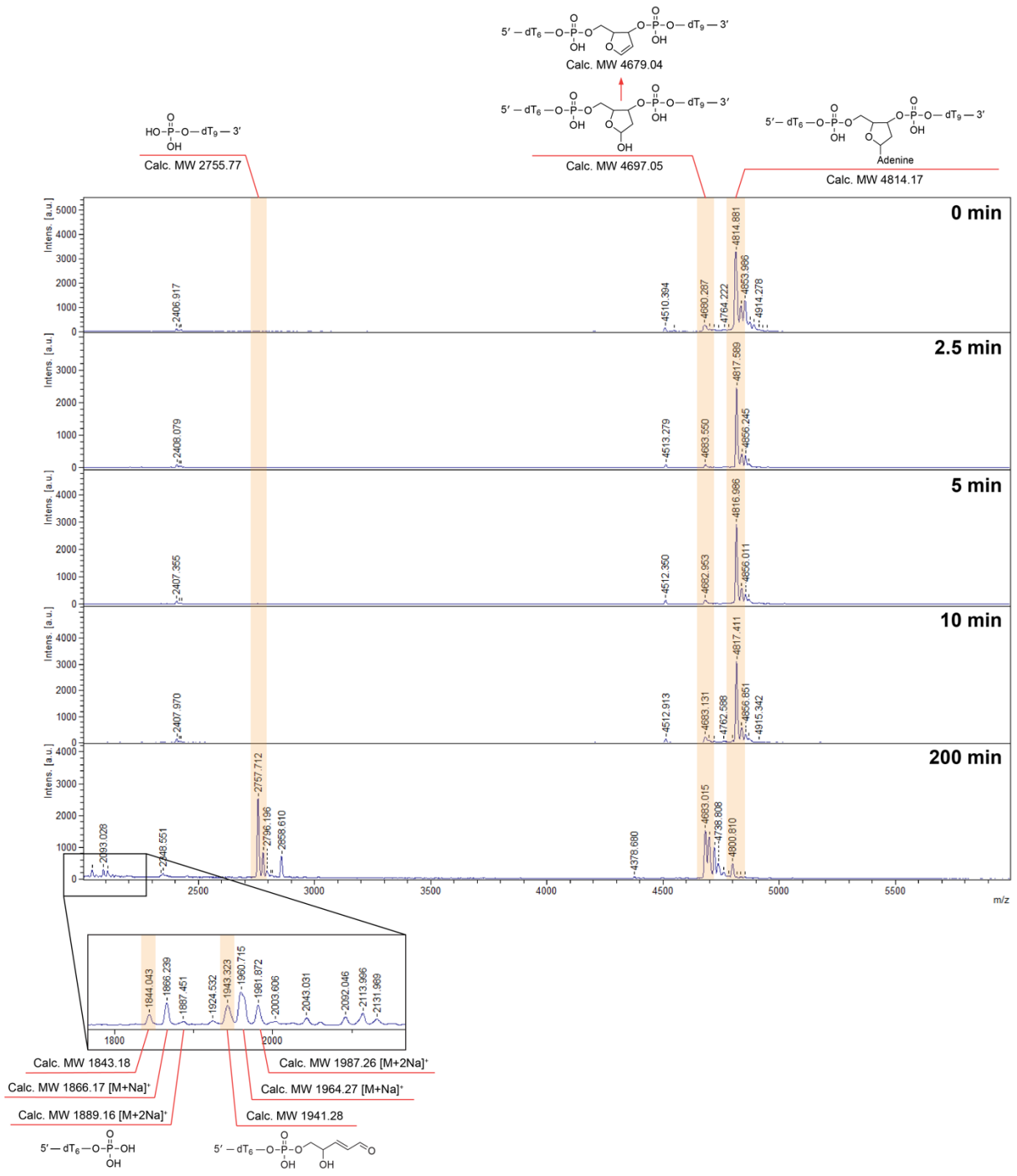

Supplementary Figure 4. Time-dependent mass spectrometry analysis of acid-mediated cleavage of DNA. *The DNA oligonucleotide consisting of the asymmetric sequence 5'-T_6AT_9-3' (40 µM) was incubated in 120 mM citrate phosphate buffer (pH 3.3) at 90°C. Cleavage products (MW 1941.28 and MW 2755.77) from deprotonation of the alpha-proton during β-elimination were observed by MALDI-TOF. The depurinated form of the oligonucleotide (MW 4697.05) is observed as the dehydrated form (MW 4679.04). Some masses were observed with one or more bound sodium ions.*

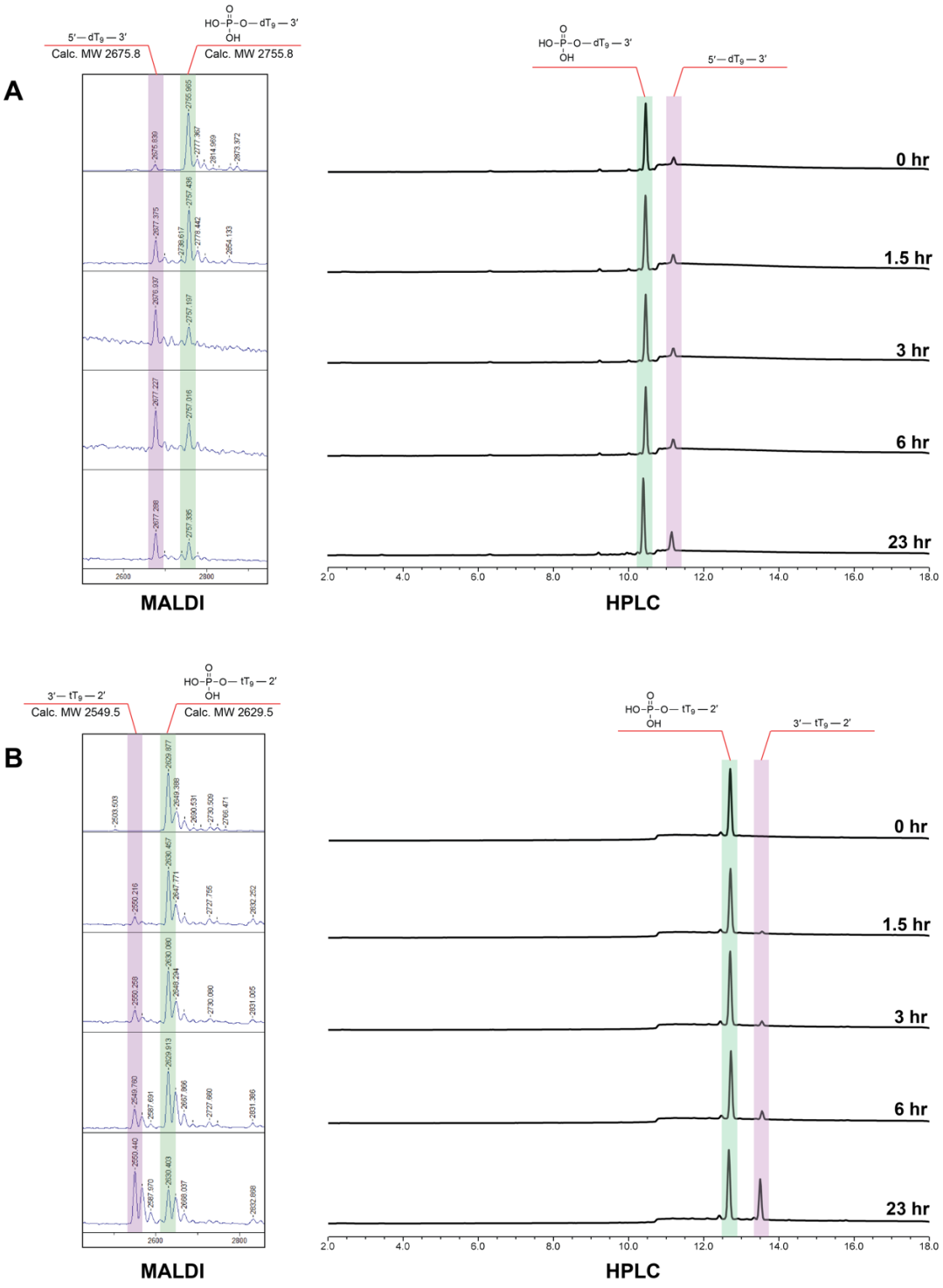

Supplementary Figure 5. Time-dependent HPLC and mass spectrometry analysis of acid hydrolysis of phosphorylated DNA and TNA. *The oligonucleotides (40 μM) were incubated in 120 mM citrate phosphate buffer (pH 3.3) at 90°C. Mass spectra and HPLC chromatograms show the acid hydrolysis profile of A) 5′-phos-dT₉-3′ and B) 3′-phos-tT₉-2′.*

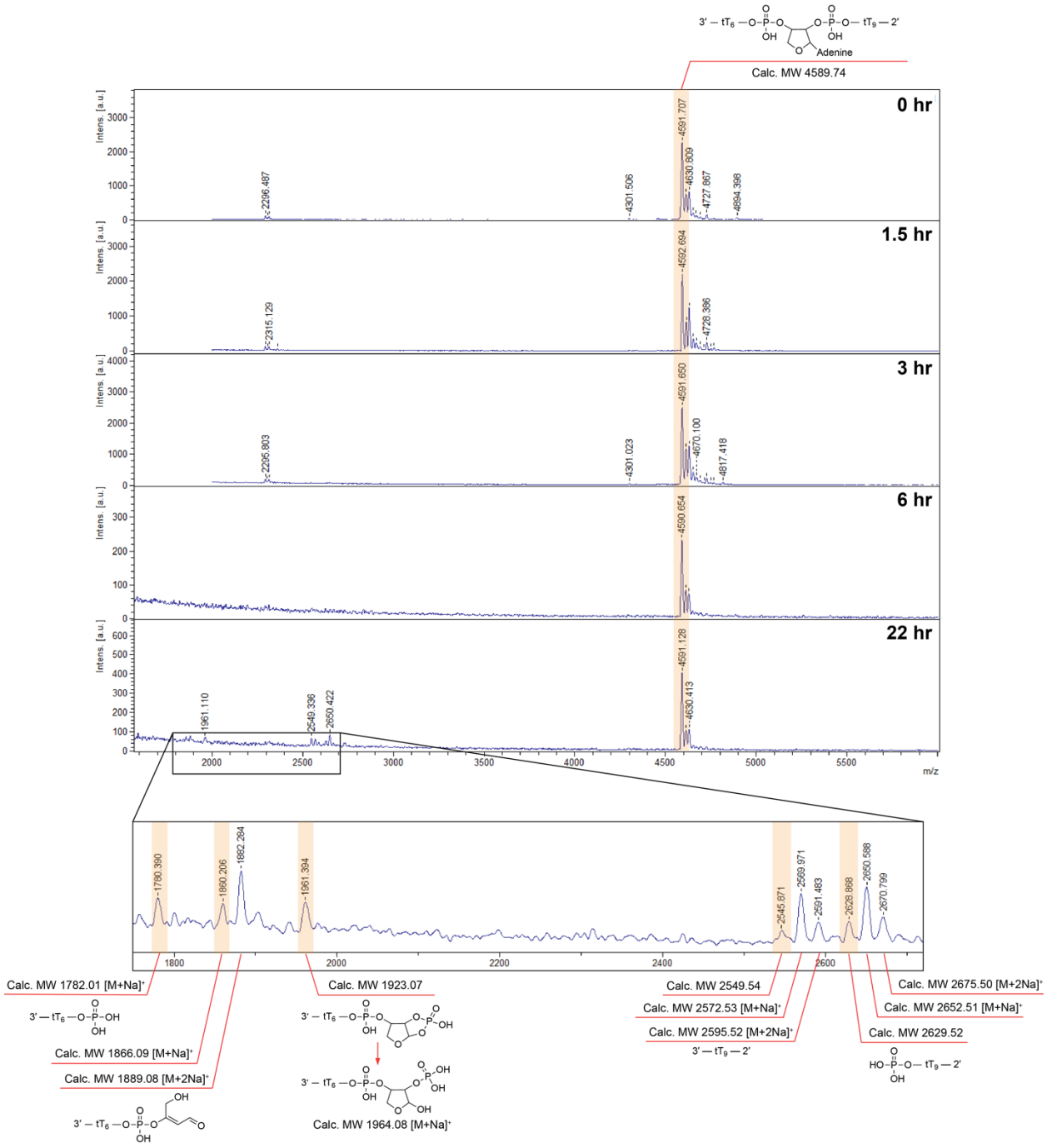

Supplementary Figure 6. Time-dependent mass spectrometry analysis of acid-mediated cleavage of TNA. *The TNA oligonucleotide consisting of the asymmetric sequence 3′-T_6AT_9-2′ (40 μM) was incubated in 120 mM citrate phosphate buffer (pH 3.3) at 90°C. Cleavage products (MW 1866.09 and MW 2629.52) from deprotonation of the beta-proton during β-elimination were observed by MALDI-TOF. The observed mass of 1961.4 indicate a competing minor pathway (see Supplementary Figure 7). Some masses were observed with one or more bound sodium ions.*

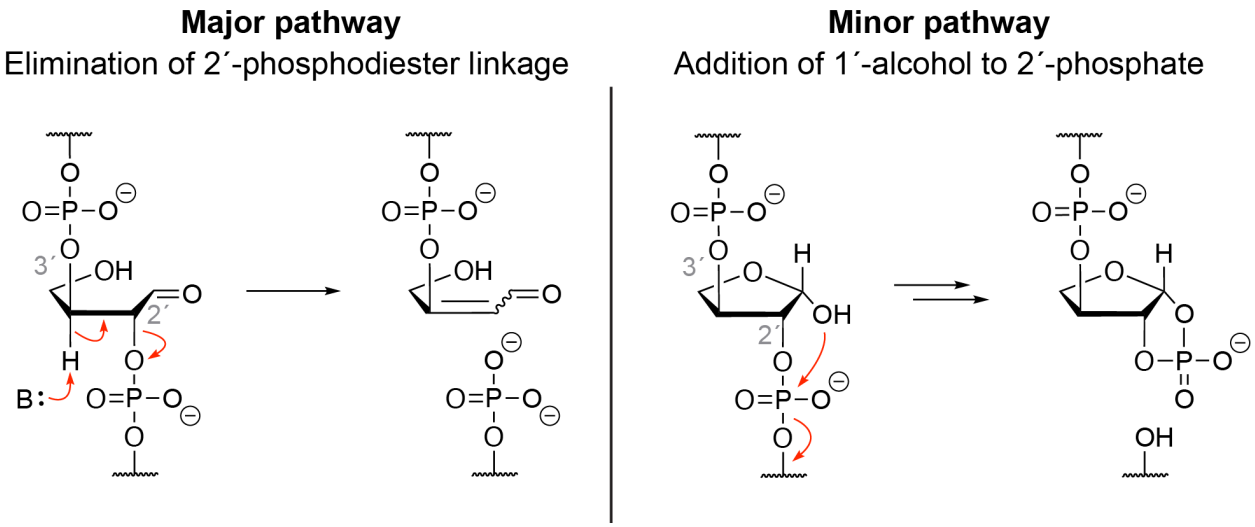

Supplementary Figure 7. Elimination pathways in acid-mediated TNA degradation. *Based on mass spectrometry, TNA does not follow the same elimination pathway as DNA, where the proton alpha to the aldehyde is deprotonated to eliminate the 3′-phosphodiester linkage. Instead, the proton beta to the aldehyde is primarily deprotonated to eliminate the 2′-phosphodiester linkage in TNA. Our mass spectrometry data is also consistent with a competing minor pathway where the a-anomeric hydroxyl group adds to the 2′-phosphate, resulting in a cyclic phosphate and 3′-tT₉-2′ without a 3´phosphate.*

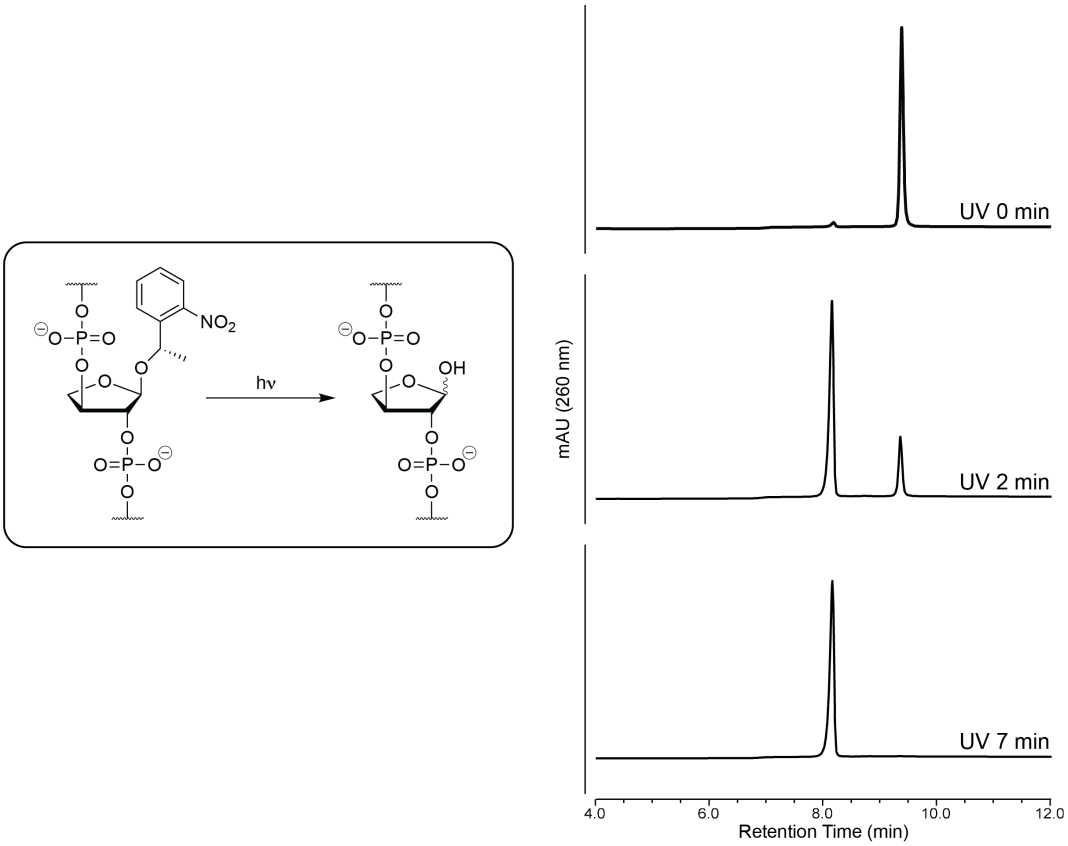

Supplementary Figure 8. HPLC analysis of NPE deprotection of asymmetric abasic TNA control strand via UV irradiation. *NPE deprotection was monitored over different time intervals by RP-HPLC with an increasing gradient of 5% to 37% buffer B over 14 min with a flow rate of 1.00 mL/min at a set temperature of 40°C. The peak of the NPE-protected TNA (R_t = ~9.5 min) decreased while the peak of the abasic TNA (R_t = ~8.0 min) increased. Complete conversion was observed at 7 minutes of UV irradiation as described in the Materials and Methods.*

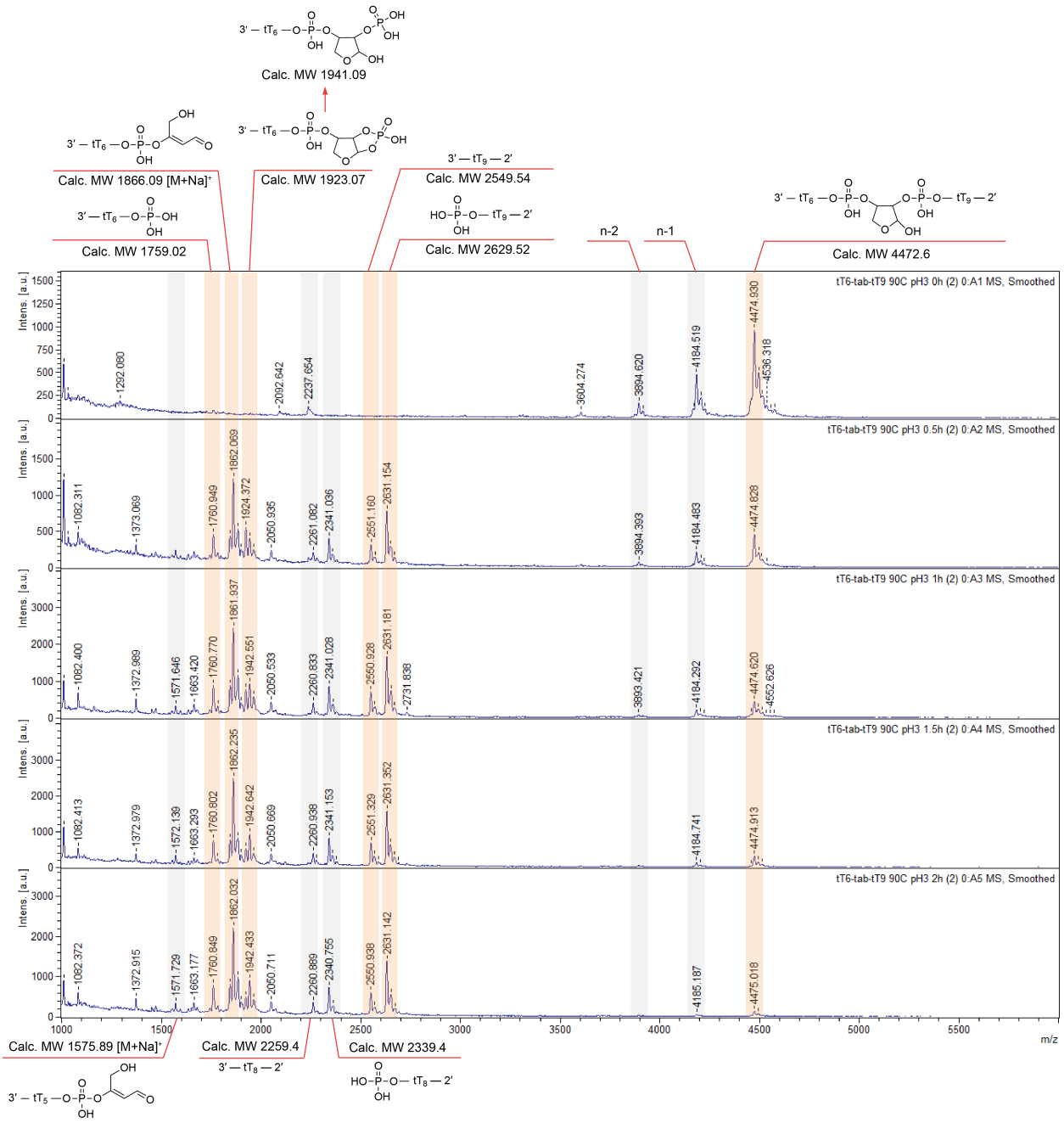

Supplementary Figure 9. Time-dependent mass spectrometry analysis of acid-mediated cleavage of TNA with an abasic residue. *The TNA oligonucleotide consisting of the asymmetric sequence 3'-T_6-tAP-T_9-2' (tAP are abasic TNA residues) (40 µM) was incubated in 120 mM citrate phosphate buffer (pH 3.3) at 90˚C. Cleavage products (MW 1866.09 and MW 2629.52) from deprotonation of the beta-proton during b-elimination were observed by MALDI-TOF. The observed mass of 1942.4 indicate a competing minor pathway (see Supplementary Figure 7). Light gray bars highlight masses associated with n-1 and n-2 products and their cleavage products. Some masses were observed with one or more bound sodium ions.*

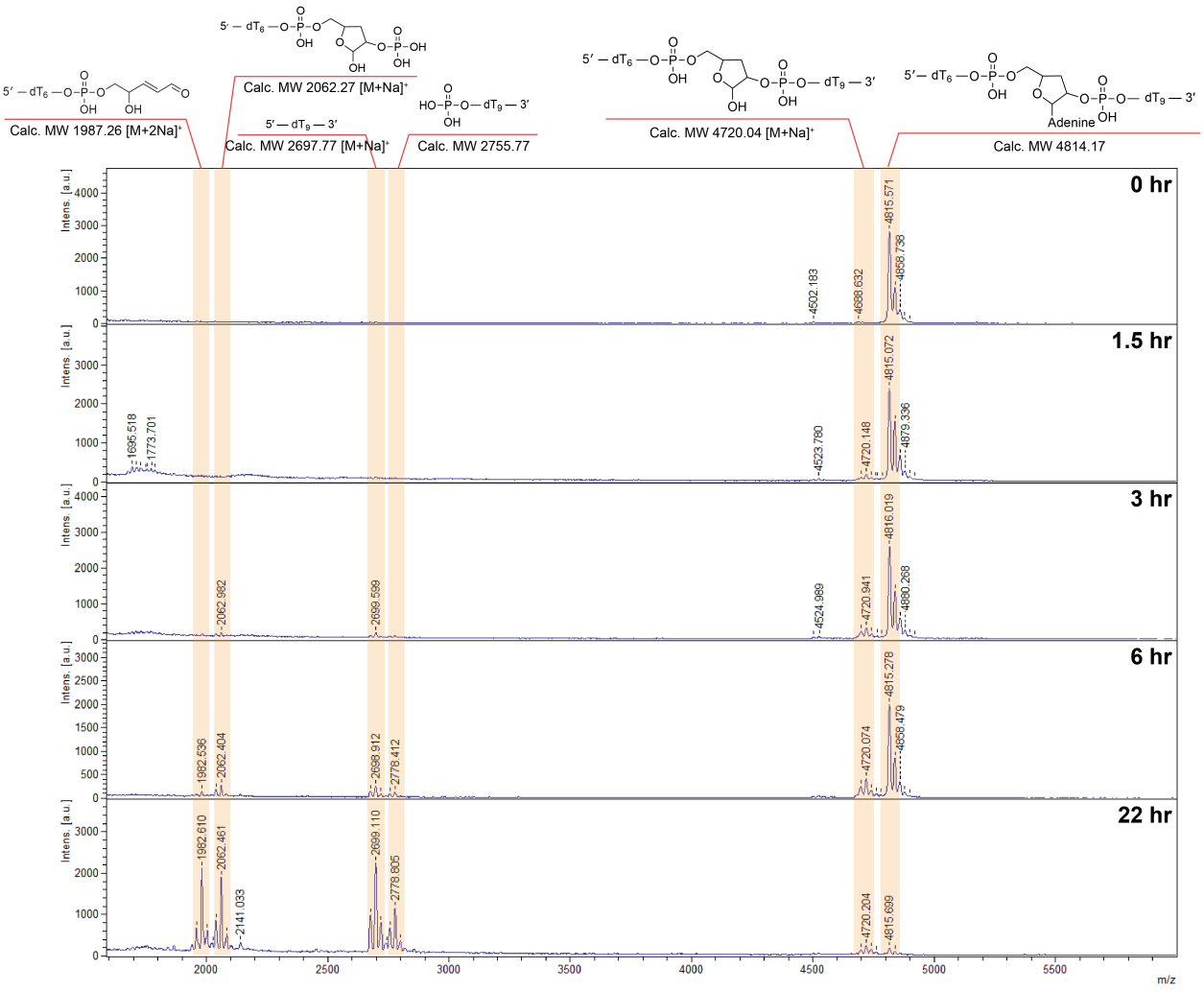

Supplementary Figure 10. Time-dependent mass spectrometry analysis of acid-mediated cleavage of a chimeric DNA with a central 2',5'-linked adenosine residue. *The DNA oligonucleotide consisting of the asymmetric sequence 5'-T_6AT_9-3' (<u>underlined</u> bases are 2',5'-linked DNA residues) (40 µM) was incubated in 120 mM citrate phosphate buffer (pH 3.3) at 90°C. Cleavage products (MW 1987.26 and MW 2755.77) from deprotonation of the beta-proton during b-elimination were observed by MALDI-TOF. Like in the asymmetric TNA strands, the observed mass of 2062.5 indicate a similar competing mechanism involving a cyclic phosphate (see Supplementary Figure 7). Some masses were observed with one or more bound sodium ions.*

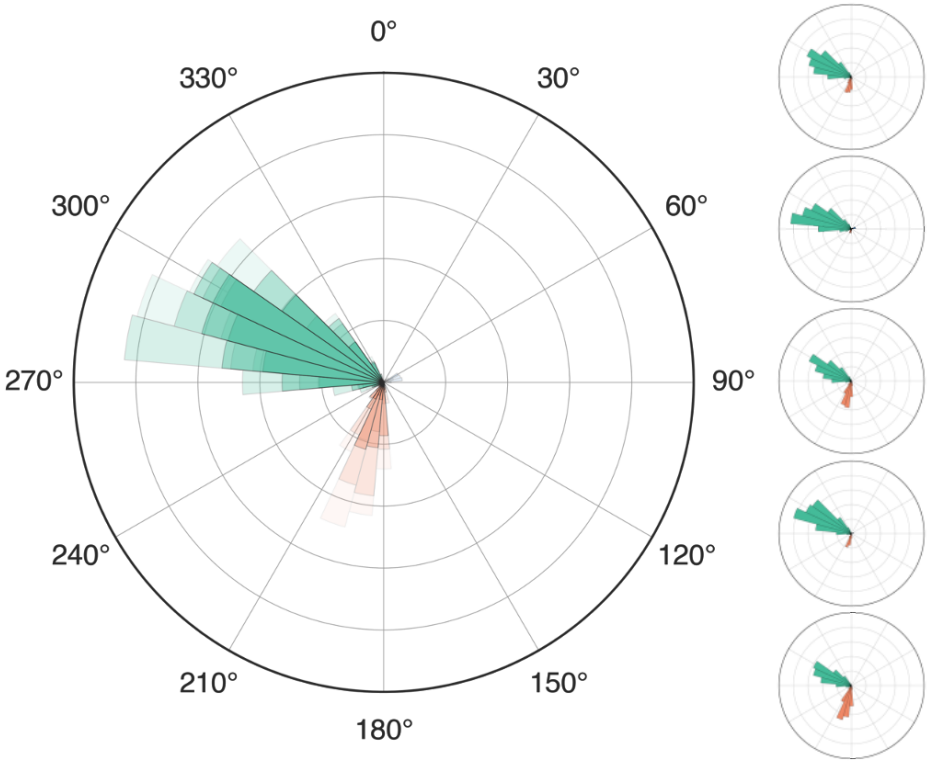

Supplementary Figure 11. Replication of conformational sampling. *Data presented in Figure 6 was reproduced in five replicates of the molecular dynamics simulation. Results are shown overlaid for all replicates and individually. The average frequency of a conformation nearing the antiperiplanar conformation is 22.9 ± 2.7% (orange peaks).*

Abasic TNA Phosphoramidite Synthesis.

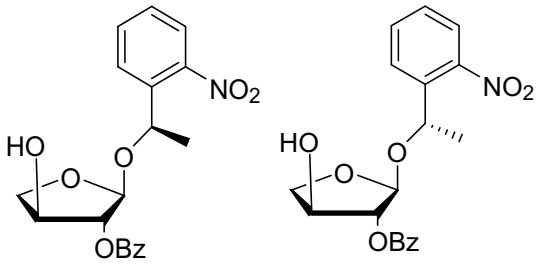

16a **16b**

(2*S*,3*R*,4*S*)-4-hydroxy-2-((*S*)-1-(2-nitrophenyl)ethoxy)tetrahydrofuran-3-yl benzoate (16a & 16b): To a solution of 1-(2-nitrophenyl)ethan-1-ol **14** (100 mg, 0.5982 mmol) and glycosyl donor **15** (362 mg, 0.7179 mmol) in dry CH_3CN, TMSOTf (37 µL, 0.2094 mmol) was added dropwise at -35°C under Argon atmosphere. The reaction mixture was stirred for 1 h (monitored by TLC) and quenched with 10 mL saturated aqueous $NaHCO_3$ solution. The aqueous layer was extracted with EtOAc (50 mL), and the organic layer was washed with brine, dried and concentrated under reduced pressure to give 200 mg inseparable mixture of diastereomers as crude product. To a solution of 200 mg of crude product in THF, 1M TBAF (0.36 mL, 0.3596 mmol) was added at 0°C. After stirring for 5 h at 0°C, the reaction mixture was concentrated, diluted with EtOAc (20mL). The organic layer was washed with water, dried and concentrated under reduced pressure to give crude. The crude was purified by column chromatography on silica gel (eluted with EtOAC:Hex = 1:4) to give separable diastereomers **16a** (60 mg, 0.1607 mmol, 27%) and **16b** (50 mg, 0.1339 mmol, 22%) in total 49% two-step yield.

16a: R_f 0.28 (EtOAc:Hex = 3:10); ^{1}H NMR (400 MHz, $CDCl_3$) δ 8.01-7.99 (m, 2H), 7.91 (d, *J* = 8.1 Hz, 1H), 7.82 (d, *J* = 7.9 Hz, 1H), 7.67-7.63 (m, 1H), 7.60-7.57 (m, 1H), 7.46-7.39 (m, 3H), 5.42 (q, *J* = 6.3 Hz, 1H), 5.38 (s, 1H), 5.18 (s, 1H), 4.32-4.29 (m, 1H), 4.10 (dd, *J* = 9.7, 6.3 Hz, 1H), 3.63 (dd, *J* = 9.7, 4.7 Hz, 1H), 3.11 (bs, 1H), 1.58 (d, *J* = 6.3 Hz, 3H); ^{13}C NMR (101 MHz, $CDCl_3$) δ 166.4, 147.3, 140.0, 133.7, 133.5, 129.9, 129.0, 128.6, 128.1, 128.0, 124.2, 105.3, 84.8, 75.6, 73.4, 71.3, 22.8; HRMS (ESI-TOF) calcd. for $C_{19}H_{19}NO_7Na$ $[M+Na]^+$ 396.1059, observed 396.1056.

16b: R_f 0.3 (EtOAc:Hex = 3:10); ^{1}H NMR (400 MHz, $CDCl_3$) δ 7.93-7.91 (m, 3H), 7.82-7.80 (d, *J* = 7.8 Hz, 1H), 7.68-7.65 (m, 1H), 7.57-7.53 (m, 1H), 7.44-7.38 (m, 3H), 5.52 (q, *J* = 6.2 Hz, 1H), 5.18 (s, 1H), 4.96 (s, 1H), 4.35 (s, 1H), 4.36-4.31 (m, 1H), 4.08-4.03 (m, 1H), 3.21 (bs, 1H), 1.59 (d, *J* = 6.3 Hz, 3H); ^{13}C NMR (101 MHz, $CDCl_3$) δ 166.2, 148.5, 138.4, 133.8, 133.6, 129.8, 129.0, 128.5, 128.4, 128.0, 124.5, 103.5, 84.1, 75.4, 73.9, 69.6, 24.1; HRMS (ESI-TOF) calcd. for $C_{19}H_{19}NO_7Na$ $[M+Na]^+$ 396.1059, observed 396.1042.

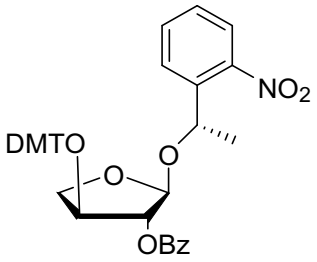

(2*S*,3*R*,4*S*)-4-(bis(4-methoxyphenyl)(phenyl)methoxy)-2-((*S*)-1-(2-nitrophenyl)ethoxy) tetrahydrofuran-3-yl benzoate (17): To a solution of **16b** (40 mg, 0.1071 mmol) in CH_2Cl_2 (1.5 mL), collidine (42 µL, 0.3214 mmol) and DMTCl (54 mg, 0.1607 mmol) were added followed by the addition of $AgNO_3$ (9 mg, 0.0535 mmol). The reaction mixture was stirred at 37°C for 5 h, quenched with water and diluted with CH_2Cl_2. The organic layer was separated, dried and concentrated under reduced pressure to give crude. The crude was purified by column chromatography (on TEA-deactivated silica, eluted with 1.5:10 EtOAc:Hex) to give product **17** (40 mg, 0.0592 mmol, 55%) as colorless oil. R_f 0.7 (EtOAc:Hex = 3:10); ^{1}H NMR (400 MHz, $CDCl_3$) δ 7.98 (d, *J* = 7.8 Hz, 1H), 7.90-7.85 (m, 3H), 7.63 (t, *J* = 6.3 Hz, 1 H), 7.55-7.48 (m, 3H), 7.40-7.33 (m, 7H), 7.27-7.23 (m, 2H), 7.20-7.16 (m, 1H), 6.78-6.73 (m, 4H), 5.43 (q, *J* = 6.3 Hz, 1H), 5.12 (d, *J* = 1.4 Hz, 1H), 4.59 (s, 1H), 4.38-4.35 (m, 1H), 3.73 (dd, *J* = 9.1, 7.0 Hz, 1H), 3.69 (s, 3H), 3.66 (s, 3H), 3.55 (dd, *J* = 9.1, 7.0 Hz, 1H), 1.62 (d, *J* = 6.3 Hz, 3H); ^{13}C NMR (101 MHz, $CDCl_3$) δ 165.3, 158.7, 158.7, 148.3, 145.2, 139.1, 136.2, 136.1, 133.9, 133.2, 130.3, 130.2, 129.8, 129.4, 128.5, 128.3, 128.1, 128.0, 128.0, 127.0, 124.3, 113.4, 113.3, 103.4, 87.2, 83.8, 77.3, 71.1, 68.7, 55.1, 55.1, 24.1; HRMS (ESI-TOF) calcd. for $C_{40}H_{37}NO_9Na$ $[M+Na]^+$ 698.2366, observed 698.2372.

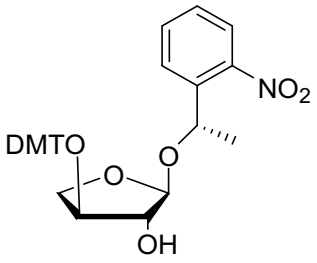

(2*S*,3*R*,4*S*)-4-(bis(4-methoxyphenyl)(phenyl)methoxy)-2-((*S*)-1-(2-nitrophenyl)ethoxy) tetrahydrofuran-3-ol (18): A solution of **17** (40 mg, 0.0592 mmol) in 3 mL of THF:MeOH:H_2O (0.012 M, 3.5:3:1) was cooled to 0°C and 0.90 mL (0.9058 mmol) of 1M NaOH was added to it. After stirring for 5 h at 0°C, 54 mg (1.0063 mmol) of solid NH_4Cl was added and stirring was continued for 20 min. The reaction mixture was evaporated to remove solvents and the crude was purified by column chromatography (on TEA-deactivated silica, eluted with 2:10 EtOAc:Hex) to give product **18** (25 mg, 0.0437 mmol, 73% yield) as colorless oil. R_f 0.4 (EtOAc:Hex = 3:10); ^{1}H NMR (400 MHz, $CDCl_3$) 7.86 (d, *J* = 8.1 Hz, 1H), 7.75 (d, *J* = 7.9 Hz, 1H), 7.61-7.59 (m, 1 H), 7.50-7.48 (m, 2H), 7.40-7.36 (m, 5H), 7.32-7.29 (m, 2H), 7.25-7.23 (m, 1H), 6.86-6.83 (m, 4H), 5.33 (q, *J* = 6.3 Hz, 1H), 4.50 (s, 1H), 4.00-3.97 (m, 1H), 3.88 (m, 1H), 3.79 (s, 6H), 3.69-3.60 (m, 2H), 1.59 (d, *J* = 6.3 Hz, 3H); ^{13}C NMR (101 MHz, $CDCl_3$) δ ; 158.8, 148.5, 145.4, 139.1, 136.7, 136.6, 133.5, 130.2, 128.3, 128.2, 128.1, 128.0, 127.1, 124.3, 113.3, 105.5, 86.7, 82.2, 80.0, 71.5, 69.1, 55.3, 24.0; HRMS (ESI-TOF) calcd. for $C_{33}H_{33}NO_8Na$ $[M+Na]^+$ 594.2104, observed 594.2093.

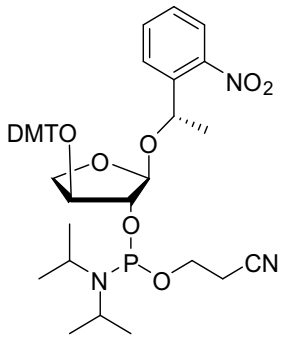

(2*S*,3R,4*S*)-4-(bis(4-methoxyphenyl)(phenyl)methoxy)-2-((*S*)-1-(2-nitrophenyl)ethoxy) tetrahydrofuran-3-yl (2-cyanoethyl) diisopropylphosphoramidite (19): To a suspension of **18** (60 mg, 0.1049 mmol) and DMAP (2.5 mg, 0.0210 mmol) in CH_2Cl_2 (10 mL) was added *N*,*N*-diisopropylethylamine (DIPEA) (27 µL, 0.1574 mmol), followed by the addition of 2-cyanoethyl-*N*,*N*-diisopropylchlorophosphoramidite (35 µL, 0.1574 mmol). After stirring for 40 minutes at room temperature, the solution was diluted with CH_2Cl_2 (20 mL) and washed with saturated aqueous $NaHCO_3$ (40 mL). The organic layer was washed with brine, dried and concentrated under reduced pressure to give crude. The crude was purified by column chromatography on silica gel (eluted with 1.5:10 EtOAc:Hex) to afford product **19** (77 mg, 0.1010 mmol, 96%) as white solid. TLC (EtOAc:Hex, 3:10). R_f 0.8 (EtOAc:Hex = 3:10); ^{31}P NMR (162 MHz, CD3CN) δ 149.3, 149.0; HRMS (ESI-TOF) calcd. for $C_{42}H_{50}N_3O_9PNa$ $[M+Na]^+$ 794.3182, observed 794.3160.

Compound Characterization.

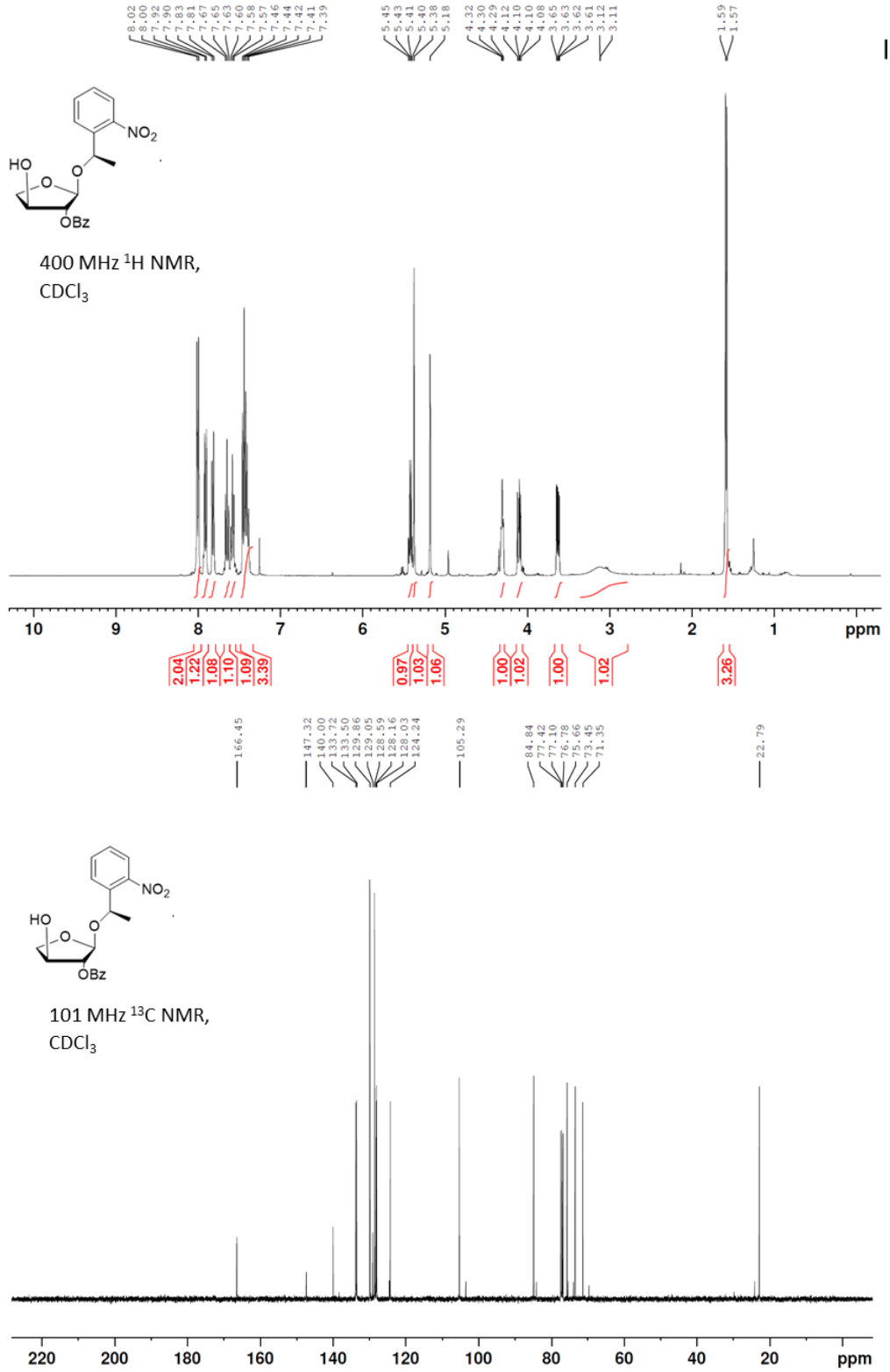

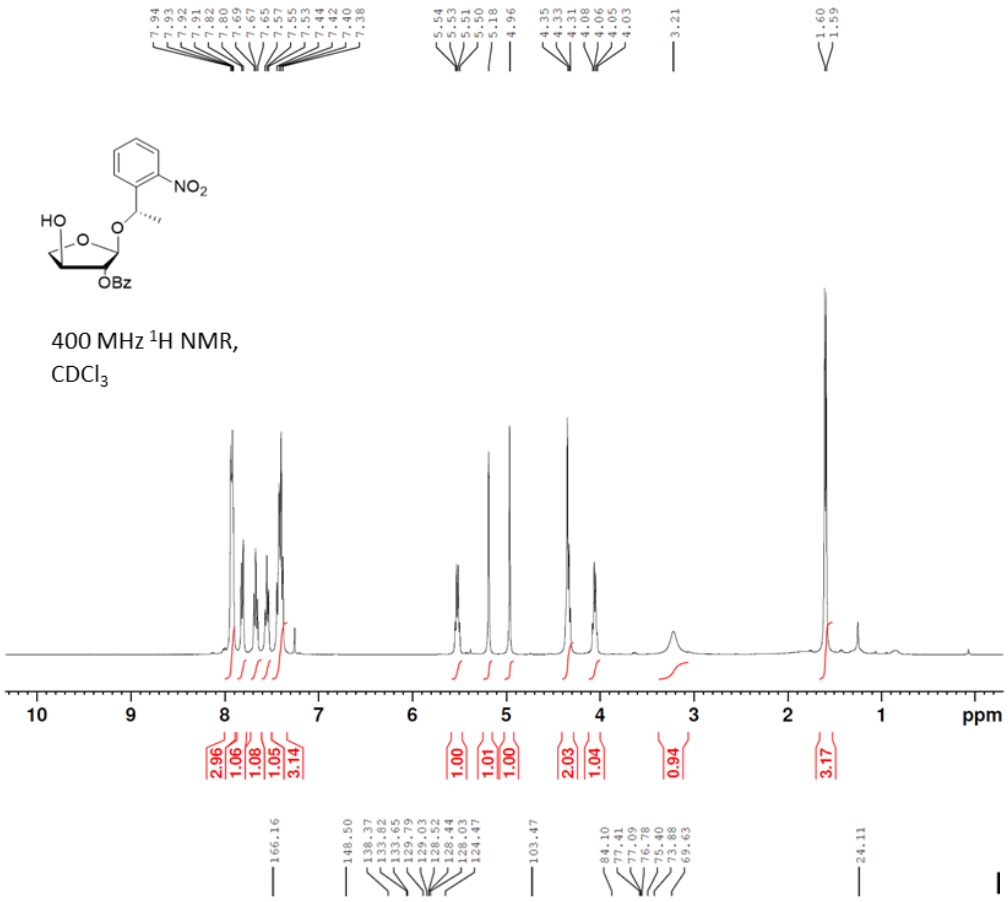
7.94
7.93
7.92
7.91
7.82
7.80
7.69
7.67
7.65
7.57
7.55
7.53
7.44
7.42
7.40
7.38
5.54
5.53
5.51
5.50
5.18
4.96
4.35
4.33
4.31
4.08
4.06
4.05
4.03
3.21
1.60
1.59
NO2
HO
O
O
OBz
400 MHz 1H NMR,
CDCl3
10
9
8
7
6
5
4
3
2
1
ppm
2.96
1.06
1.08
1.05
3.14
1.00
1.01
1.00
2.03
1.04
0.94
3.17

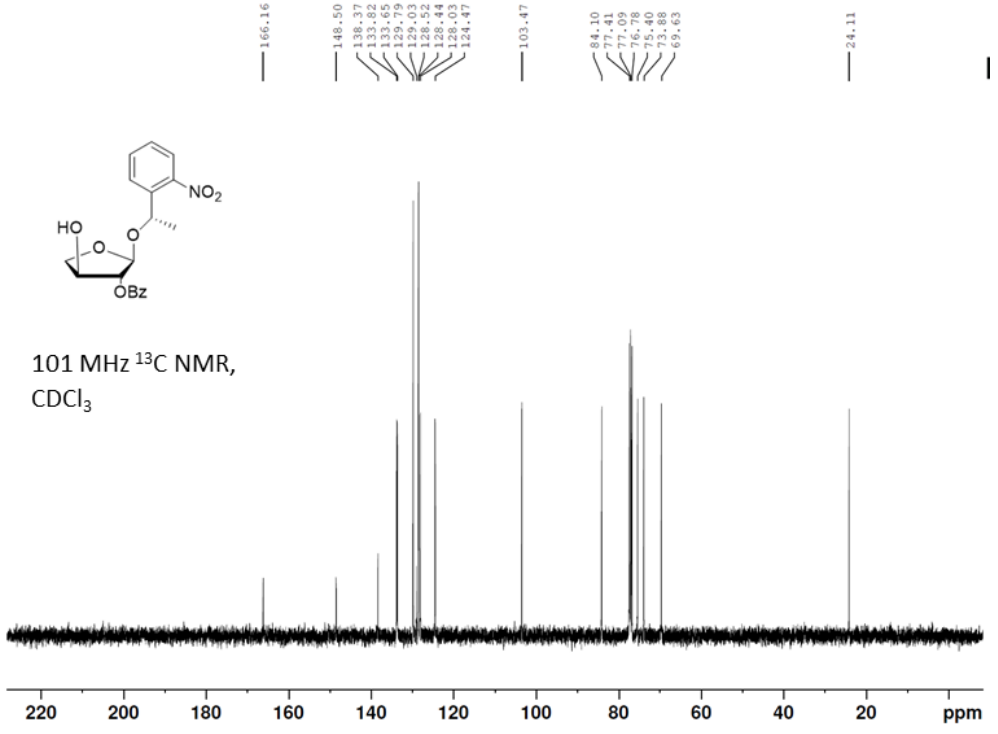
166.16
148.50
138.37
133.82
133.65
129.79
129.03
128.52
128.44
124.03
124.47
103.47
84.10
77.41
77.09
76.78
75.60
73.88
69.63
24.11
NO2
HO
O
O
OBz
101 MHz 13C NMR,
CDCl3
220
200
180
160
140
120
100
80
60
40
20
ppm

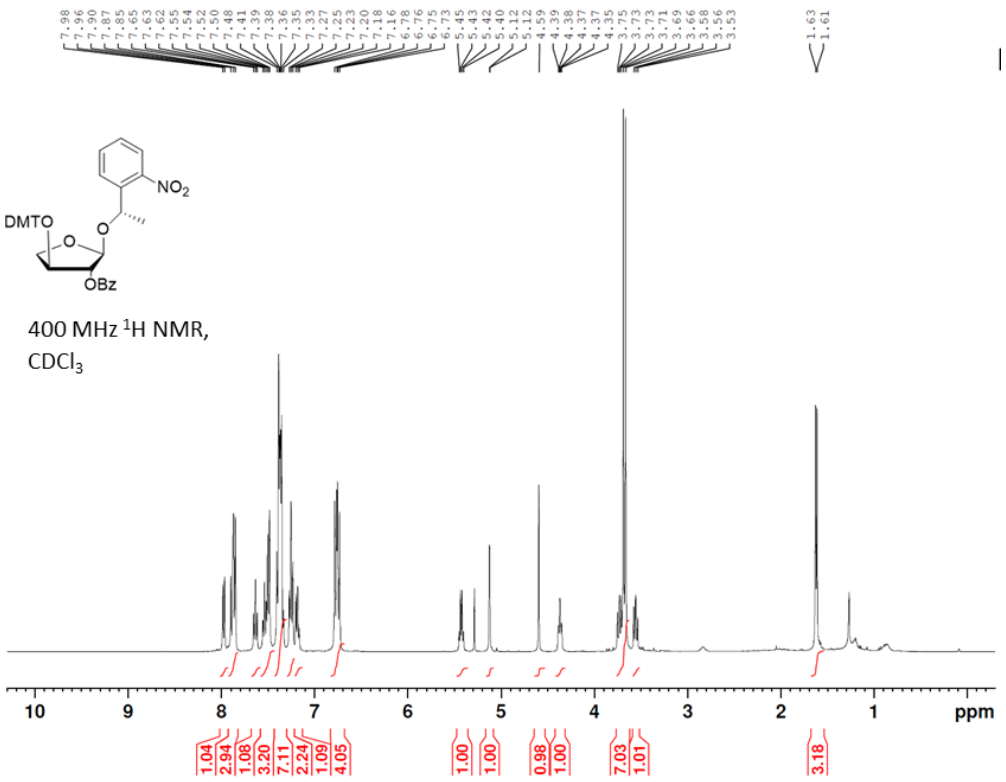
DMTO
NO2
OBz
400 MHz 1H NMR,
CDCl3
10
9
8
7
6
5
4
3
2
1
ppm

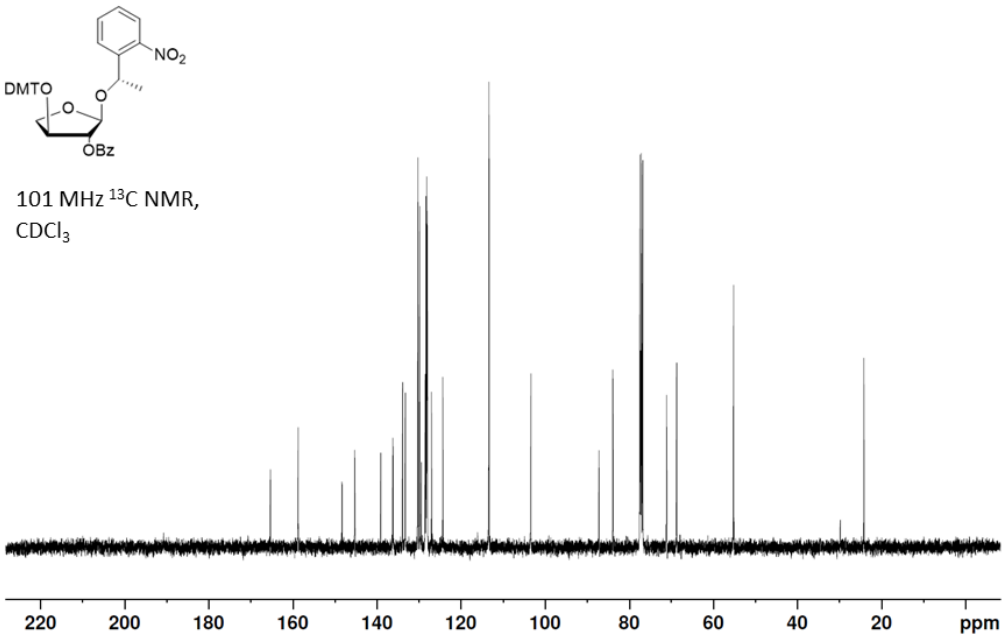
DMTO
NO2
OBz
101 MHz 13C NMR,
CDCl3
220
200
180
160
140
120
100
80
60
40
20
ppm

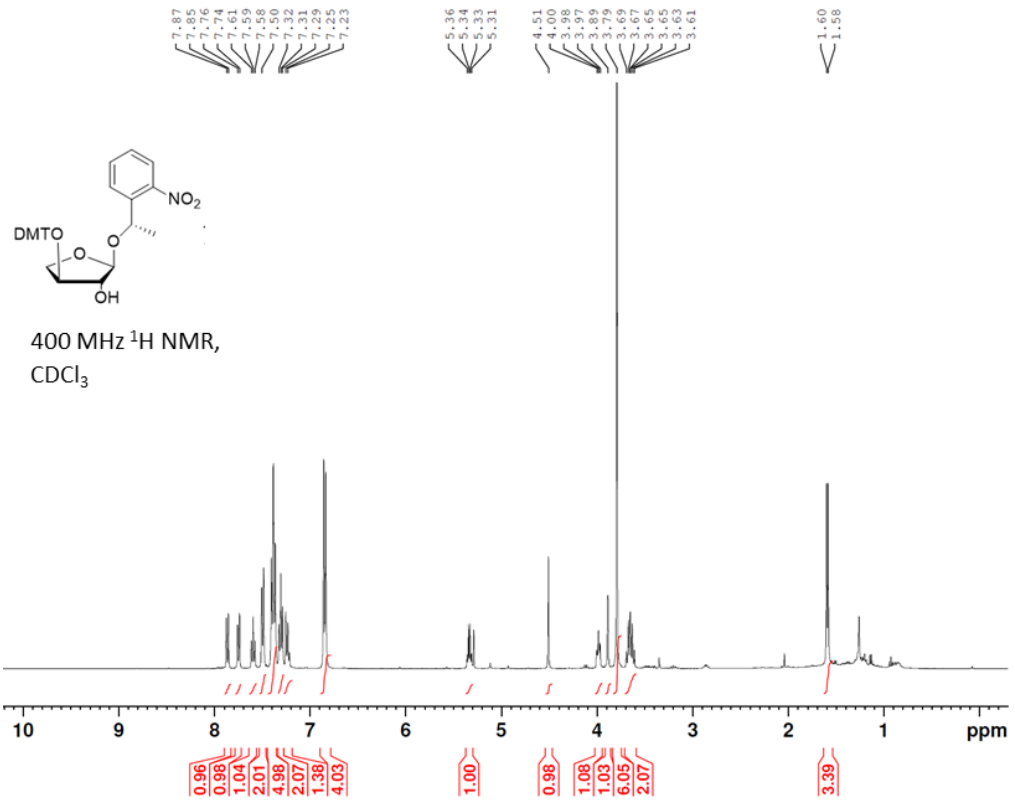

400 MHz ^{1}H NMR,
$CDCl_3$

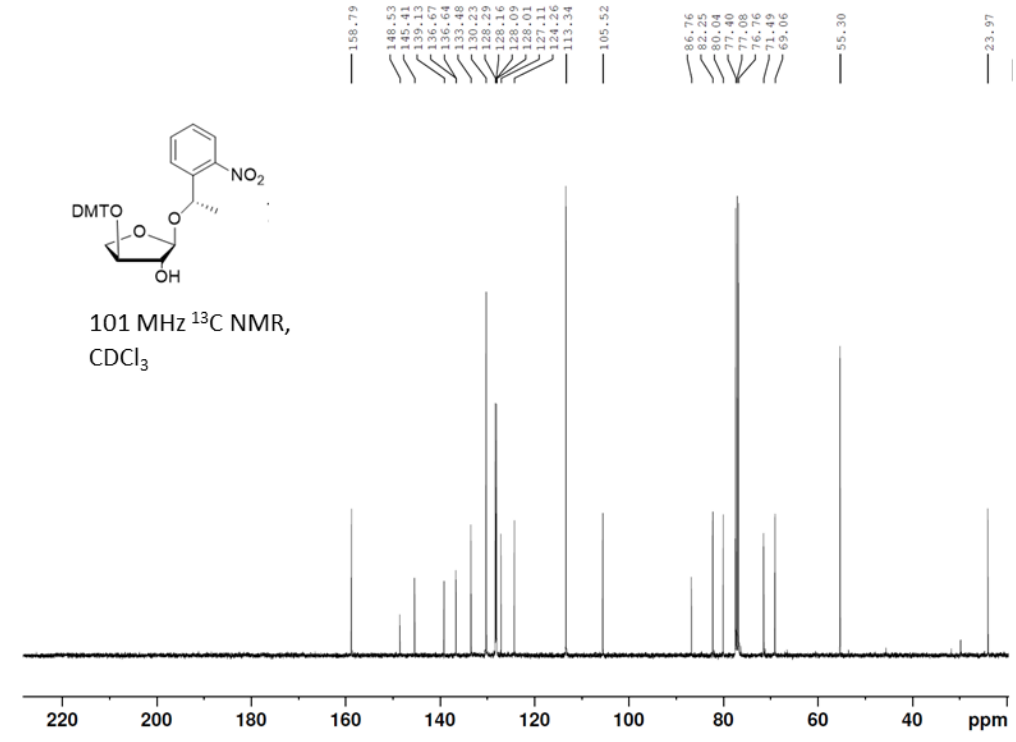

101 MHz ^{13}C NMR,
$CDCl_3$

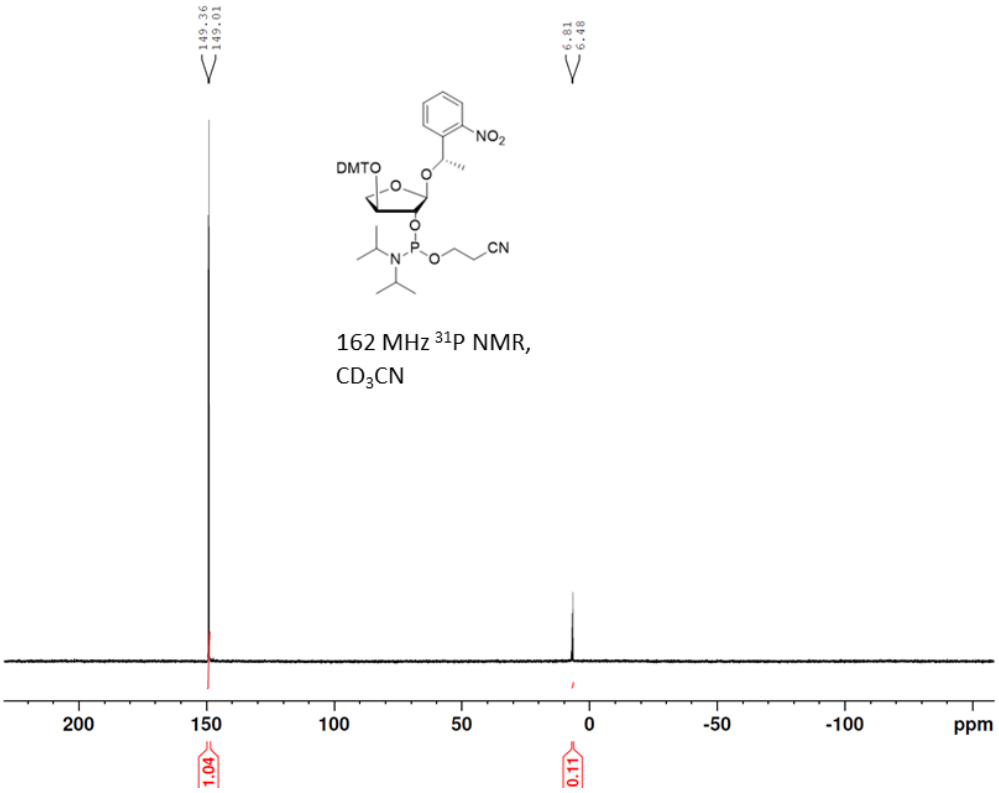

162 MHz ^{31}P NMR,
CD_3CN

APPENDIX B: Supplementary Data for Chapter 2

Supplementary Table 1. Dz46 variants used in the TNA walk.

DNAzyme ID	Sequence (5' → 3'; IDT nomenclature)	Calculated Mass (Da)	Observed Mass (Da)	Δ Mass (Da)
tA0	+TmAmCmGCCA**tA***GGCTAGmCmUACAAC*/i2MOErG/AAGCmUmCmC+A	9514.17	9518.65	4.48
tG1	+TmAmCmGCCAA***tG**GCTAGmCmUACAAC*/i2MOErG/AAGCmUmCmC+A	9514.17	9520.00	5.83
tG2	+TmAmCmGCCAA*G**tG**CTAGmCmUACAAC*/i2MOErG/AAGCmUmCmC+A	9514.17	9521.91	7.74
tC3	+TmAmCmGCCAA*GG**tC**TAGmCmUACAAC*/i2MOErG/AAGCmUmCmC+A	9514.17	9520.30	6.13
tT4	+TmAmCmGCCAA*GGC**tT**AGmCmUACAAC*/i2MOErG/AAGCmUmCmC+A	9514.17	9520.69	6.52
tA5	+TmAmCmGCCAA*GGCT**tA**GmCmUACAAC*/i2MOErG/AAGCmUmCmC+A	9514.17	9522.65	8.48
tG6	+TmAmCmGCCAA*GGCTA**tG**mCmUACAAC*/i2MOErG/AAGCmUmCmC+A	9514.17	9522.44	8.27
tC7	+TmAmCmGCCAA*GGCTAG**tC**mUACAAC*/i2MOErG/AAGCmUmCmC+A	9484.14	9492.35	8.21
tT8	+TmAmCmGCCAA*GGCTAGmC**tT**ACAAC*/i2MOErG/AAGCmUmCmC+A	9498.16	9506.26	8.10
tA9	+TmAmCmGCCAA*GGCTAGmCmU**tA**CAAC*/i2MOErG/AAGCmUmCmC+A	9514.17	9519.74	5.57
tC10	+TmAmCmGCCAA*GGCTAGmCmUA**tC**AAC*/i2MOErG/AAGCmUmCmC+A	9514.17	9521.08	6.91
tA11	+TmAmCmGCCAA*GGCTAGmCmUAC**tA**AC*/i2MOErG/AAGCmUmCmC+A	9514.17	9521.48	7.31
tA12	+TmAmCmGCCAA*GGCTAGmCmUACA**tA**C*/i2MOErG/AAGCmUmCmC+A	9514.17	9521.23	7.06
tC13	+TmAmCmGCCAA*GGCTAGmCmUACAA**tC***/i2MOErG/AAGCmUmCmC+A	9514.17	9521.05	6.88
tG14	+TmAmCmGCCAA*GGCTAGmCmUACAAC***tG** AAGCmUmCmC+A	9440.09	9446.36	6.27
tA15	+TmAmCmGCCAA*GGCTAGmCmUACAAC*/i2MOErG/**tA**AGCmUmCmC+A	9514.17	9520.45	6.28
tA16	+TmAmCmGCCAA*GGCTAGmCmUACAAC*/i2MOErG/A**tA**GCmUmCmC+A	9514.17	9521.41	7.24

TNA (t); LNA (+); 2'-O-methoxyribonucleic acid (m); phosphorothioate linkage (*); 2'-O- methoxyethylribonucleic acid (/i2MOEr/).

Supplementary Table 2. Dz46 variants with chemical modification at the terminal and internal positions.

DNAzyme ID	Sequence (5' → 3' or 3' → 2'; IDT nomenclature)	Calculated Mass (Da)	Observed Mass (Da)	Δ Mass (Da)
Dz46+	+TmAmCmG**tCtC**AA*GGCTAGmCmUACAAC*/i2MOErG/AAGCmUmCmC+A	9500.15	9502.51	2.36
NS580	***t*T**mAmCmGCCAA*GGCTAGmCmUACAAC*/i2MOErG/AAGCmUmCmC**tA**	9444.13	9450.83	6.70
NS580+	***t*T**mAmCmG**tCtC**AA*GGCTAGmCmUACAAC*/i2MOErG/AAGCmUmCmC**tA**	9416.09	9424.63	8.54

TNA (t); LNA (+); 2'-O-methoxyribonucleic acid (m); phosphorothioate linkage (*); 2'-O- methoxyethylribonucleic acid (/i2MOEr/).

Supplementary Table 3. DNAzymes used in KRAS G12V knockdown experiments.

DNAzyme ID	Sequence (5' → 3'; IDT nomenclature)	Calculated Mass (Da)	Observed Mass (Da)	Δ Mass (Da)
Dz46	+TmAmCmGCCAA*GGCTAGmCmUACAAC*/i2MOErG/AAGCmUmCmC+A	9528.23	9533.33	5.1
tC3 (Dz46 ver.)	+TmAmCmGCCAA*GG**tC**TAGmCmUACAAC*/i2MOErG/AAGCmUmCmC+A	9514.17	9520.30	6.13
tC3+ (Dz46 ver.)	+TmAmCmG**tCtC**AA*GG**tC**TAGmCmUACAAC*/i2MOErG/AAGCmUmCmC+A	9486.13	9493.73	7.60
Inactive Dz46	+TmAmCmGCCAA*GGCCATmCmUACAAC*/i2MOErG/A AGCmUmCmC+A	9488.20	9494.35	6.15

TNA (t); LNA (+); 2'-O-methoxyribonucleic acid (m); phosphorothioate linkage (*); 2'-O- methoxyethylribonucleic acid (/i2MOEr/).

Supplementary Table 4. DNAzymes used in PCSK9 knockdown experiments.

DNAzyme ID	Sequence (5' → 3'; IDT nomenclature)	Calculated Mass (Da)	Observed Mass (Da)	Δ Mass (Da)
TNM243	+GmCmAmCGGAA*GGCTAGmCmUACAAC*/i2 MOErG/AAAGmAmGmC+T	9671.36	9675.10	3.74
tC3 (TNM243 ver.)	+GmCmAmCGGAA*GG**tC**TAGmCmUACAAC*/i2 MOErG/AAAGmAmGmC+T	9657.34	9660.76	3.42
tC3+ (TNM243 ver.)	+GmCmAmC**tGtG**AA*GG**tC**TAGmCmUACAAC*/i2 MOErG/AAAGmAmGmC+T	9629.30	9632.71	3.41
Inactive TNM243	+GmCmAmCGGAA*GGCCATmCmUACAAC*/i2 MOErG/AAAGmAmGmC+T	9631.33	9634.29	2.96

TNA (t); LNA (+); 2'-O-methoxyribonucleic acid (m); phosphorothioate linkage (*); 2'-O- methoxyethylribonucleic acid (/i2MOEr/).

Supplementary Table 5. DNAzymes used in GATA3 knockdown experiments.

DNAzyme ID	Sequence (5' → 3'; IDT nomenclature)	Calculated Mass (Da)	Observed Mass (Da)	Δ Mass (Da)
KN155	+AmAmCmGGTAA*GGCTAGmCmUACAAC*/i2 MOErG/AACTmGmAmU+T	9622.33	9625.98	3.65
tC3 (KN155 ver.)	+AmAmCmGGTAA*GG**tC**TAGmCmUACAAC*/i2 MOErG/AACTmGmAmU+T	9608.31	9613.88	5.57
tC3+ (KN155 ver.)	+AmAmCmG**tGtT**AA*GG**tC**TAGmCmUACAAC*/i2 MOErG/AACTmGmAmU+T	9580.26	9583.11	2.85
Inactive KN155	+AmAmCmGGTAA*GGCCATmCmUACAAC*/i2 MOErG/AACTmGmAmU+T	9582.30	9587.37	5.07

TNA (t); LNA (+); 2'-O-methoxyribonucleic acid (m); phosphorothioate linkage (*); 2'-O- methoxyethylribonucleic acid (/i2MOEr/).

Supplementary Table 6. Control oligonucleotides.

DNAzyme ID	Sequence (5' → 3'; IDT nomenclature)	Calculated Mass (Da)	Observed Mass (Da)	Δ Mass (Da)
Non-binder (used in RNase H1 assays)	+AmGmGmUGACA*GGCTAGmCmUACAAC*/i2MOErG/A TATmAmGmA+A	9671.38	9675.84	4.46
Non-binder (used in cellular assays)	+AmCmCmGCGCA*GGCTAGmCmUACAAC*/i2MOErG/A CCGmUmUmU+G	9523.17	9528.21	5.04
ASO	GCCTACGCCAACAGCTCCAACT	-	-	-

TNA (t); LNA (+); 2'-O-methoxyribonucleic acid (m); phosphorothioate linkage (*); 2'-O- methoxyethylribonucleic acid (/i2MOEr/).

Supplementary Table 7. RNA substrates.

RNA substrates	Sequence (5' → 3'; IDT nomenclature)
16 nt –G12V KRAS (NCBI: NM_ 004985, human GTPase KRAS mRNA variant b, (positions 217-232: G225U mutation, codon 12 GGU to GUU)	/5Cy5/rUrGrGrArGrCrUrGrUrUrGrGrCrGrUrA
60 nt –G12V KRAS (NCBI: NM_ 004985, human GTPase KRAS mRNA variant b, (positions 195-254: G225U mutation, codon 12 GGU to GUU)	/5Cy5/rCrUrGrArArUrArUrArArArCrUrUrGrU rGrGrU-rArGrUrUrGrGrArGrCrUrGrUrUrGrGr CrGrU-rArGrGrCrArArGrArGrUrGrCrCrUrUrG rArCrG rArUrArC
60 nt- G12V KRAS (5'Alexa Fluor 750)	/5Alex750N/rCrUrGrArArUrArUrArArArCrUrUr GrUrGrGrUrArGrUrUrGrGrArGrCrUrGrUrUrG rGrCrGrUrArGrGrCrArArGrArGrUrGrCrCrUrU rGrArCr-GrArUrArC
60 nt –WT KRAS (NCBI: NM_ 004985, human GTPase KRAS mRNA variant b, (positions 195-254)	/5Cy5/rCrUrGrArArUrArUrArArArCrUrUrGrU rGrGrU-rArGrUrUrGrGrArGrCrUrGrGrUrGrGr CrGrU-rArGrGrCrArArGrArGrUrGrCrCrUrUrG rArCrG rArUrArC

Oligonucleotides were ordered from IDT.

Supplementary Table 8. Primer oligos used in RT-PCR.

Oligo #	Sequence (5' → 3')	Amplicon (size)
KN469F	GGCCTGCTGAAAATGACTGAATATAAAC	KRAS (134 nt)
KN470R	ACAAGATTTACCTCTATTGTTGGATCATATTCG	KRAS
KN60F	ACCATCTTCCAGGAGCGAGATCCCTC	GAPDH (235 nt)
KN61R	TGCAGGAGGCATTGCTGATGATCTTGA	GAPDH
KN601F	TTTCACCATTCAAACAGGTCGAGCTG	PCSK9 (185 nt)
KN602R	TCCCTGCAGCCCCTACC	PCSK9
KN603F	GTTGTAGGCGAATCATTTGTTCAAAGCTG	GATA3 (159 nt)
KN604R	CAAACAACAATTACAGGGACTTGTTCACAAAG	GATA3

Oligonucleotides were ordered from IDT.

Supplementary Table 9. Primer oligos used in PCR-RFPLA.

Oligo #	Sequence (5' → 3')	Amplicon (size)
KN484F	TTATTATAAATAATGACTGAATATAAACTTGTGGTAGTTGGA**c**CT	KRAS (200 nt)
KN483R	TCCTCTTGACCTGCTGTGTCG	KRAS

Lower case "c" in KN484F denotes a mutation introduced in the primer to create *BstN*I recognition sequence. Oligonucleotides were ordered from IDT.

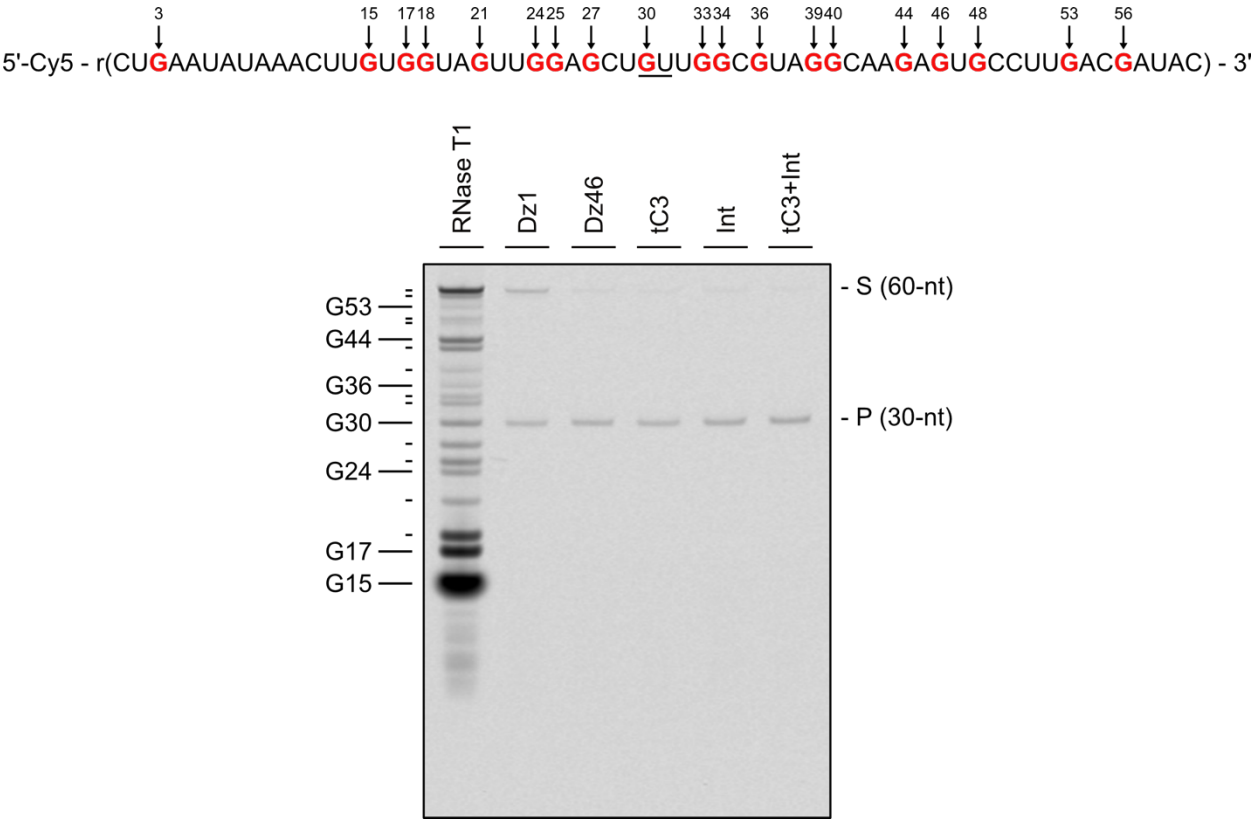

Supplementary Figure 1. Product Validation by Dz cleavage. *Depiction of full 60-nt G12V RNA substrate showing the 19 RNase T1 cut sites after G residues (red) and desired G-U cleavage junction (underlined). Denaturing PAGE gel showing product bands produced by Dz1 (unmodified 10-23), Dz46, tC3, Int, and tC3+Int alongside an RNA ladder produced by RNase T1. DNAzyme-catalyzed reactions were performed as 1:1 (S:E) single turnover in 1 mM $MgCl_2$, 50 mM Tris (pH 7.5), 10 mM NaCl, and 140 mM KCl at 37°C with 30-min incubation. The RNase T1 digestion was performed using 1 unit of RNase T1 in 50 mM Tris (pH 7.5), 10 mM NaCl, and 140 mM KCl at 24°C following a 1-min incubation. S: 5′-Cy5-labeled full-length substrate, P: 5′-Cy5-labeled cleavage product.*

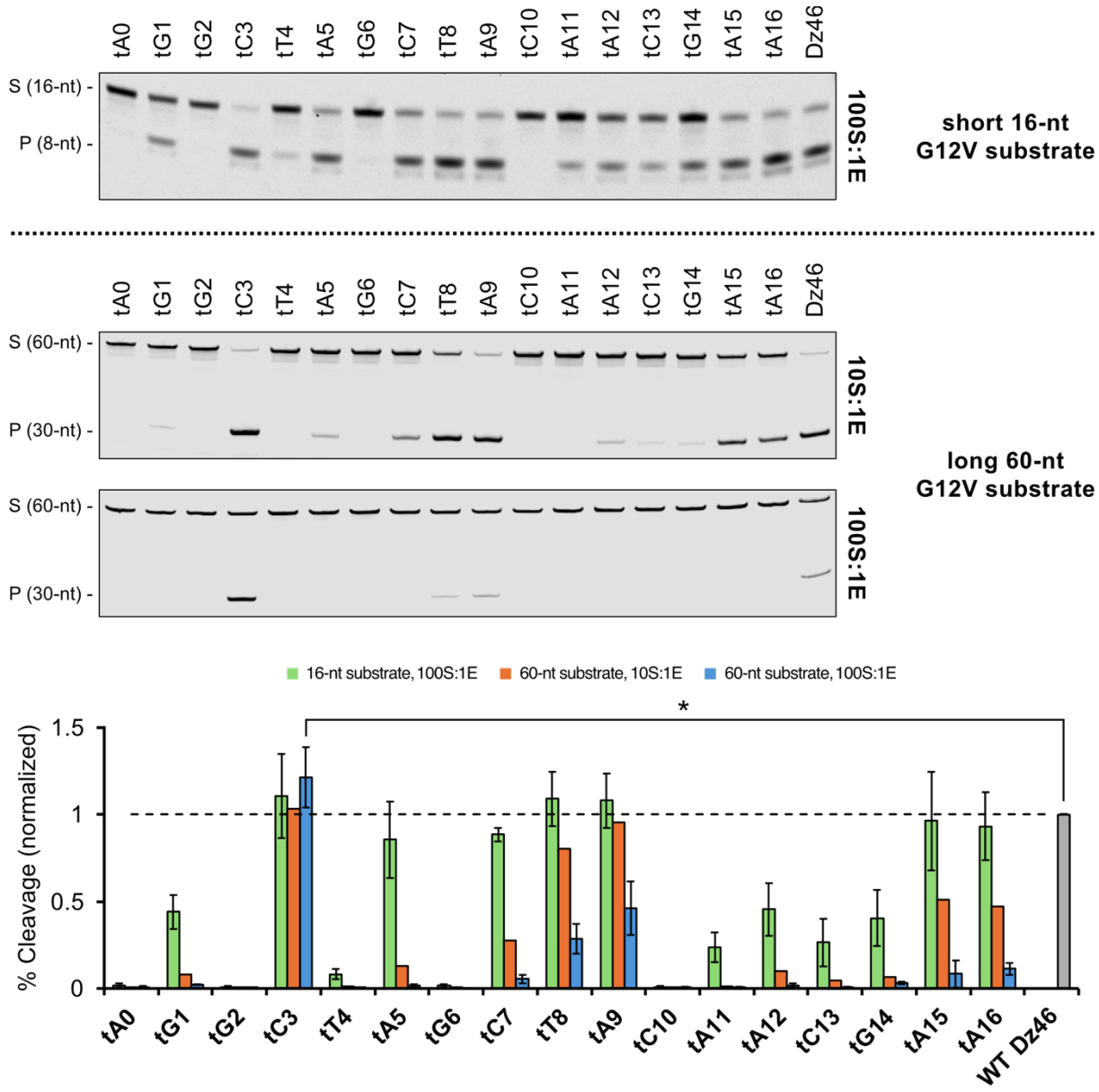

Supplementary Figure 2. TNA walk of the catalytic loop region. *Representative denaturing PAGE gel and corresponding bar graph showing RNA cleavage activity of a G12V RNA substrate after 30 min under different multiple turnover conditions on the short 16-nt substrate, 100S:1E (n=3), and long 60-nt substrate at both 10S:1E (n=1) and 100S:1E (n=3 for all constructs except for tC3 and Dz46 which have n=6). RNA cleavage activity (% cleavage) was normalized to Dz46. Data presented as the mean ± standard deviation. Two-tailed p-value determined by Welch's t-test (*, p<0.05). All reactions were performed under simulated physiological conditions in buffer containing 1 mM $MgCl_2$, 50 mM Tris (pH 7.5), 10 mM NaCl, and 140 mM KCl at 37°C. S: 5′-Cy5-labeled full-length substrate, P: 5′-Cy5-labeled cleavage product.*

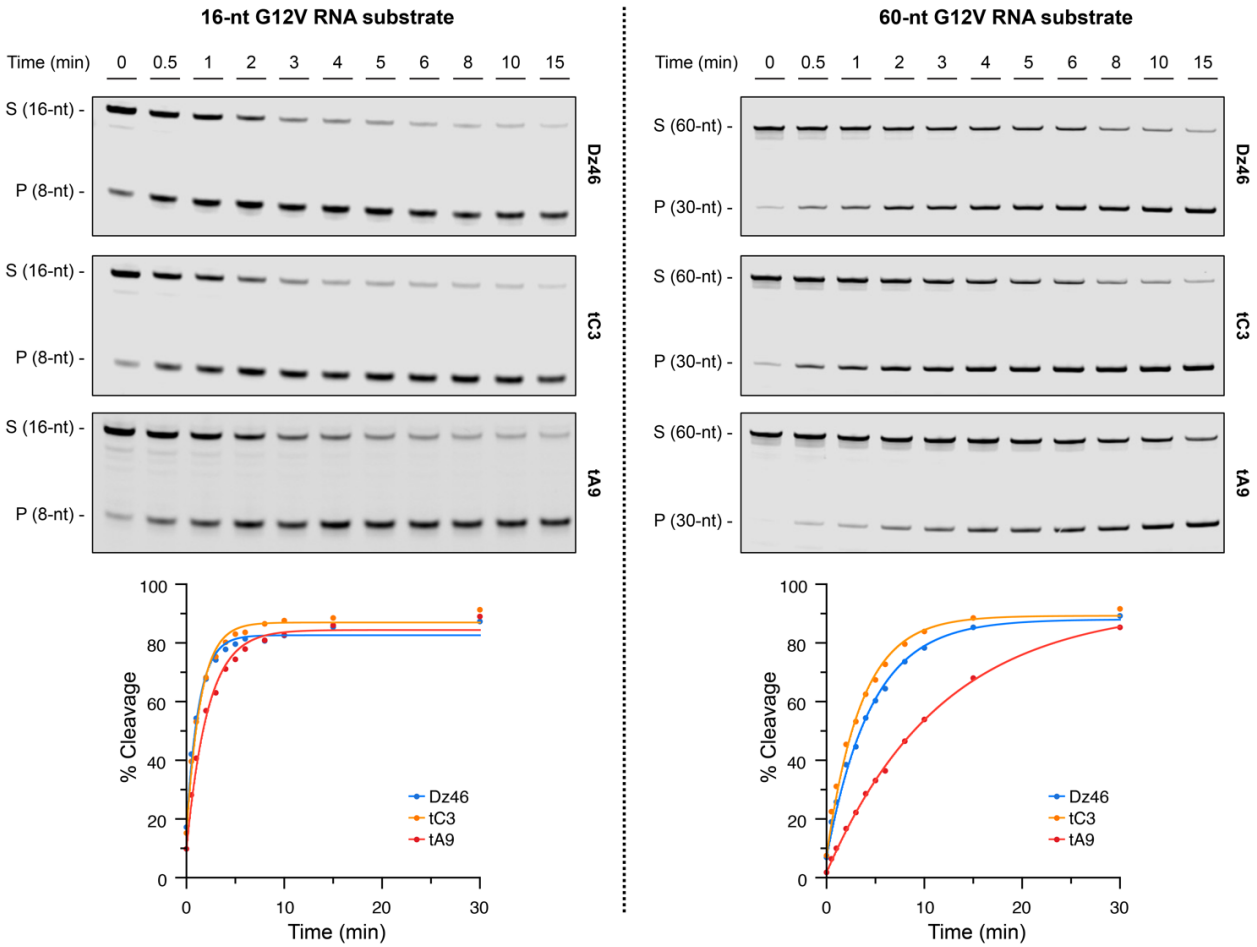

Supplementary Figure 3. RNA cleavage activity of Dz46, tC3, and tA9 on different length substrates. *Representative denaturing PAGE gel and corresponding kinetic curves showing 10:1 (S:E) multiple turnover RNA cleavage activity of a short 16-nt RNA substrate versus long 60-nt RNA substrate over the course of 15 min (n=1). All reactions were performed under simulated physiological conditions in buffer containing 1 mM $MgCl_2$, 50 mM Tris (pH 7.5), 10 mM NaCl, and 140 mM KCl at 37°C.*

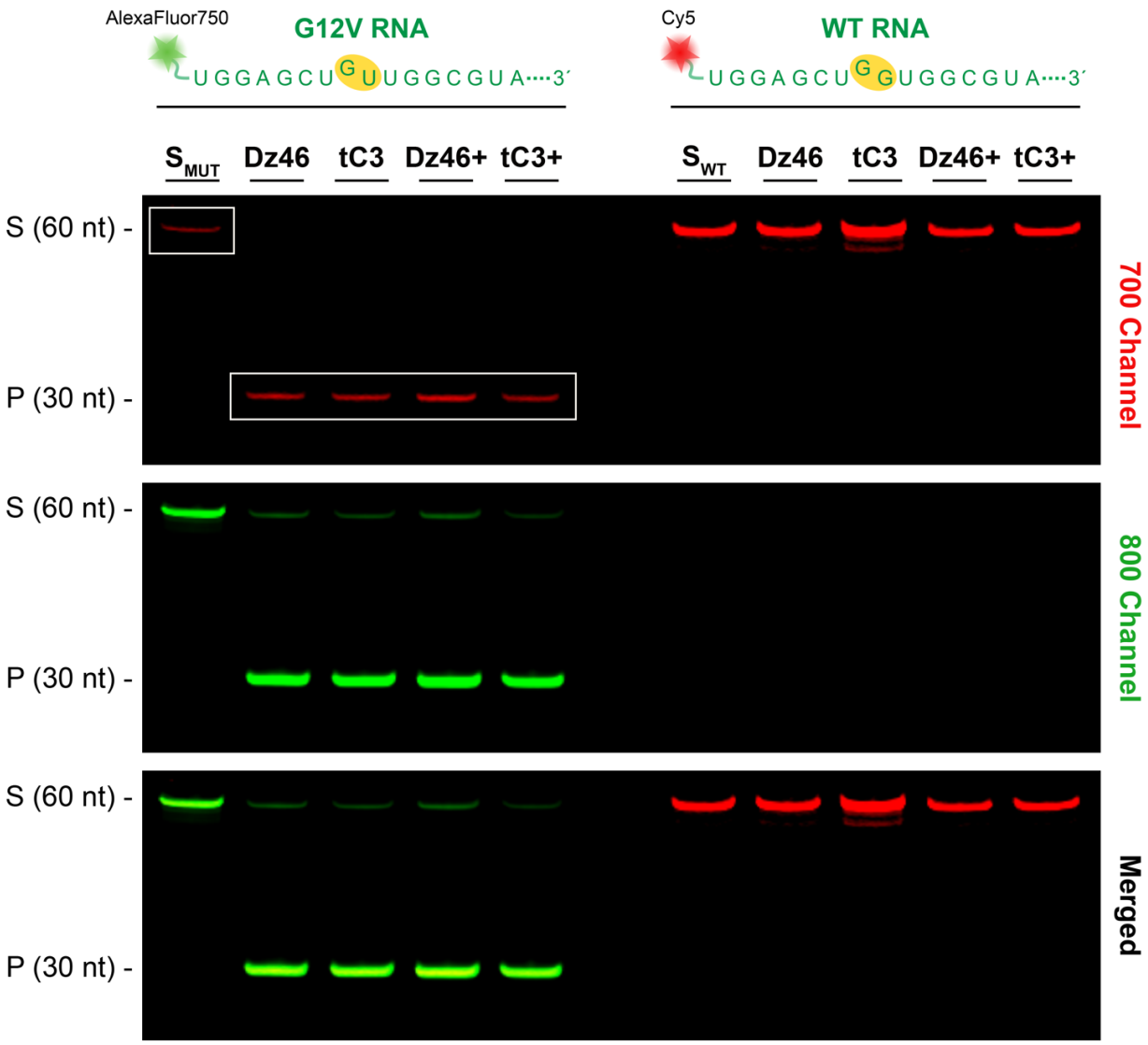

Supplementary Figure 4. Signal bleed through of AlexaFluor750 from the 800 to the 700 channel on the Odyssey CLx Imaging System (LI-COR). *Denaturing PAGE gel showing RNA cleavage profiles in 1:2 (S:E) single turnover reactions containing either the 60-nt G12V (green) or wild-type (red) substrates after a 30 min incubation. Individual 700 (red) and 800 (green) channels, as well as the merged image, are shown. Bleed through is observed in the P30 and P60 bands for AlexaFluor750 (green) (white box). Reactions performed under simulated physiological conditions in buffer containing 1 mM $MgCl_2$, 50 mM Tris (pH 7.5), 10 mM NaCl, and 140 mM KCl at 37°C. S: 5'-labeled full-length substrate, P: 5'-labeled cleavage product.*

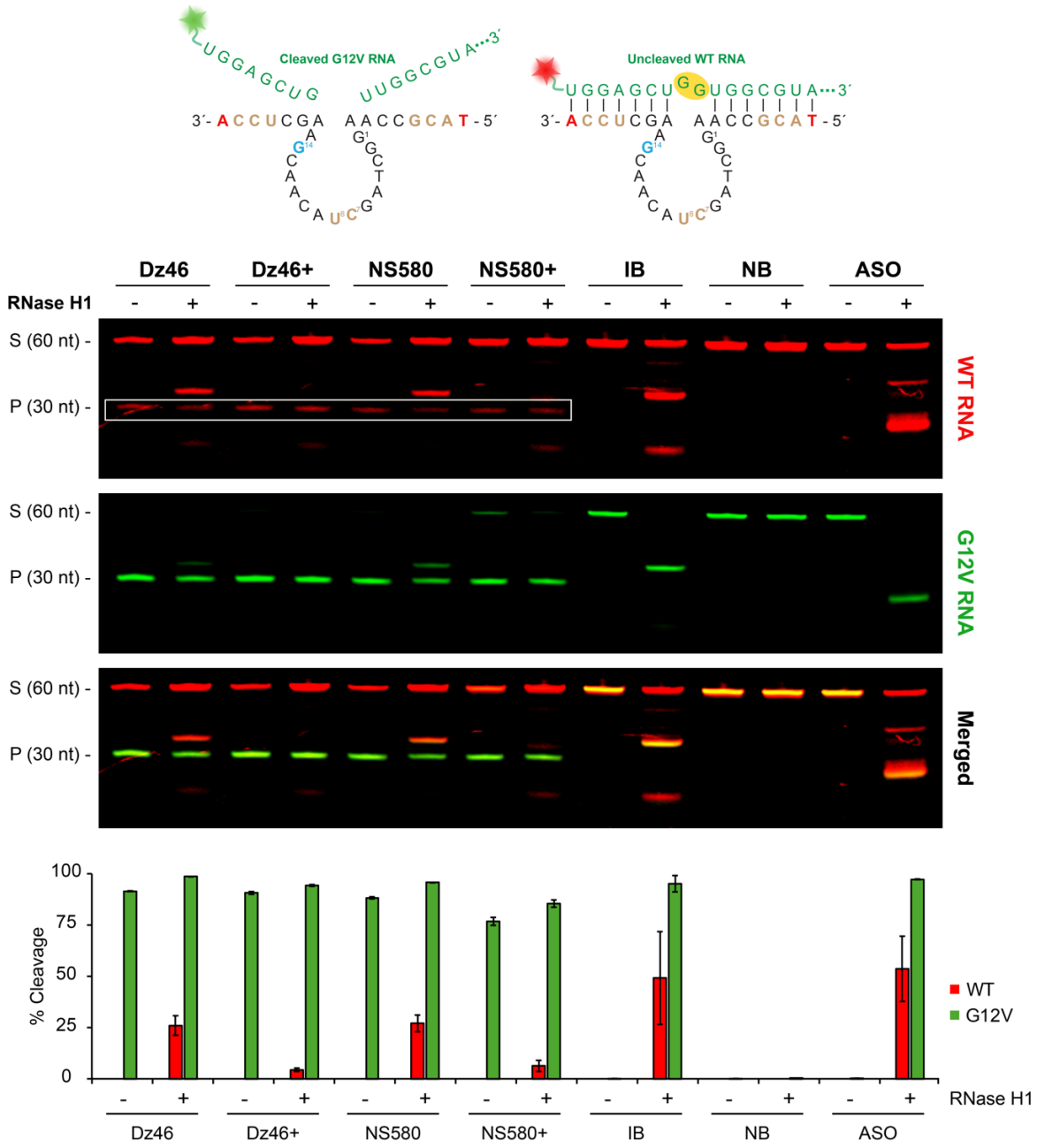

Supplementary Figure 5. Modulating RNase H activity using TNA modifications in the binding arms. *Cartoon representation of allele-specific G12V RNA cleavage and representative denaturing PAGE gel showing RNA cleavage profiles in reactions containing both the wild-type (red) and G12V (green) substrates (1:1) in the absence (-) or presence (+) of 5 ng/µL human RNase H1 after a 30 min incubation (n=2). Individual Cy5 (red) and AlexaFluor750 (green) channels, as well as the merged image, are shown. The corresponding bar graph shows the percent cleavage of WT (red) and G12V (green) substrate. The band at P30 was excluded from the analysis due to signal bleed through in the 700 nm channel (white box). Reactions performed under simulated physiological conditions in buffer containing 1 mM $MgCl_2$, 50 mM Tris (pH 7.5), 10 mM NaCl, and 140 mM KCl at 37°C. S: 5'-labeled full-length substrate, P: 5'-labeled cleavage product.*

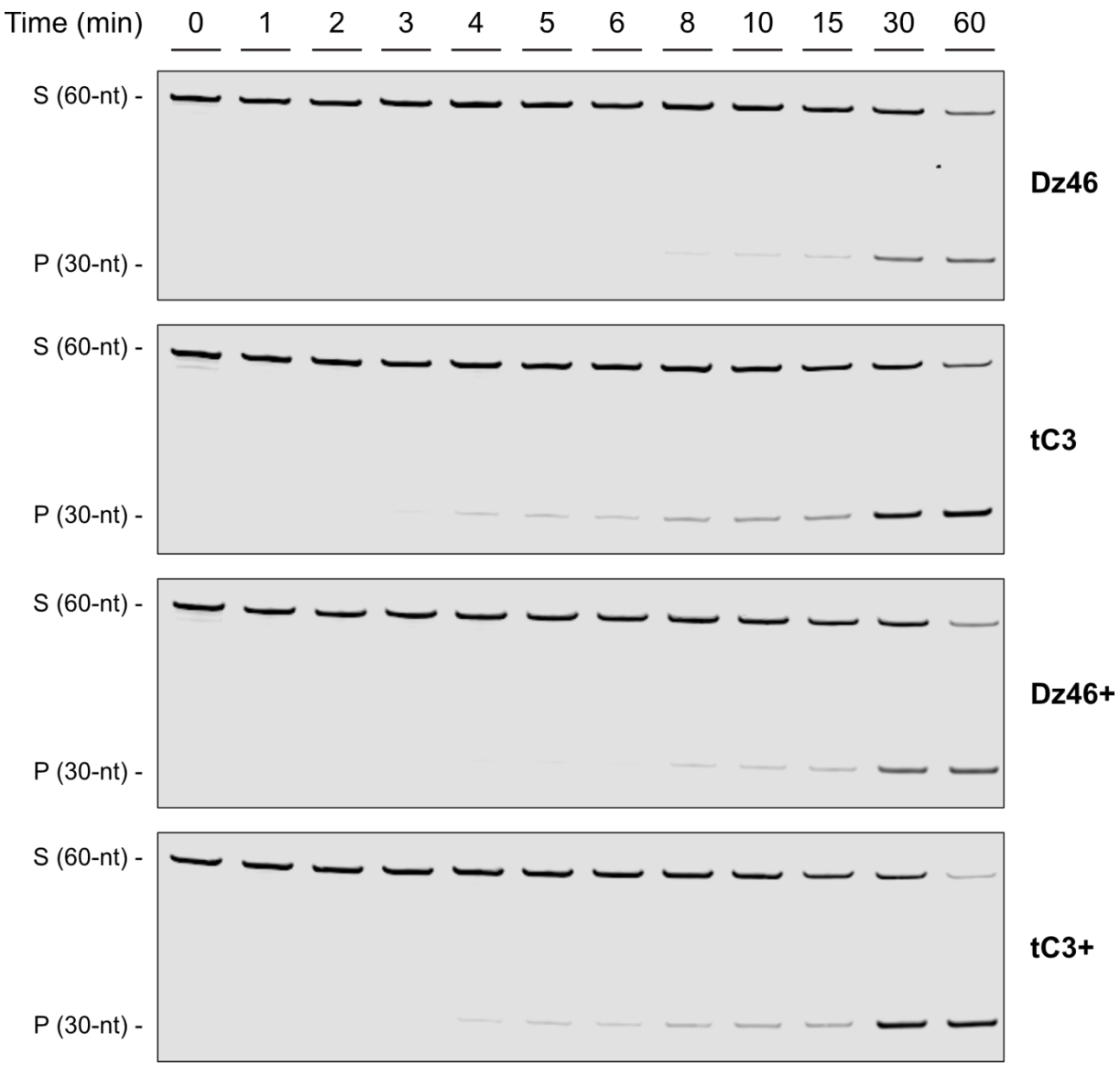

Supplementary Figure 6. Representative gels showing RNA cleavage activity of Dz46 and its variants carrying TNA modifications. *Representative denaturing PAGE gel showing 100:1 (S:E) multiple turnover RNA cleavage activity of a long 60-nt RNA substrate over the course of 60 min (n=2). Corresponding kinetic curves and initial velocity bar graphs shown in Figure 3b. All reactions were performed under simulated physiological conditions in buffer containing 1 mM $MgCl_2$, 50 mM Tris (pH 7.5), 10 mM NaCl, and 140 mM KCl at 37°C. S: 5'-labeled full-length substrate, P: 5'-labeled cleavage product.*

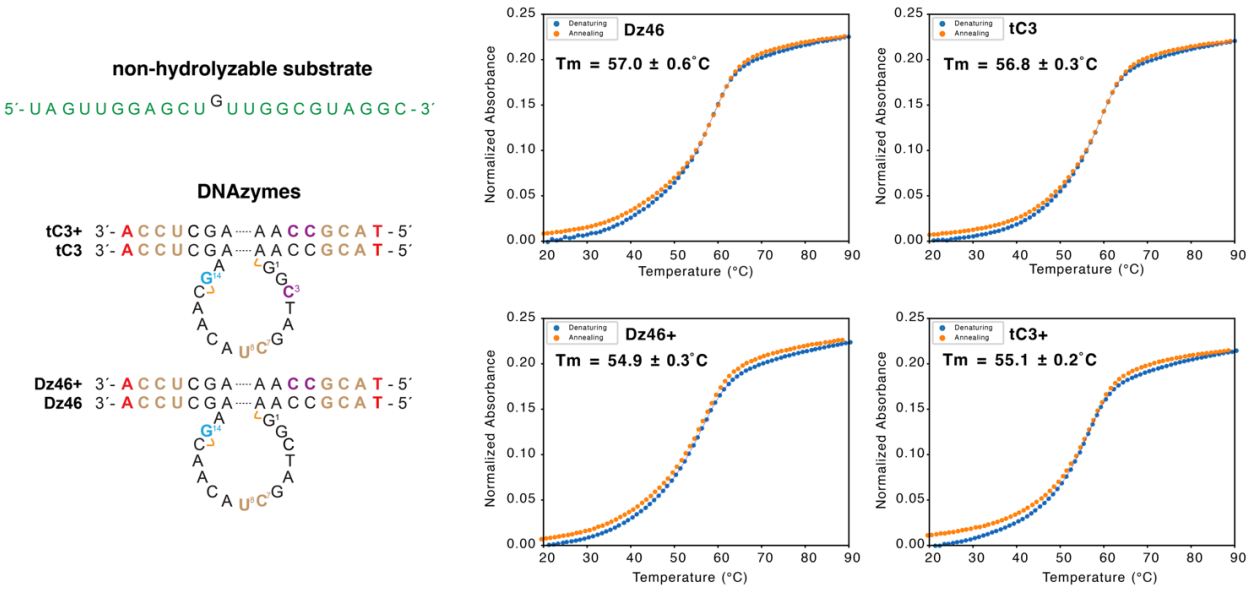

Supplementary Figure 7. Melting temperatures of Dz46 and its variants with TNA incorporations. *An uncleavable 21-nt RNA substrate with a 2′-deoxyribose G replacement at the G-U dinucleotide cleavage junction was used for melt measurements. All melts were performed with 1:1 oligonucleotide stoichiometry (1 µM enzyme + 1 µM RNA substrate) in 1 M NaCl, 50 mM Tris-HCl, 1 mM $MgCl_2$ at pH 7.5. Melting curves were obtained in the reverse and forward melting directions in a quartz cuvette of 1-cm path length with a temperature gradient of 20º to 90ºC and a ramping rate of 1°C per min by monitoring the change in UV absorbance at 260 nm at each temperature (n=2).*

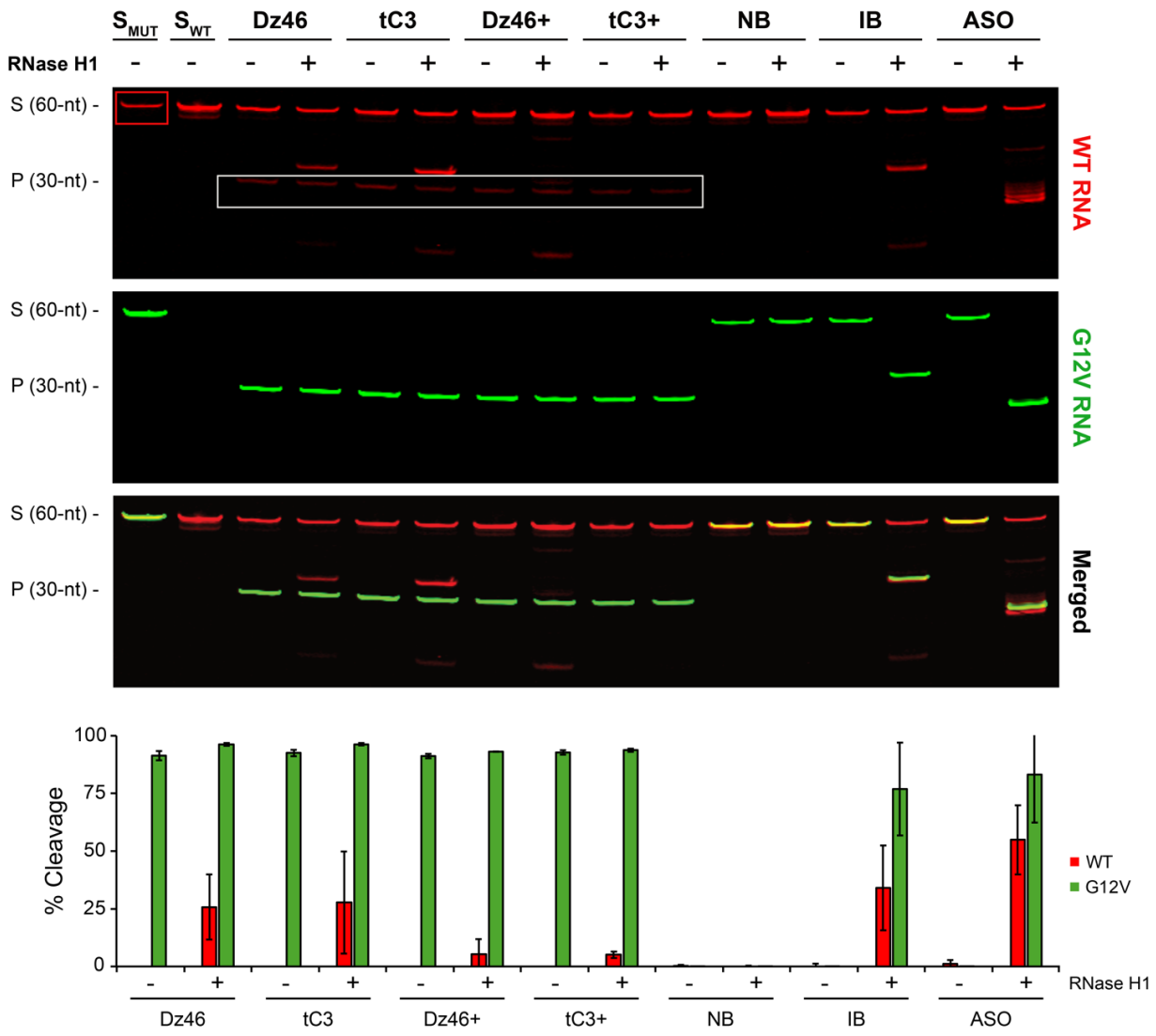

Supplementary Figure 8. RNase H activity of final chosen Dz46 variants carrying TNA modifications in the catalytic core and binding arms. *Representative denaturing PAGE gel showing RNA cleavage profiles in reactions containing both the wild-type (red) and G12V (green) substrates (1:1) in the absence (-) or presence (+) of 5 ng/µL human RNase H1 after a 30 min incubation (n=2). Individual Cy5 (red) and AlexaFluor750 (green) channels, as well as the merged image, are shown. The corresponding bar graph shows the percent cleavage of WT (red) and G12V (green) substrate. The red band at P30 was excluded from the analysis due to signal bleed through in the 700 nm channel (white box). Reactions performed under simulated physiological conditions in buffer containing 1 mM $MgCl_2$, 50 mM Tris (pH 7.5), 10 mM NaCl, and 140 mM KCl at 37°C. S: 5'-labeled full-length substrate, P: 5'-labeled cleavage product.*

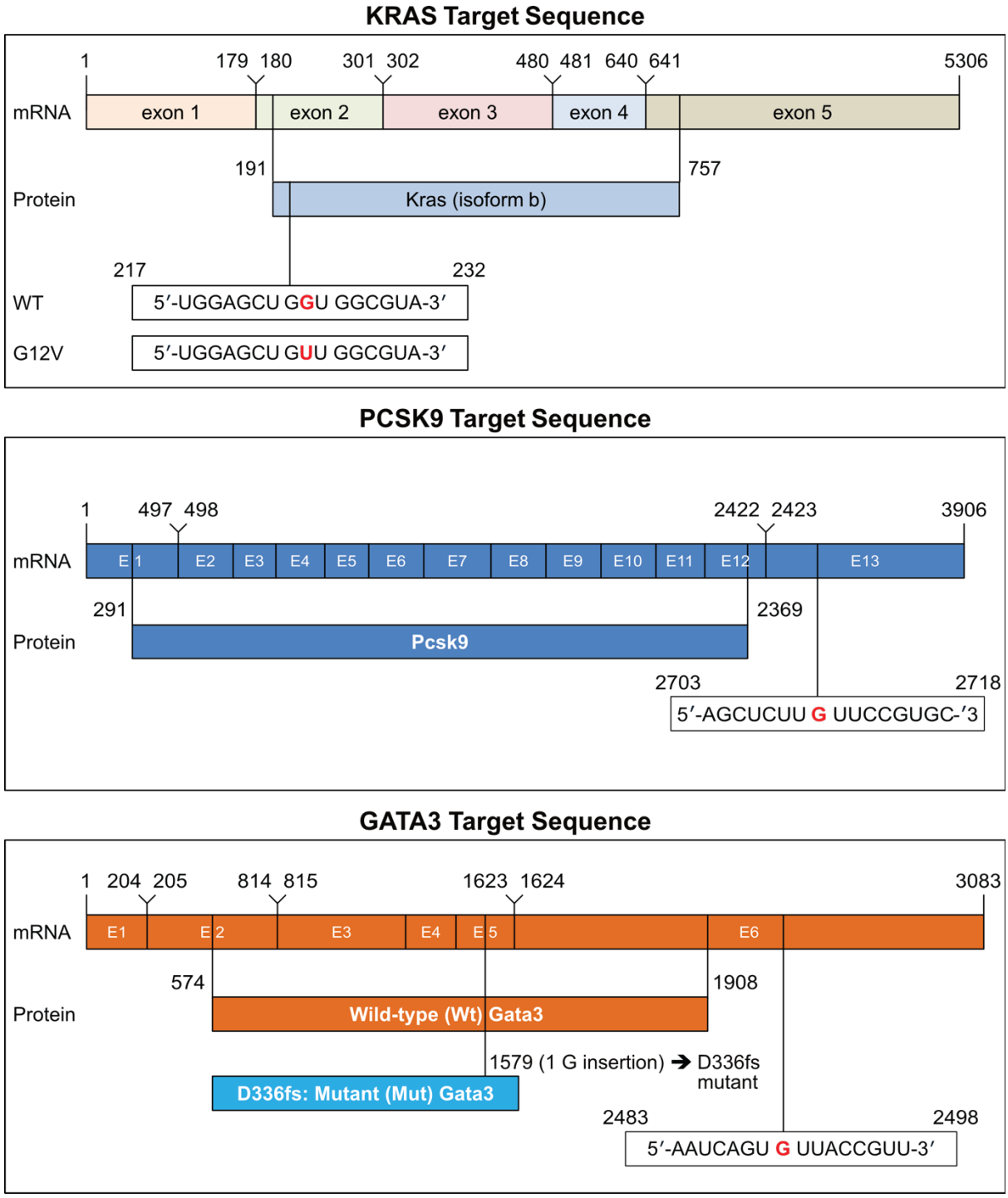

Supplementary Figure 9. Protein targets chosen for knockdown assays. *WT KRAS mRNA sequence was obtained from NCBI (Accession number: NM_004985). Target sequence of G12V mutant derived from a single point mutation (G→U) is shown along with the WT. Human PCSK9 mRNA sequence was obtained from NCBI (Accession number: NM_174936.4). Human GATA3 mRNA sequence was obtained from NCBI (Accession number: NM001002295.2). GATA3 targeting Dz does not discriminate WT and mutant.*

APPENDIX C: Supplementary Data for Chapter 3

Supplementary Table 1. Oligonucleotides used in the threozyme selection.

Name	Sequence (5' → 3')
KRAS G12V N15 DNA Library	CTCTGCTGAAGCCAGTTACC AGTTGGAGCT(N15)TTGGCGTAGG GGTGG-TATCCCCAAGGGGAC
KRAS G12V N20 DNA Library	CTCTGCTGAAGCCAGTTACC AGTTGGAGCT(N20)TTGGCGTAGG GGTGG-TATCCCCAAGGGGAC
Hairpin Primer	pACTACGTACCCACAACCTCGGCCGTACCACGGTACGTAGT GTCCCCTTGGG-GATACCACC
Strand Displacement Primer w/KRAS G12V RNA Substrate	Biotin-r(GUGGUAGUUGGAGCUGUUGGCGUAGG)GGTGGTATCC CCAAGGG-GACACTACGTACCGTGGTACGGCCGAGGTTGTG
Reverse Primer PBS8	GTCCCCTTGGGGATACCACC
Forward Primer PBS23	CTCTGCTGAAGCCAGTTACC
PEGylated Forward Primer PBS23	AACAAACAAACAAACAAACA-iSp9-CTCTGCTGAAGCCAGTTACC

RNA (r); triethylene glycol spacer (iSp9).

Supplementary Table 2. Chemically synthesized threozymes used in the study.

Name	Sequence (3' → 2')	Calc. Mass (Da)	Obs. Mass (Da)	Δ Mass (Da)
N15-1	ACGCCAAACAACGGTAGTTGGAAGCTCCA	8498.2	8501.8	3.6
N15-2	ACGCCAAAATCGACCGAGCTTTAGCTCCA	8409.1	8412.2	3.1
N15-3	ACGCCAAACAATAGAAGCTGTTAGCTCCA	8457.2	8461.0	3.8
N15-4	ACGCCAATTAAAAACACTACAAAGCTCCA	8394.2	8398.0	3.8
N15-5	ACGCCAATTTACACGATACAAAAGCTCCA	8401.1	8404.4	3.3
N15-6	ACGCCAATTCACCGCTAGCTTGAGCTCCA	8376.1	8379.8	3.7
N20-1	ACGCCAAGAAAAGCCACAGAACTAAGTAGCTCCA	9939.1	9943.5	4.4
N20-2	ACGCCAAAATGGCCCTGTTAAGCGTTTAGCTCCA	9910.0	9914.7	4.7
N20-3	ACGCCAAGTATCGCTACTTACAAAACCAGCTCCA	9832.0	9836.7	4.7
N20-4	ACGCCAATGATAGAAGTTTCCTGGTCGAGCTCCA	9950.0	9954.1	4.1
N20-5	ACGCCAATGGAGTGCAACTAAGGTCAAAGCTCCA	9977.1	9980.8	3.7
N20-6	ACGCCAAATCGACTAGTATACACGAACAGCTCCA	9881.0	9884.7	3.7
6-29	TCGAGCTCTCAATAAGGGGATGAGTT	7685.7	7689.0	3.3
13-38	GTAGAGAAGTCTTATTGGTGGTTGAAGGGATGAGTT	10800.6	10808.1	7.5

Supplementary Table 3. RNA substrates used in the study.

Name	Sequence (5' → 3')
KRAS G12V RNA	IR680-AGUUGGAGCUGUUGGCGUAGG
EGFR T790M RNA	Cy5-AACUCAUCAUGCAGCUCGA

Supplementary Table 4. Rate constants (k_{obs}) and activation energies (E_a).

Enzyme	Temp (˚C)	k_{obs} (h^{-1})	± SE	E_a (kJ/mol)	± SE
Tz N15-1	37	0.02	0.002	77.5	7.2
	50	0.06	0.0008		
Tz N20-1	37	0.02	0.0008	79.4	2.7
	50	0.07	0.001		
Tz 6-29	37	0.07	0.004	9.1	5.3
	50	0.08	0.005		
Tz 13-38	37	0.27	0.02	-47.0	5.7
	50	0.13	0.008		
Dz 10-23	37	21.7	1.1	-158.2	14.4
	50	1.8	0.4		

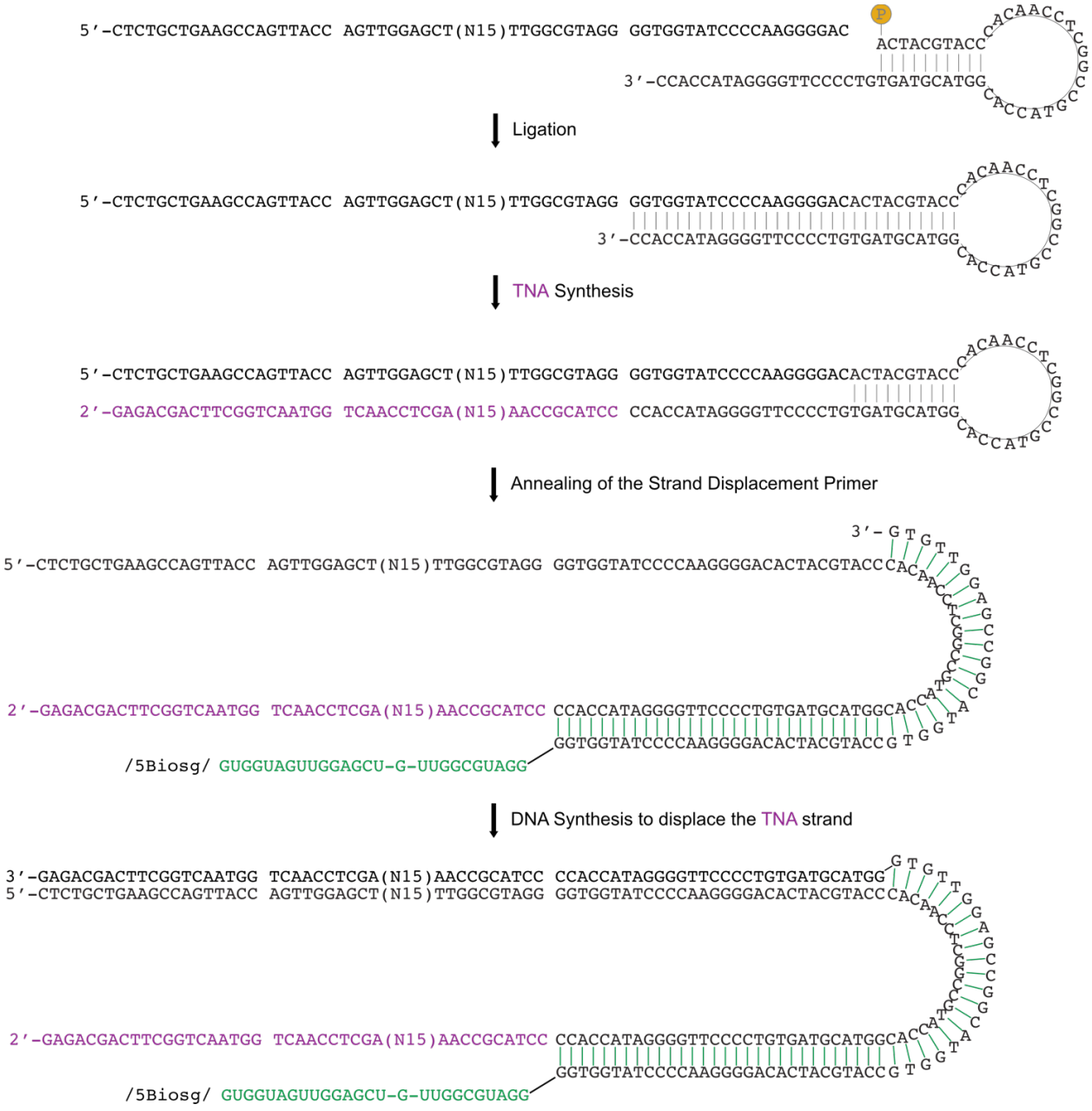

Supplementary Figure 1. Schematic of DNA display. *A DNA stem-loop structure is ligated to a DNA library, extended with TNA, and the resulting hairpin undergoes a strand displacement reaction by extending a DNA substrate annealed to the loop region with DNA. Colors: DNA (black), TNA (purple), and RNA (green).*

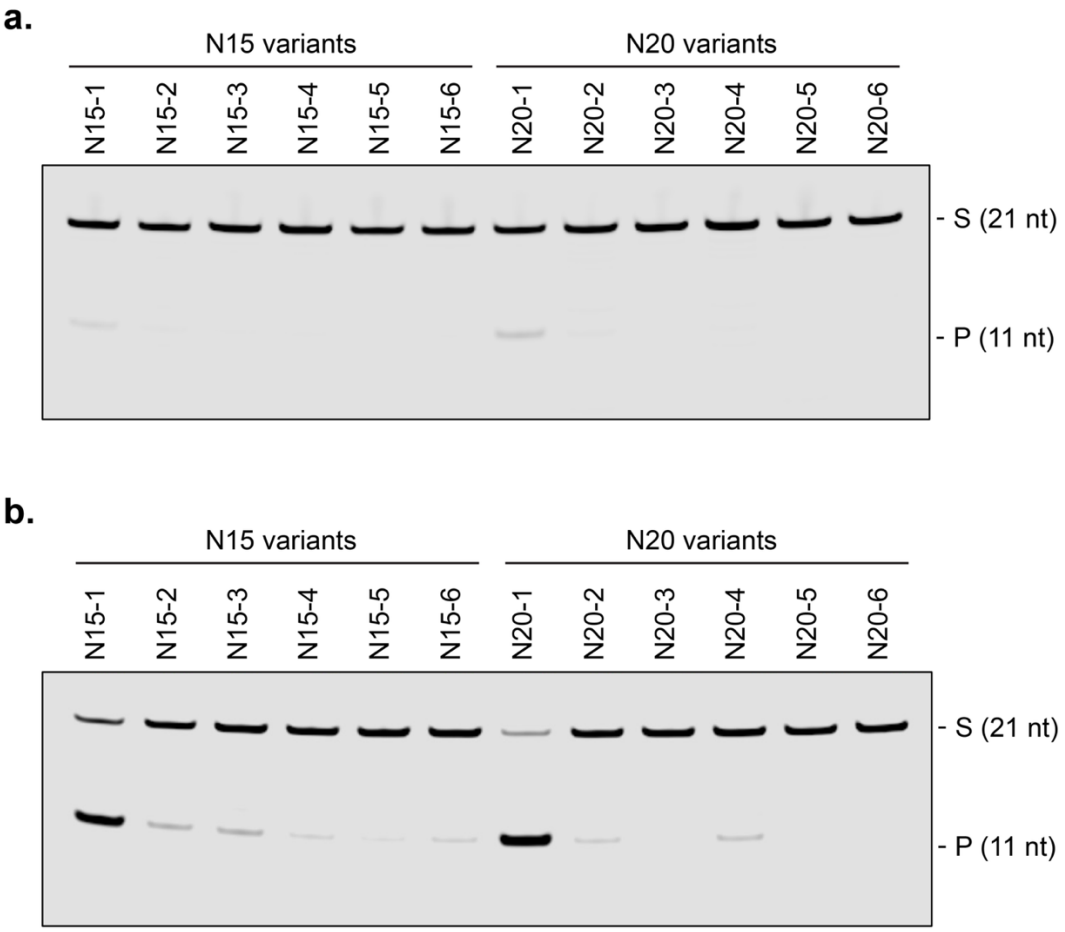

Supplementary Figure 2. Threozyme screen for RNA-cleavage activity. a-b. *Representative denaturing PAGE gels of the six most enriched sequences from the N15 and N20 libraries screened for activity at 37°C (panel a) and 50°C (panel b), respectively. All reactions (n=3 independent experiments) were performed in 50 mM Tris (pH 7.5), 10 mM NaCl, 140 mM KCl, and 20 mM $MgCl_2$ at either 37°C or 50°C for 24 hours with 250 nM substrate and 500 nM enzyme (1:2, S:E). S: 5'-IR680 labeled full-length substrate, P: 5'-IR680 labeled cleavage product. Molecular weight markers indicated to the right of the gel.*

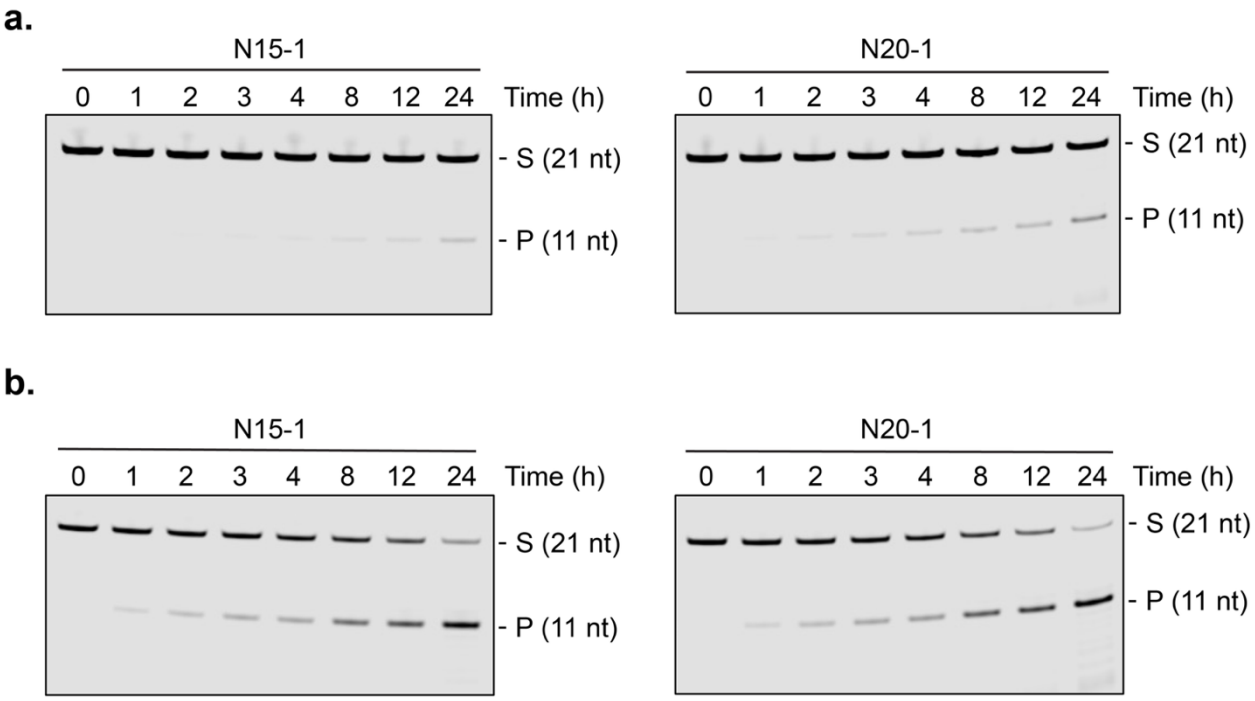

Supplementary Figure 3. Temperature-dependent RNA cleavage activity of top performing threozymes isolated by in vitro evolution. *a-b. Representative denaturing PAGE gels of the most active threozymes from the N15 and N20 libraries assessed in time course reactions performed at 37°C (panel a) and 50°C (panel b), respectively. All reactions (n=3 independent experiments) were performed in 50 mM Tris (pH 7.5), 10 mM NaCl, 140 mM KCl, and 20 mM $MgCl_2$ at either 37°C or 50°C with 250 nM substrate and 500 nM enzyme (1:2, S:E). S: 5'-IR680 labeled full-length substrate, P: 5'-IR680 labeled cleavage product. Molecular weight markers indicated to the right of the gel.*

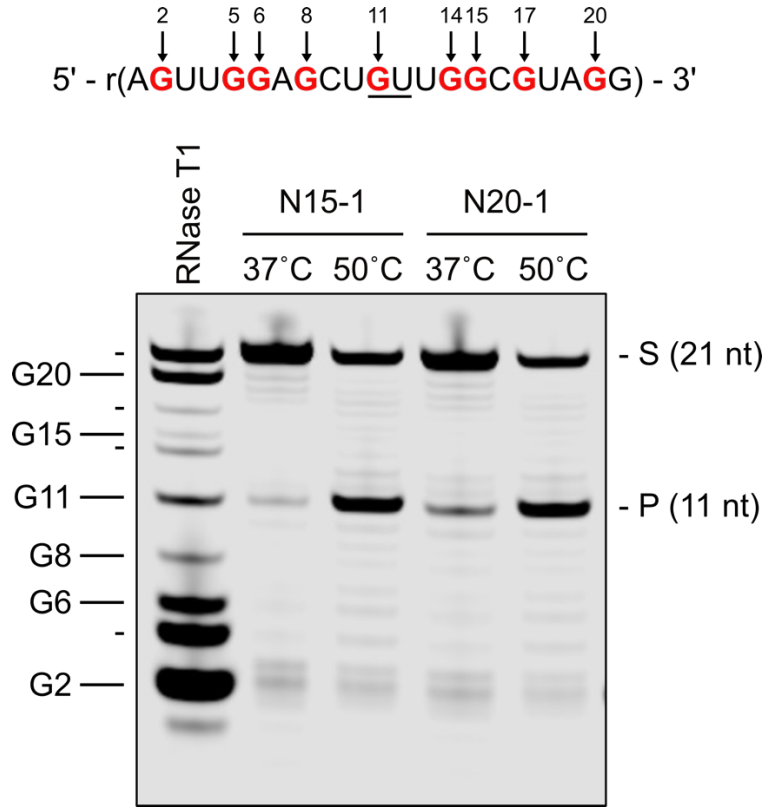

Supplementary Figure 4. Cleavage site validation by Tz N15-1 and N20-1. *Schematic depiction of the 21-nt RNA substrate showing the RNase T1 cut sites after G residues (red) and desired G-U cleavage junction (underlined). A denaturing PAGE gel showing the full-length substrate and upstream product of threozyme-mediated cleavage reactions alongside an RNA ladder produced by RNase T1 digestion. Threozyme reactions were performed in 50 mM Tris (pH 7.5), 10 mM NaCl, 140 mM KCl, and 20 mM $MgCl_2$ at either 37˚C or 50°C with 250 nM substrate and 500 nM enzyme (1:2, S:E). S: 5'-IR680 labeled full-length substrate, P: 5'-IR680 labeled cleavage product. Molecular weight markers indicated to the right of the gel.*

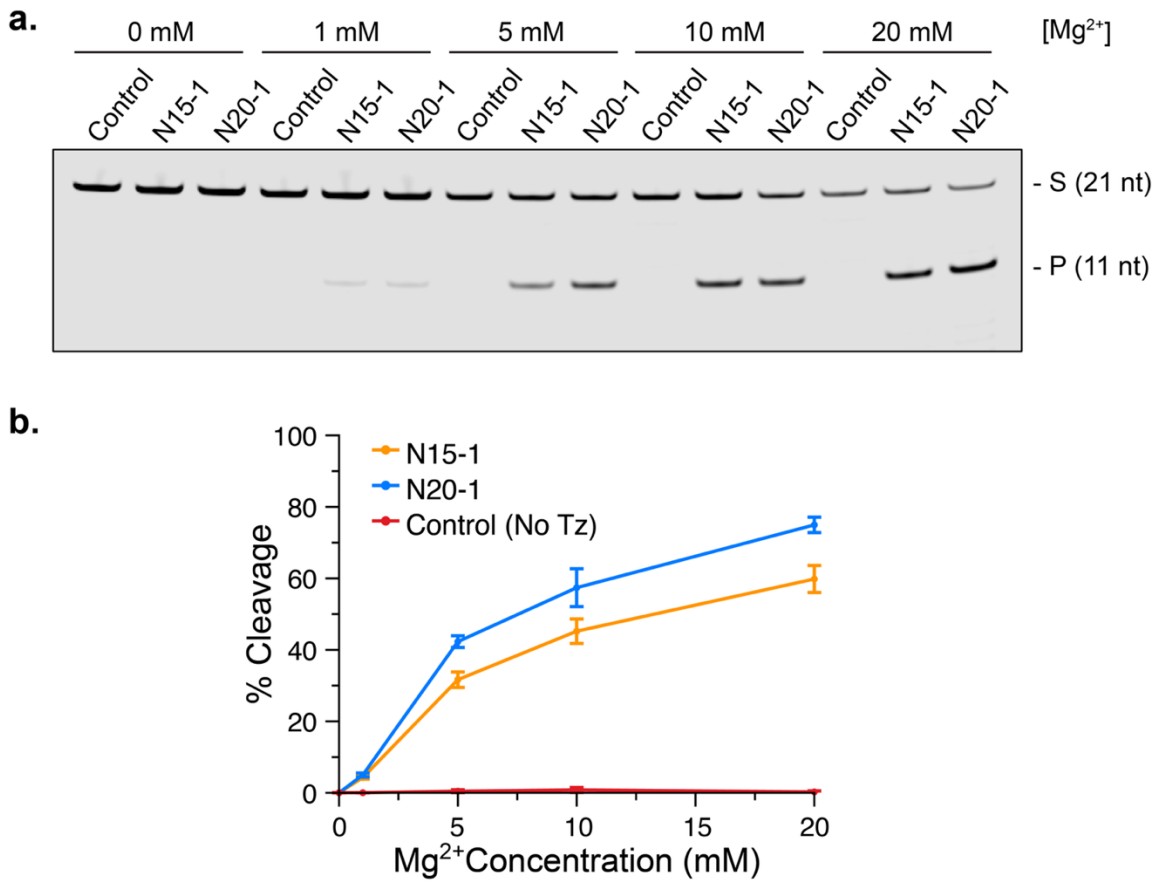

Supplementary Figure 5. Magnesium requirement for threozyme activity. a. *Representative denaturing PAGE gel of Tz N15-1 and N20-1 assessed in the presence of increasing concentration of Mg^{2+} (0 – 20 mM) after 18 hours of incubation at 50°C.* ***b.*** *Plot of catalytic activity as a function of magnesium concentration. Data presented as the mean ± standard deviation (n=3 independent experiments). All reactions were performed in 50 mM Tris (pH 7.5), 10 mM NaCl, and 140 mM KCl with 250 nM substrate and 500 nM enzyme (1:2, S:E). S: 5'-IR680 labeled full-length substrate, P: 5'-IR680 labeled cleavage product.*

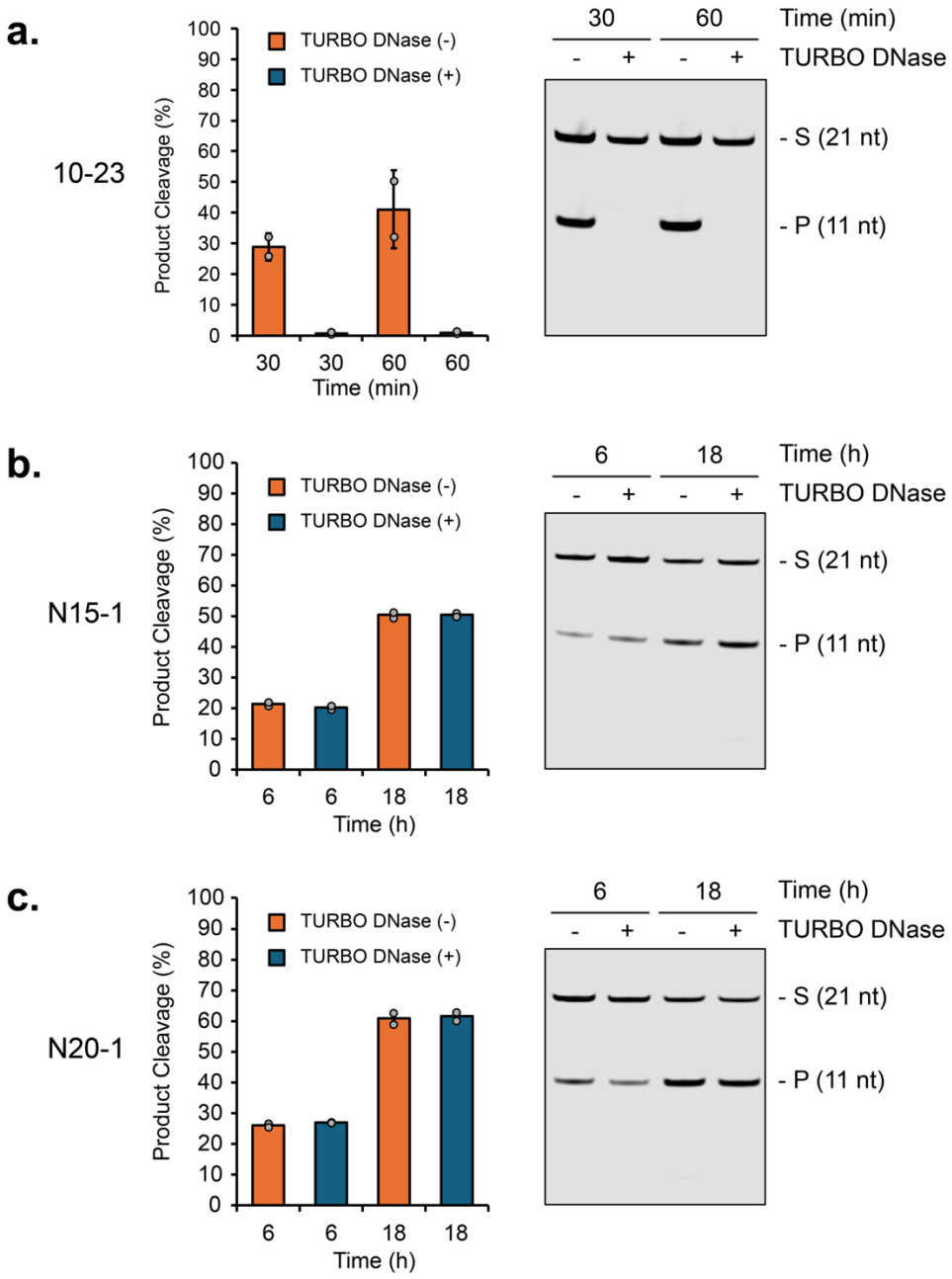

Supplementary Figure 6. Nucleic acid catalysis following preincubation with Turbo DNase. a. *Representative denaturing PAGE gel of Dz 10-23 mediated RNA cleavage in the absence and presence of Turbo DNase.* ***b-c.*** *Representative denaturing PAGE gels of Tz N15-1 and N20-1 mediated RNA cleavage in the absence and presence of Turbo DNase. Data presented as the mean ± standard deviation (n=2 independent experiments). All reactions were performed by pretreating the catalysts with Turbo DNase in 50 mM Tris (pH 7.5), 10 mM NaCl, and 140 mM KCl at 37°C before addition of the RNA substrate to the reaction. Dz catalyzed reactions contained 2 mM $MgCl_2$, while Tz reactions contained 20 mM $MgCl_2$. For the Tz reactions, the temperature was increased to 50°C after the initial preincubation period and RNA substrate addition. S: 5'-IR680 labeled full-length substrate, P: 5'-IR680 labeled cleavage product.*

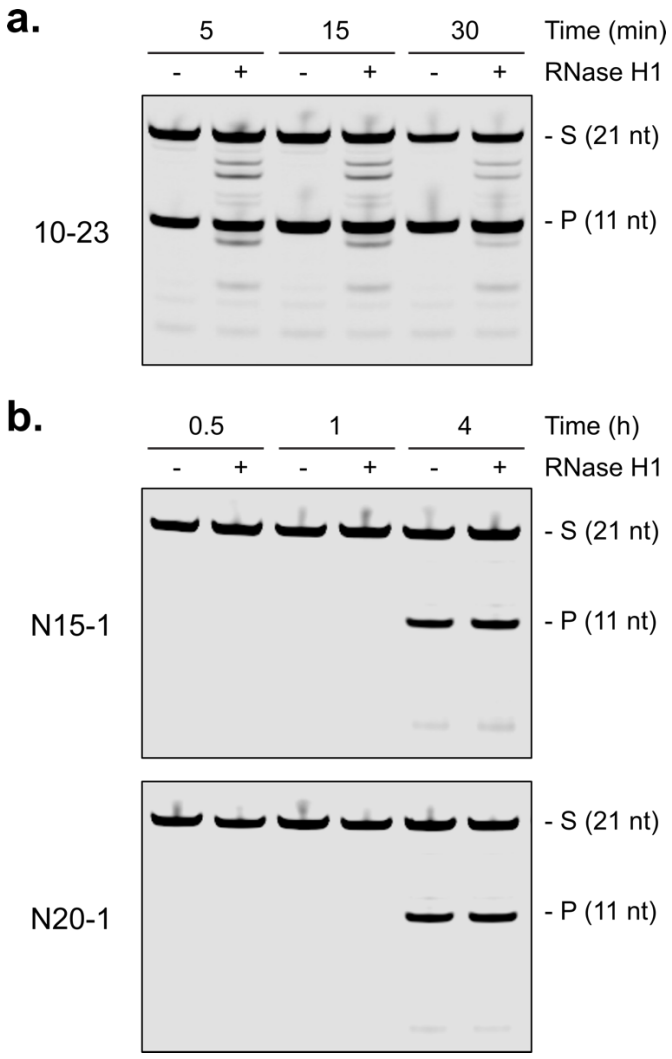

Supplementary Figure 7. Nucleic acid catalysis in the absence and presence of RNase H1. a. *Representative denaturing PAGE gel of Dz 10-23 mediated RNA cleavage in the absence and presence of human RNase H1.* ***b.*** *Representative denaturing PAGE gels of Tz N15-1 and N20-1 mediated RNA cleavage in the absence and presence of human RNase H1. All reactions (n=2 independent experiments) were performed in 50 mM Tris (pH 7.5), 10 mM NaCl, and 140 mM KCl with 250 nM substrate and 250 nM enzyme (1:1, S:E) at 37˚C. Dz catalyzed reactions contained 2 mM $MgCl_2$, while the Tz catalyzed reactions contained 20 mM $MgCl_2$. After 1 hour of incubation at 37˚C, the temperature of the Tz reaction was increased to 50°C for an additional 4 hours. S: 5'-IR680 labeled full-length substrate, P: 5'-IR680 labeled cleavage product.*

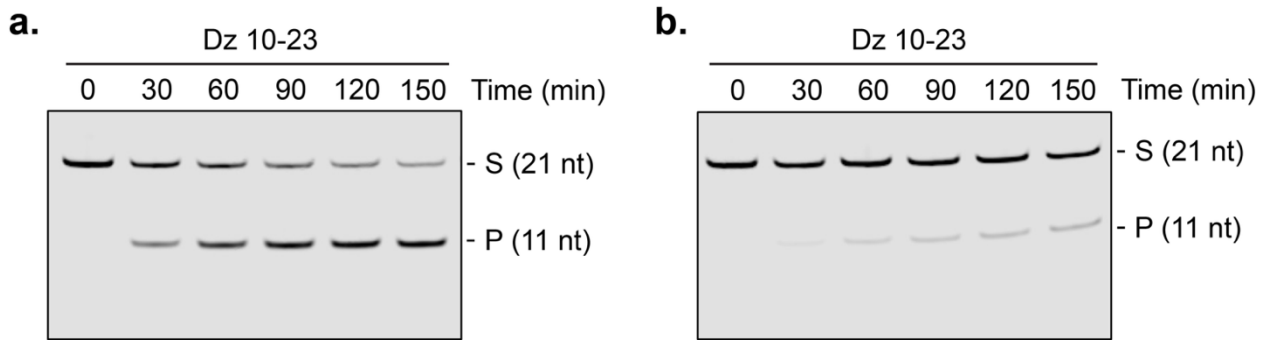

Supplementary Figure 8. Temperature-dependent RNA cleavage activity of Dz 10-23 under multiple turnover conditions. a-b. *Representative denaturing PAGE gels of 10-23 activity in time course reactions performed at 37°C (panel a) and 50°C (panel b), respectively. All reactions (n=3 independent experiments) were performed in 50 mM Tris (pH 7.5), 10 mM NaCl, 140 mM KCl, and 2 mM $MgCl_2$ at either 37°C or 50°C with 250 nM substrate and 25 nM enzyme (10:1, S:E). S: 5'-IR680 labeled full-length substrate, P: 5'-IR680 labeled cleavage product. Molecular weight markers indicated to the right of the gel.*

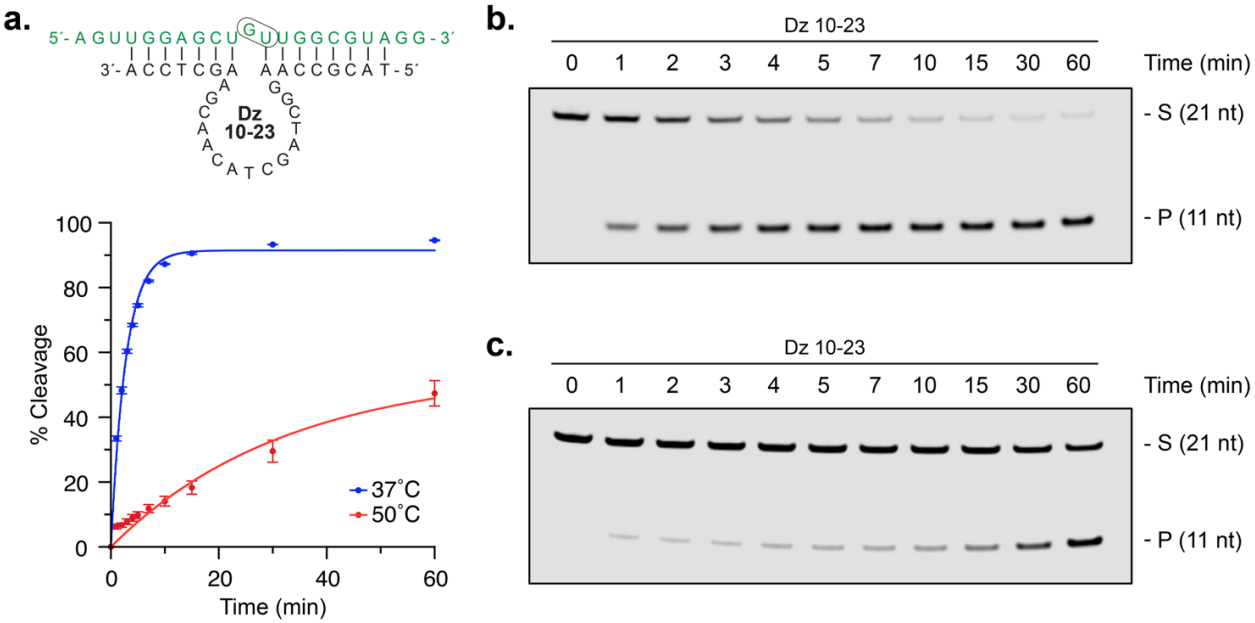

Supplementary Figure 9. Temperature-dependent RNA cleavage activity of Dz 10-23 under single turnover conditions. a. *Kinetic curves of Dz 10-23. Reaction profiles show RNA cleavage at 37°C (blue) and 50°C (red). Enzyme-substrate complex is provided above the plot. The cleavage site is denoted with a circle.* ***b-c.*** *Representative denaturing PAGE gels of 10-23 activity in time course reactions performed at 37°C (panel b) and 50°C (panel c), respectively. Data presented as the mean ± standard deviation (n=3 independent experiments). All reactions were performed in 50 mM Tris (pH 7.5), 10 mM NaCl, 140 mM KCl, and 2 mM $MgCl_2$ at either 37°C or 50°C with 0.5 µM substrate and 2.5 µM enzyme (1:5, S:E). S: 5'-IR680 labeled full-length substrate, P: 5'-IR680 labeled cleavage product. Molecular weight markers indicated to the right of the gel.*

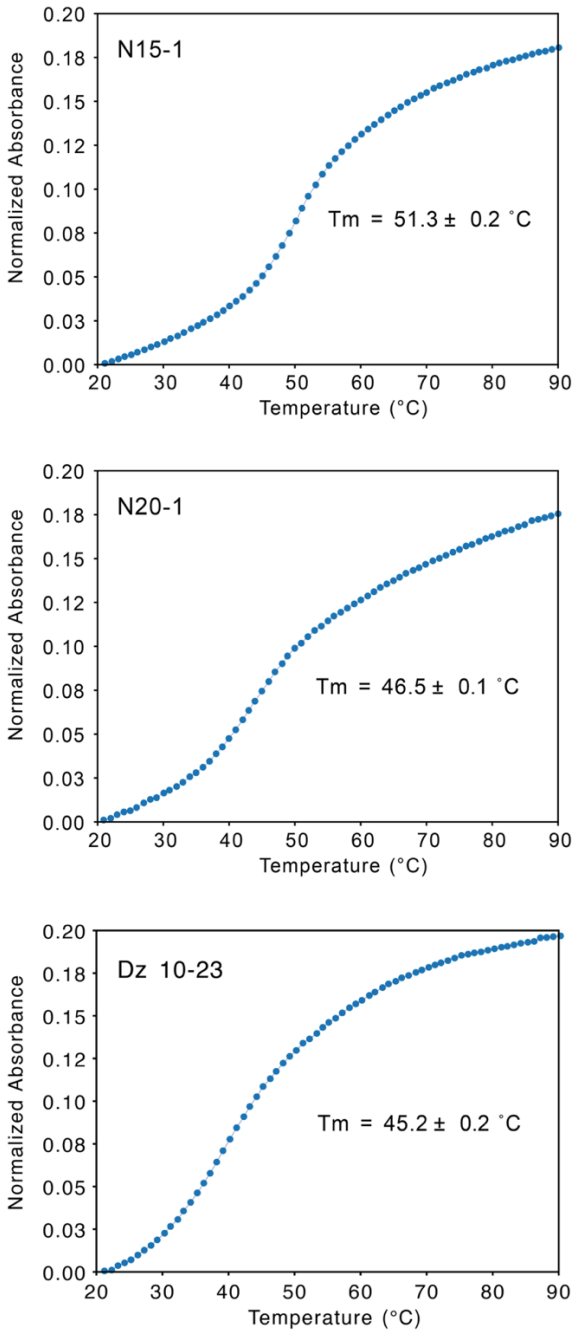

Supplementary Figure 10. Melting temperature of enzyme-substrate complexes. *An uncleavable 21-nt RNA substrate with a 2′-deoxyribose G substitution at the G-U dinucleotide cleavage junction was used for melt measurements. All melts were performed with 1:1 oligonucleotide stoichiometry (1 μM enzyme + 1 μM RNA substrate) in the Tz and Dz reaction buffers. Melting curves were obtained (n=2 independent experiments) in the forward direction in a quartz cuvette with a 1-cm path length and a temperature range of 20º to 90ºC. Thermal denaturation was performed with a ramping rate of 1°C per min by monitoring changes in UV absorbance (260 nm).*

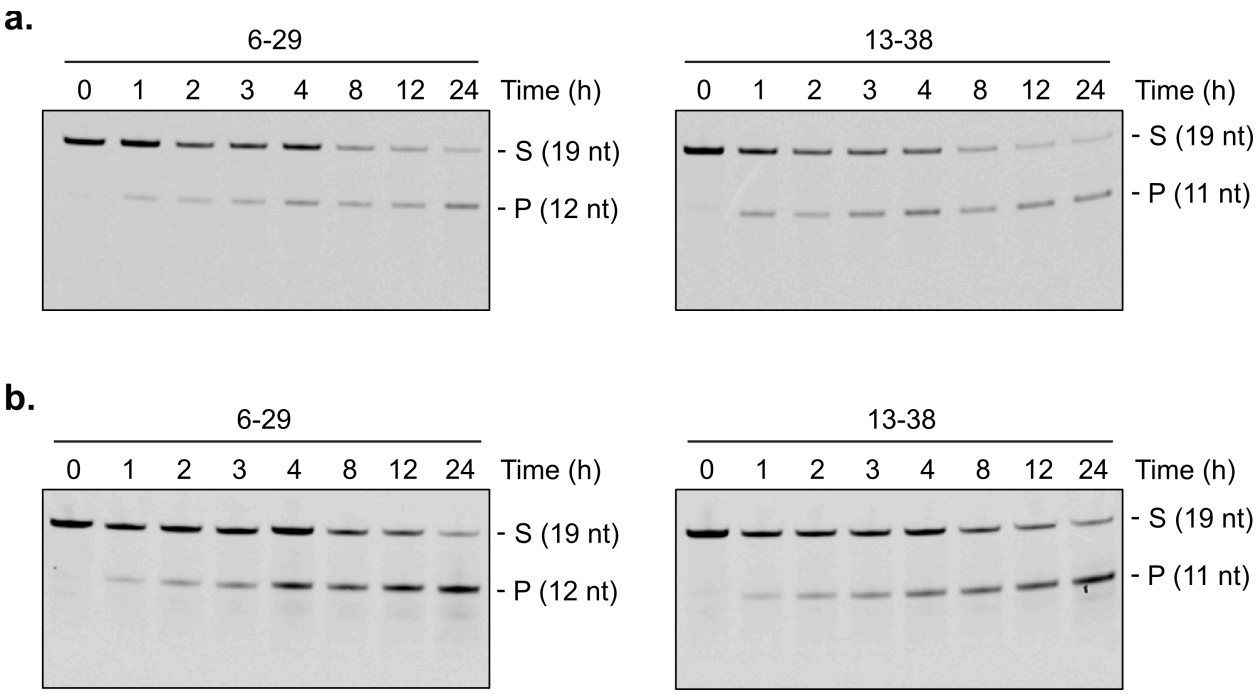

Supplementary Figure 11. Temperature-dependent RNA cleavage activity of known threozymes that function with more flexible active sites. a-b. *Representative denaturing PAGE gels of threozyme activity in time course reactions performed at 37°C (panel a) and 50°C (panel b), respectively. All reactions (n=3 independent experiments) were performed in 50 mM Tris (pH 7.5), 10 mM NaCl, 140 mM KCl, and 20 mM $MgCl_2$ at either 37°C or 50°C with 250 nM substrate and 500 nM enzyme (1:2, S:E). S: 5'-Cy5 labeled full-length substrate, P: 5'-Cy5 labeled cleavage product. Molecular weight markers indicated to the right of the gel.*

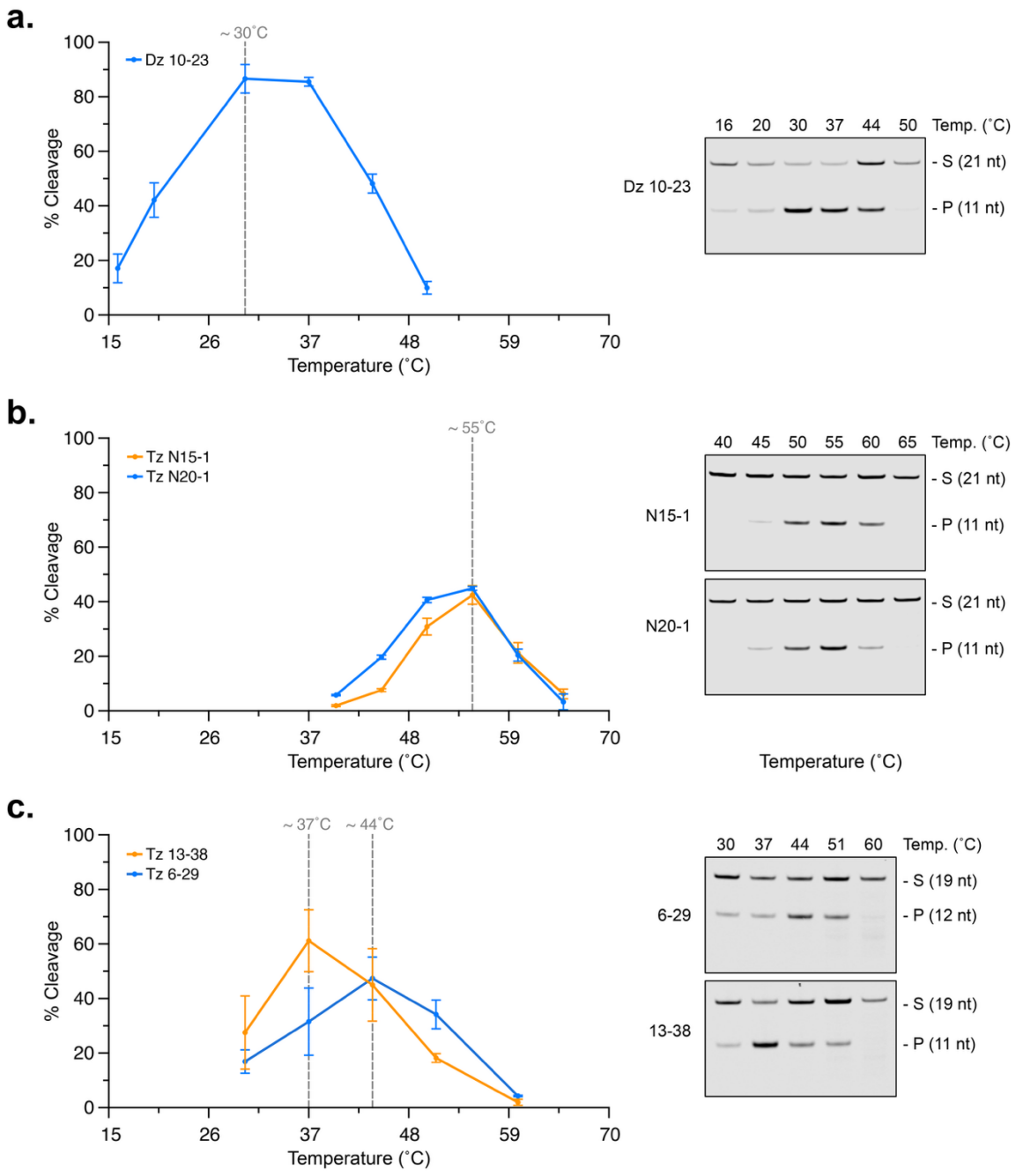

Supplementary Figure 12. Comparison of temperature optimum for RNA cleavage. a-c. *Plots and representative denaturing PAGE gel of RNA cleavage activity at increasing temperatures for Dz 10-23 (panel a), Tz N15-1 and N20-1 with constrained active sites (panel b), and Tz 6-29 and 13-38 with flexible active sites (panel c). Data presented as the mean ± standard deviation (n=3 independent experiments). All reactions were performed in 50 mM Tris (pH 7.5), 10 mM NaCl, and 140 mM KCl with 8 hours of incubation. Dz catalyzed reactions contained 2 mM $MgCl_2$ with 250 nM substrate and 25 nM enzyme, while the Tz catalyzed reactions contained 20 mM $MgCl_2$ with 250 nM substrate and 500 nM enzyme.*

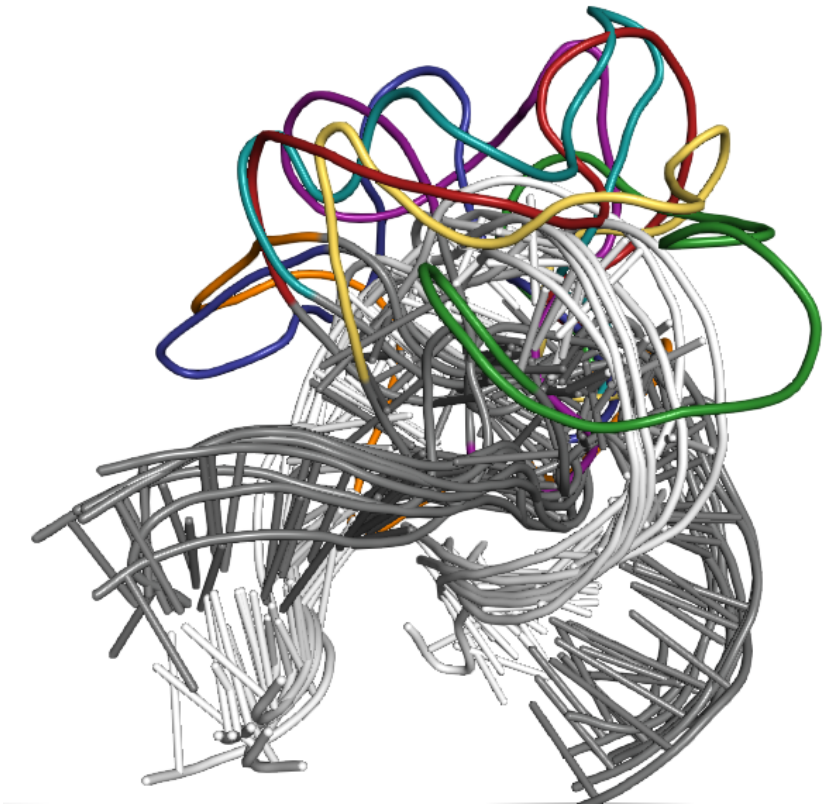

Supplementary Figure 13. NMR-derived structural ensemble of Dz 10-23. *NMR analysis of Dz 10-23 (PDB: 7PDU) showing a highly dynamic catalytic loop (colored loops) displayed on more rigid substrate binding arms (grey).*